EXPERIMENTAL AND PHENOMENOLOGICAL INVESTIGATIONS OF FEMTOSCOPIC CORRELATION FUNCTIONS IN HEAVY-ION COLLISIONS

DÁNIEL KINCSES

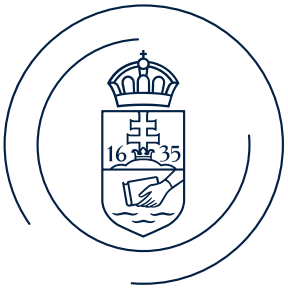

EÖTVÖS LORÁND
UNIVERSITY

A dissertation submitted for the degree of Doctor of Philosophy

under the supervision of Dr. Máté Csanád
D.Sc., associate professor, Department of Atomic Physics

Doctoral School of Physics – head: Prof. Jenő Gubicza
Particle and Nuclear Physics Program – head: Prof. Zoltán Trócsányi

Eötvös Loránd University
Faculty of Natural Sciences

DOI: 10.15476/ELTE.2022.164

2022

Dániel Kincses: *Experimental and phenomenological investigations of femtoscopic correlation functions in heavy-ion collisions,* A dissertation submitted for the degree of Doctor of Philosophy, © 2022

PUBLICATIONS

The present dissertation is based on the following publications:

[1] Dániel Kincses. "Lévy analysis of HBT correlation functions in $\sqrt{s_{NN}} = 62$ GeV and 39 GeV Au+Au collisions at PHENIX." In: *Universe* 4.1 (2018), p. 11. DOI: 10.3390/universe4010011. arXiv: 1711.06891 [nucl-ex].

[2] Dániel Kincses, Márton I. Nagy, and Máté Csanád. "Coulomb and strong interactions in the final state of Hanbury-Brown–Twiss correlations for Lévy-type source functions." In: *Phys. Rev. C* 102.6 (2020), p. 064912. DOI: 10.1103/PhysRevC.102.064912. arXiv: 1912.01381 [hep-ph].

[3] Dániel Kincses, Maria Stefaniak, and Máté Csanád. "Event-by-event investigation of the two-particle source function in heavy-ion collisions with EPOS." In: *Entropy* 24 (2022), p. 308. DOI: 10.3390/e24030308. arXiv: 2201.07962 [hep-ph].

[4] Maria Stefaniak and Dániel Kincses. "Investigating the pion source function in heavy-ion collisions with the EPOS model." In: *Proc. SPIE Int. Soc. Opt. Eng.* 11581 (2020), p. 1158112. DOI: 10.1117/12.2580570. arXiv: 2008.03139 [hep-ph].

[5] Dániel Kincses. "Shape Analysis of HBT Correlations at STAR." In: *Phys. Part. Nucl.* 51.3 (2020), pp. 267–269. DOI: 10.1134/S106377962003017X. arXiv: 1911.05352 [nucl-ex].

[6] Dániel Kincses. "PHENIX results on collision energy dependent Levy HBT correlations from $\sqrt{s_{NN}}$ = 15 to 200 GeV." In: *Acta Phys. Polon. Supp.* 12 (2019), p. 445. DOI: 10.5506/APhysPolBSupp.12.445. arXiv: 1811.08311 [nucl-ex].

[7] Dániel Kincses. "PHENIX results on Lévy analysis of Bose-Einstein correlation functions." In: *Acta Phys. Polon. Supp.* 10 (2017), pp. 627–631. DOI: 10.5506/APhysPolBSupp.10.627. arXiv: 1610.05025 [nucl-ex].

[8] Dániel Kincses. "PHENIX results on Bose-Einstein correlation functions." In: *Acta Phys. Polon. Supp.* 9 (2016), p. 243. DOI: 10.5506/APhysPolBSupp.9.243. arXiv: 1602.04578 [nucl-ex].

[9] Andrew Adare et al., PHENIX Coll. "Lévy-stable two-pion Bose-Einstein correlations in $\sqrt{s_{NN}} = 200$ GeV Au+Au collisions." In: *Phys. Rev. C* 97.6 (2018), p. 064911. DOI: 10.1103/PhysRevC.97.064911. arXiv: 1709.05649 [nucl-ex].

Papers [1–3] are published in refereed journals, and are representing the main thesis points of this dissertation. Papers [4–8] are conference proceedings articles, which (although did not went through rigorous peer-review) are also an important part of the dissertation. Furthermore, I also played an important role in the work published in [9]. This paper is not part of the thesis points, but it provided the basis for all the other experimental works included in this list of publications hence it is detailed in the dissertation.

ACKNOWLEDGMENTS

I started my university studies with the intention of doing research in the field of experimental particle physics. I was lucky enough to find an excellent supervisor in Máté Csanád early on, who not only meticulously guided me through the maze of high-energy heavy-ion physics but, along the way, provided me with extraordinary opportunities, for which I am truly grateful. I also owe thanks to the wizard, Márton Nagy, whose brilliant ideas, tips and tricks in programming, and enthusiasm for science helped me tremendously during my research. Thanks for sharing your office with me!

I would like to thank Tamás Csörgő, my co-supervisor during my first data analysis projects, whose wisdom I could always count on, and also all of my colleagues from the PHENIX experiment, Tamás Novák, Wesley Metzger, Sándor Lökös, Gábor Dávid, and many others.

I also want to thank Ákos Horváth for supporting me since my early TDK days.

I am thankful to Hanna Zbroszczyk and the Warsaw STAR group for hosting me multiple times in Warsaw and helping me jump-start my STAR data analysis.

I am especially grateful to Roy Lacey for his hospitality during my Fulbright scholarship in Stony Brook. His wit and experience are unmatched, and it is always a pleasure discussing various topics with him during coffee breaks at conferences or at a bar afterward.

During my studies, I tried to seize all opportunities to travel the world, and along this journey, I made many new friends.

I barely knew Maria Stefaniak back when she drove from Long Island with her rental Mini Cooper to pick me up at JFK. Since then, not only have we become really good friends, but co-authors as well – our idea for a project connecting our separate research directions became an essential part of this dissertation. Thank you for your constant support; here is to many more scientific and non-scientific adventures together!

I want to thank my Stony Brook office mate, Ben Schweid, for inducting me to American culture, being hospitable, and always driving me to the jam sessions at the Stony Brook Jazz Loft.

I would like to thank my musician friends, whom I think of as a second family; Pali, Balázs, Lőrinc, and all other members of Kalász Jazz Band, furthermore Viki, Hajni, Balázs, and all other members of Kamp János Kapelle.

Many thanks to Imi, Anita, and Bori, especially to the latter two, for making me amazing flat whites and tolerating me while I spent countless hours working in Málna, writing my dissertation (or just procrastinating and complaining).

Plato supposedly said that the ideal citizen is the scholar-athlete, the man of thought, and the man of action. While trying to live by this quote, I also made many new friends in powerlifting, became a coach myself, and managed to keep my sanity during a global pandemic. I want to thank my coach Boti and all my training partners from the Óbuda gym; I am sure we will achieve many more pr-s together.

Finally, I want to thank Fruzsi, whose overwhelming support during the time of writing this dissertation gave me the strength to keep going. As a two times national champion powerlifter, she somehow manages to lift the weight off my shoulders as well.

Last but not least, I want to express my gratitude to my family, especially my parents and my brother for providing a stable and always encouraging background. I often set my ambitions very high, and they always believe in me.

My research was supported by the US-Hungarian Fulbright Commission, the ÚNKP-17-3 and ÚNKP-18-3 New National Excellence program of the Hungarian Ministry of Human Capacities, the ÚNKP-19-3 and ÚNKP-21-4 New National Excellence Program of the Hungarian Ministry for Innovation and Technology from the source of the National Research, Development and Innovation Fund, the NKFIH grants FK-123842, FK-123959, K-138136 and 2019-2.1.11-TÉT-2019-00080, and the COST Action CA15213 THOR.

CONTENTS

LIST OF FIGURES

LIST OF TABLES

ACRONYMS

QGP	Quark-Gluon-Plasma
QCD	Quantum Chromo Dynamics
LBL	Lawrence Berkeley National Laboratory
AGS	Alternating Gradient Synchrotron
RHIC	Relativistic Heavy Ion Collider
BNL	Brookhaven National Laboratory
LHC	Large Hadron Collider
SPS	Super Proton Synchrotron
PHENIX	Pioneering High Energy Nuclear Interacton eXperiment
STAR	Solenoid Tracker At RHIC
BRAHMS	Broad RAnge Hadron Magnetic Spectrometer
BES	Beam Energy Scan
CEP	Critical Endpoint
BBC	Beam-Beam Counter
DC	Drift Chamber
PC	Pad Chamber
PbSc	Lead Scintillator
TOF	Time-Of-Flight
PMT	Photo-Multiplier Tube
RPC	Resistive Plate Chamber
MRPC	Multi-gap Resistive Plate Chamber
BEMC	Barrel Electromagnetic Calorimeter
TPC	Time Projection Chamber
MTD	Muon Telescope Detector
VPD	Vertex Position Detector
EPD	Event Plane Detector
MWPC	Multi-Wire Proportional Chamber
PID	Particle Identification
NSII	Narrabri Stellar Intensity Interferometer
HBT	Hanbury-Brown-Twiss
BP	Bertsch-Pratt
LCMS	Longitudinal Co-Moving System
PCMS	Pair Co-Moving System
DCA	Distance of Closest Approach
SL	Splitting Level
FMH	Fraction of Merged Hits

Part I

INTRODUCTION TO HEAVY-ION PHYSICS AND FEMTOSCOPY

Before we get started, does anyone want to get out?

— Steve Rogers [10]

1

EXPLORING THE PROPERTIES OF THE QUARK-GLUON-PLASMA

Turning back the wheel of time by nearly 14 billion years would bring us back to the beginning of the Universe, the Big Bang. According to today's scientific consensus, at the beginning of time, around the first microseconds, the Universe was filled with a hot and dense matter called Quark-Gluon-Plasma (QGP) [11]. As the Universe started to expand and cool down, the temperature dropped below $10^{12}K$, and the quarks and gluons stuck together to form complex particles called hadrons. The first protons and neutrons, the basic building blocks of nuclei, were created. To observe and investigate the properties of the QGP, one has to collide heavy-ions (nuclei abundant in protons and neutrons) with enormous energy, so the conditions in these "little bangs" would resemble those at the beginning of the Universe.

In this chapter, I briefly review the history of heavy-ion physics and introduce the measurements that led to the discovery of the strongly-interacting Quark-Gluon-Plasma.

1.1 A BRIEF HISTORY OF HEAVY-ION PHYSICS

The search for the fundamental building blocks of matter has been an important objective of science since the 6th century BC [12]. During the course of history, smaller and smaller particles have been discovered, and the notion of an elementary particle has gone through many changes. As the experimental resolution improved, molecules, atoms, and nuclei all turned out to be made of smaller constituents. There was a brief period when it seemed that everything could be made out of only three kinds of particles – electrons, protons, and neutrons. However, the technological and scientific developments of the mid-19th century opened up a whole new world of particles. Studies of cosmic rays and advancements in particle accelerator and detector technology led to a perplexing variety of seemingly elementary (but mostly unstable) particles. Studying the interactions and decays of the different species within this newly discovered particle zoo shed

light on interesting symmetries and orderings which could predict the existence of new particles and gave rise to the quark model. The culmination of these discoveries was the development of the Standard Model of particle physics, a theory describing three of the four fundamental forces known to exist in the Universe (omitting only gravity). It includes the strong interaction responsible for binding quarks and gluons into hadrons, the weak interaction responsible for various forms of decays, and the electromagnetic interaction, a long-range force responsible for various phenomena such as atomic electron shell structure and chemical bonds.

The part of the Standard Model that describes the strong interaction is called Quantum Chromo Dynamics (QCD) [13]. Under normal circumstances (at low energies), quarks and gluons are confined to hadrons that are neutral in terms of QCD color charge [14]. However, at extremely high energies, the strength of the interaction between quarks and gluons decreases; this feature of QCD is called asymptotic freedom [15, 16]. These early discoveries of the properties of QCD predicted the possibility of a transition from the hadronic phase to a quark and gluon dominated phase, the QGP [17–22]. This transition was then proposed to be studied in high-energy heavy-ion collisions [20, 23, 24].

Around the early 1980s, a renaissance period of heavy-ion physics started. Extensive research programs got funded at the Bevatron of Lawrence Berkeley National Laboratory (LBL) [25], the Alternating Gradient Synchrotron (AGS) [26] and the Relativistic Heavy Ion Collider (RHIC) [27, 28] of Brookhaven National Laboratory (BNL), and the Super Proton Synchrotron (SPS) and Large Hadron Collider (LHC) of CERN [29]. These large scale international efforts eventually led to the discovery of this new phase of matter at RHIC [30–33] which was later confirmed and refined by LHC [34–36].

In the following, I review some of the important early experimental results and discuss the current status of research on QGP.

1.2 MILESTONES IN THE DISCOVERY OF QGP

Today it is established that in high-energy heavy-ion collisions, quarks and gluons become deconfined, and a strongly interacting QGP is created. After a quick ($\sim$1 fm/c) thermalization process, it rapidly

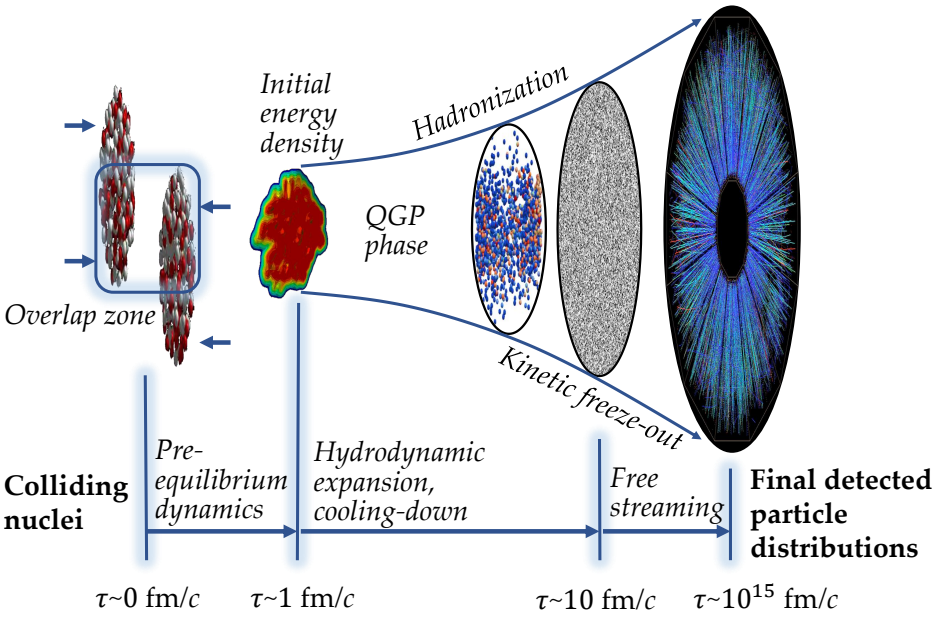

Figure 1.1: Time evolution of a relativistic heavy-ion collision.

expands and cools down. In about 10 fm/c, the temperature drops to the order of a few terakelvins, and quarks and gluon freeze out into hadrons. The expanding hadron gas further cools down, and after the last elastic scattering, the momenta of the particles becomes fixed; this is called kinetic freeze-out. The created hadrons (and their decay products) are then freely streaming into the detectors surrounding the collision point. This process is illustrated in Figure 1.1, and an example of an actual reconstructed Au+Au collision event is shown in Figure 1.2. Using complex detector systems such as the Pioneering High Energy Nuclear Interacton eXperiment (PHENIX) or the Solenoid Tracker At RHIC (STAR), it is possible to measure the properties (e.g., energy, momenta) of the particles created in these collisions. Subsequently, measuring distributions and correlations of these particles can provide information about the particle emitting source, the QGP.

The observations that the system created in these collisions is strongly-coupled and exhibits fluid-dynamic behavior required a paradigm shift; based on asymptotic freedom the expectation was a weakly coupled QGP. At even higher temperatures and/or baryon density, QCD is still expected to become weakly coupled [37].

1.2.1 *Strongly coupled quark matter*

Heavy-ion collisions are not always head-on; the colliding nuclei can be shifted relative to one another. To what extent they overlap is described by a vital quantity called centrality (illustrated on Figure 1.3). Head-on collisions are called central, while collisions with large im-

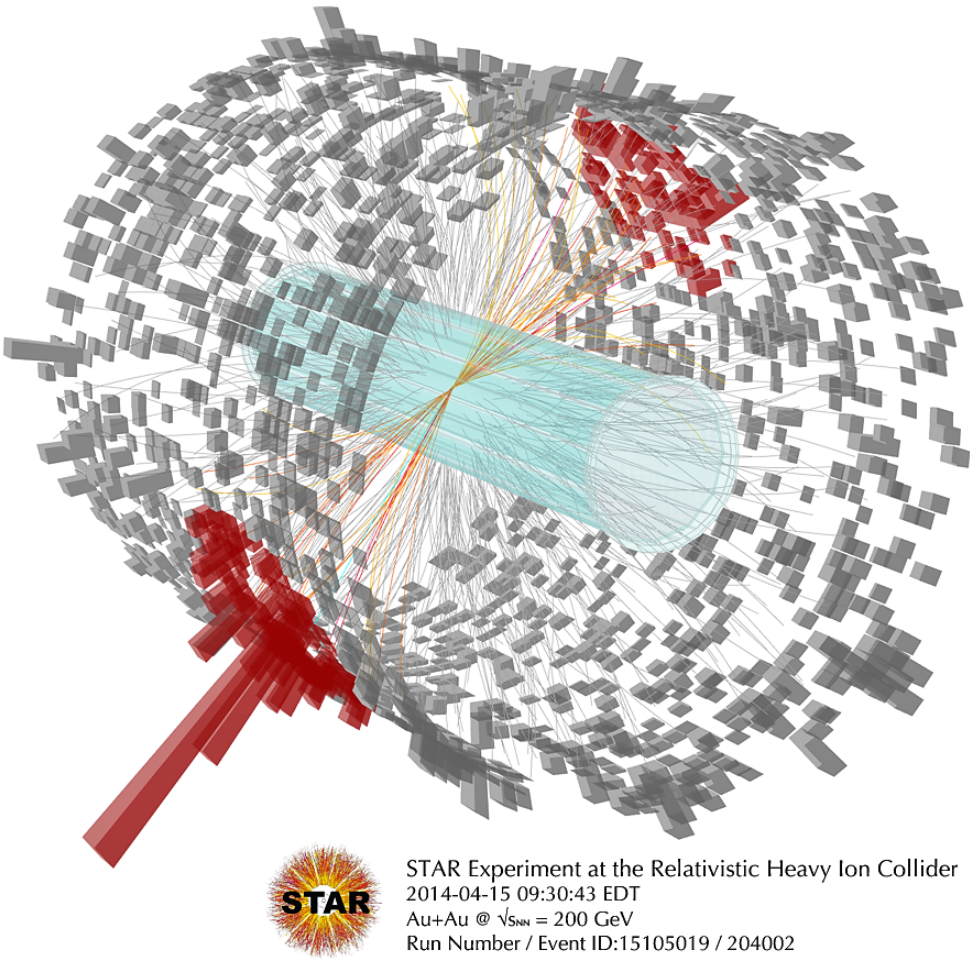

Figure 1.2: An example reconstructed high energy Au+Au collision at STAR.

pact parameter are called peripheral. Centrality is usually given in percentages, where 0% is completely central, and 100% is completely peripheral. Using the Glauber-model [38], for a given centrality, it can be determined how many nuclei took part in the collision and how many binary nucleon-nucleon collision happened. If a collision is thought of as the sum of many binary collisions, then the number of created particles (the multiplicity) is expected to be the same as the multiplicity of proton-proton collisions multiplied by the number of binary collisions. To quantify this, one can define the nuclear modification factor:

$$R_{AA} = \frac{\text{(Au+Au multiplicity)}}{\text{(number of binary collisions)} \times \text{(p+p multiplicity)}}. \quad (1.1)$$

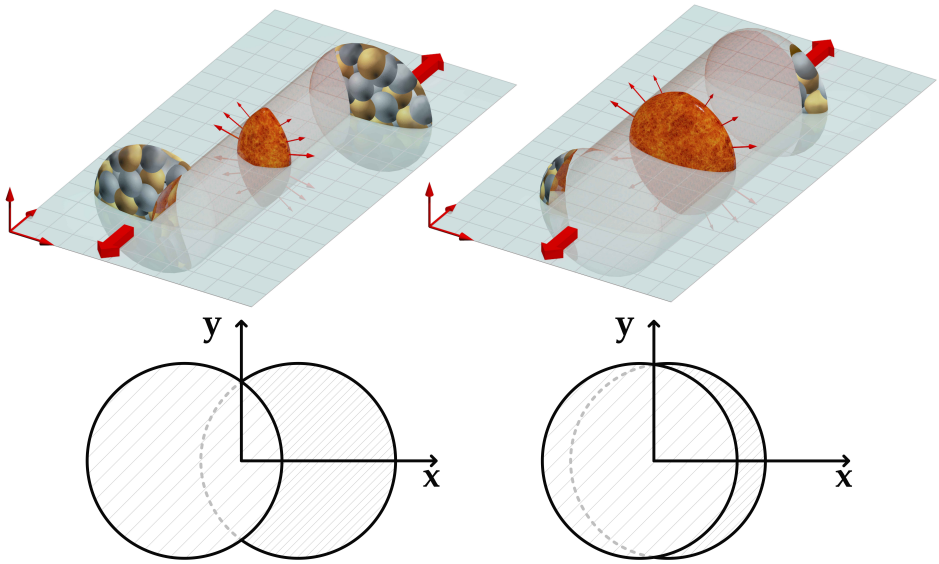

Figure 1.3: An illustration of a peripheral and a central heavy-ion collision.

Measurements of this parameter showed that in central heavy-ion collisions, much less high energy hadron is created than expected from proton-proton collisions, as shown in Figure 1.4. The explanation for this effect was that the matter created in these collisions is strongly coupled and absorbs the energy of strongly interacting particles with nonzero color charges. The modification factor of direct photons in heavy-ion collisions was found to be around unity [39], and that of hadrons in deuteron-gold collisions and peripheral gold-gold collisions was also similar due to the small size of the system [30, 31]. These measurements further corroborated the hypothesis of a strongly coupled plasma. Later it was found that the suppression effect decreases at lower collision energies [40], so finding the collision energy where the QGP is already created became one of the essential goals of heavy-ion physics.

In high-energy physics, a narrow cone of high-energy hadrons produced by the hadronization of a quark or gluon is called a jet. In collisions of small systems, they are often produced in pairs, going out in opposite directions. However, in a strongly coupled QGP, the appearance of single jets is much more frequent, a suppression of back-to-back correlations is observed. This effect is called jet-quenching and is also a strong sign of a strongly coupled QGP [30, 31].

1.2.2 *Perfect fluid*

Another important observation in heavy-ion collisions was that the spectra of particles at low momentum follow a Boltzman-distribution of $\exp(-E/k_B T)$, i.e., the system is thermodynamically equilibrated. Hydrodynamic calculations [41, 42] assuming an expanding system suggest a simple $T = T_0 + u^2 m$ relation, where T is referred to as

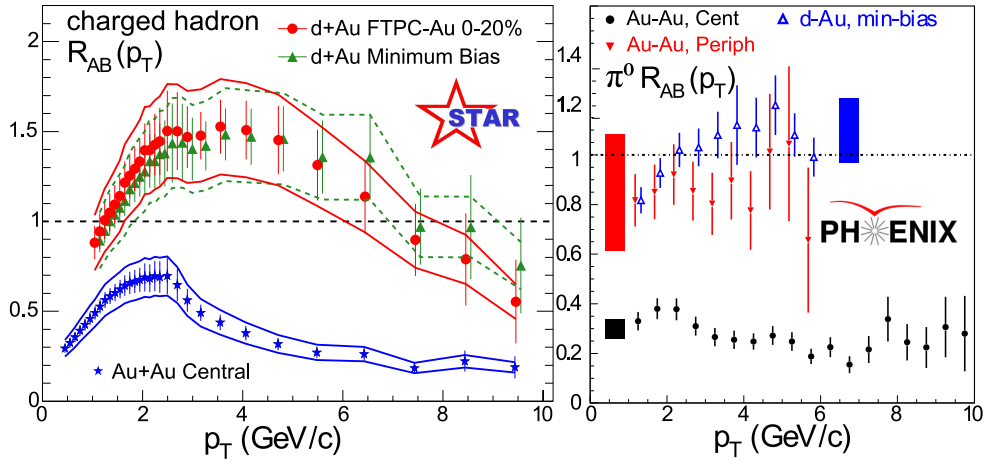

Figure 1.4: Binary-scaled ratio $R_{AB}(p_T)$ (where AB is either AuAu or dAu) of charged hadron and π^0 inclusive yields from 200 GeV Au+Au and d+Au collisions relative to that from p+p collisions, from STAR [31] (left) and PHENIX [30] (right).

It is important to note that already before these discoveries, a possible limiting temperature of the hadron gas was suggested by the statistical bootstrap model of Hagedorn [43] (about 158 MeV) and by early lattice-QCD calculations [44].

the inverse slope parameter or effective temperature, T_0 is the kinetic freeze-out temperature of the system, m is the mass of a given particle type, and u is the expansion velocity. One can test this relation experimentally by extracting the effective temperature values from exponential fits to different particle yields. It turned out that indeed a linear mass dependence is seen in experiments, and a freeze-out temperature of about 177 MeV was obtained in 200 GeV Au+Au collisions [42]. This was later refined by new experimental measurements and lattice-QCD calculations [45], and today the freeze-out parameters are measured for a vast variety of collision energies and centralities [46].

Besides these important measurements, it is also crucial to check whether the initial temperature in the collision was high enough to create QGP. PHENIX measured this through direct photons [47] and found that the initial temperature is well above the previously discussed limiting temperature.

Another observable well suited to test the hydrodynamical picture of heavy-ion collisions is the azimuthal asymmetry. If the collision is not perfectly central, the created system will have an ellipsoidal (almond-like) shape which can create an asymmetry in the momentum distribution of particles created from the hadronization process. In case of a strongly coupled QGP, the mean free path of quarks and gluons is small, and a geometrical asymmetry in this fluid-like state results in a strong momentum-space asymmetry in the created particles. To quantify this, one can investigate the Fourier-decomposition of the invariant momentum distribution in the azimuth angle (the direction in the transverse plane perpendicular to the beam direction):

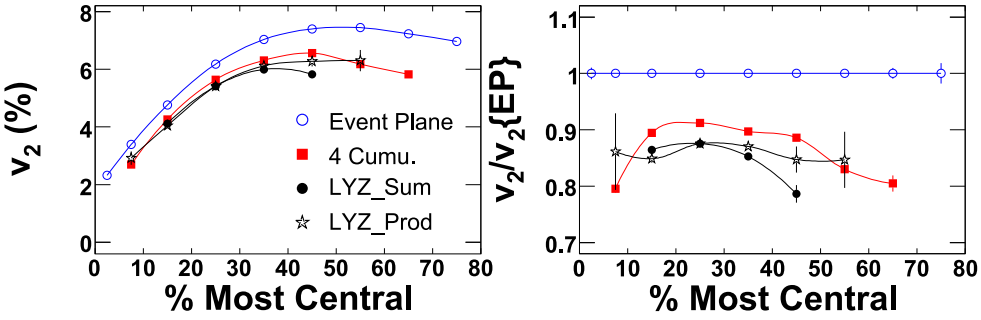

Figure 1.5: A STAR result for the p_T integrated charged hadron v_2 as a function of geometrical cross-section, measured with four different methods [50].

$$N(p_T, \phi) = N(p_T)\left[1 + 2\sum v_n \cos\left(n(\phi - \Psi_{RP})\right)\right], \tag{1.2}$$

where p_T is the transverse momentum, ϕ is the azimuth angle, v_n are the flow coefficients, and Ψ_{RP} is the reaction-plane angle. Due to symmetry reasons, the sine terms in the decomposition, as well as the odd coefficients, are negligible. The first significant coefficient is the elliptic flow, v_2, which is the angle average of $\cos(2\phi)$. This provides a measure of the deviation from spherical symmetry in the reaction plane. Experimental results showed that this coefficient is indeed non-negligible in high-energy heavy-ion collisions [49, 50] which supports the hydrodynamic picture of QGP. A STAR measurement for v_2 as a function of centrality is shown in Figure 1.5. It can be clearly seen that more peripheral collisions lead to higher elliptical asymmetries (as suggested also by Figure 1.3). Since these first results, elliptic flow has been extensively measured for many different particle types (such as different hadrons, photons [51], heavy quarks [52]), at many different collision energies [34, 53, 54].

Although in a simple model, the odd terms vanish due to symmetry, realistically, event-by-event fluctuations can lead to nonzero odd terms [48].

The next even coefficient, v_4 is connected to the viscosity of the QGP fluid. A non-negligible viscosity of the expanding fluid would suppress the hexadecapole asymmetry, however, measurements showed that v_4 values are also significant [55]. This observation, coupled with results from heavy quark R_{AA} and v_2 measurements [56] implicated that the specific shear viscosity (the ratio of the shear viscosity η to the entropy density s) of the system is extremely small, i.e., QGP is a near perfect fluid [57].

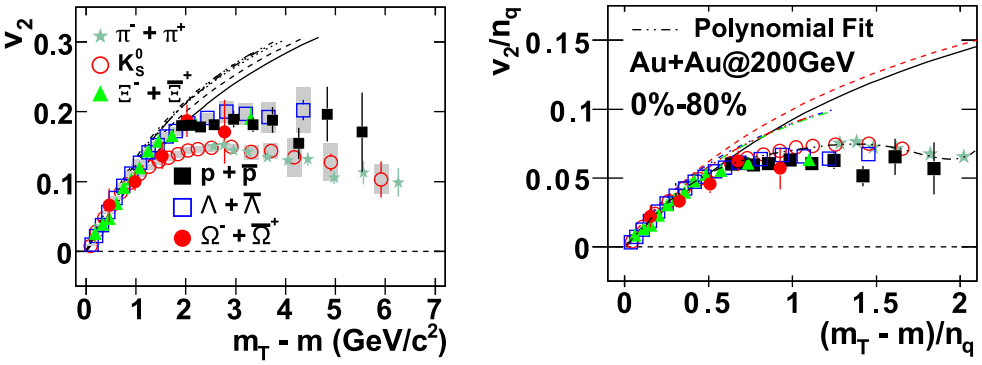

Figure 1.6: Constituent quark scaling of elliptic flow for different hadrons in 200 GeV Au+Au collisions measured by the STAR experiment [50].

1.2.3 *Quark degrees of freedom*

Another important milestone in early QGP research was the discovery of an interesting scaling behavior of the elliptic flow. In measurements of v_2 versus transverse kinetic energy ($KE_T = m_T - m = \sqrt{p_T^2 + m^2} - m$) a universal scaling behavior was observed. Elliptic flow values, in this case, follow two separate universal curves, one for mesons and another for baryons. When one divides both v_2 and KE_T with the number of constituent quarks, everything falls on the same curve, as shown in Figure 1.6. This observed scaling indicates that the hadrons are formed via a coalescence process [50, 58], and in the deconfined state, constituent quarks are the main degrees of freedom.

1.3 UNCHARTED TERRITORIES OF THE QCD PHASE DIAGRAM

Many important discoveries have already been made from the early measurements of top RHIC energy Au+Au reactions at $\sqrt{s_{NN}}$=200 GeV. The matter created in these conditions is strongly coupled; it suppresses even extremely high-energy particles on femtometer distances. The mean free path of particles within the matter is small, it exhibits fluid-like properties. Its specific shear viscosity is negligible; it is an almost perfect fluid. The initial temperature is exceptionally high, and quarks are its main degrees of freedom. Although today many properties of QGP are precisely measured, there are still many open questions and ongoing new theoretical and experimental efforts.

Besides the many experimental developments at RHIC and LHC, on the theoretical side, lattice QCD became refined and more powerful

as well. The conditions in heavy-ion collisions at the top RHIC energy and LHC energies are close to vanishing baryochemical potential ($\mu_B = 0$), which is a region lattice QCD can precisely explore. The simulations at $\mu_B = 0$ showed that the transition from QGP to a hadronic phase is a crossover, with a freeze-out temperature of about 155 MeV [45, 60–64]. Although now quite precise calculations can be done on the lattice at vanishing baryochemical potential, obtaining results for higher μ_B regions is significantly more complicated. Many model calculations suggest that in heavy-ion collisions corresponding to higher regions of baryochemical potential, the transition is first-order [65–69]. This is now supported by experimental results as well from STAR [70]. The point where the first-order transition ends is the Critical Endpoint (CEP), where the phase transition is second-order. These ideas can be summarized in a conjectured phase diagram shown in Figure 1.7.

It is important to note that for typical conditions realized in heavy-ion collisions, the transition temperatures can be somewhat higher than the infinite volume values obtained from lattice calculations [59].

Of course, such a phase diagram is just schematic; very little is known about concrete values and phase boundaries. Exploration of these uncharted territories on the phase diagram is among the main goals of today's heavy-ion physics experiments. The way to increase net-baryon density and thus leave the proximity of the $\mu_B = 0$ region is to lower the center-of-mass collision energy [46, 71]. To study a wide range on the phase-diagram, a comprehensive scan of beam energies has been done at the Relativistic Heavy Ion Collider of Brookhaven National Laboratory [72]. The first phase of this Beam Energy Scan (BES) was conducted in 2010 with both the PHENIX and STAR experiments, and the next phase, now only with STAR taking data, started in 2019. This second phase of the beam energy scan included increased luminosity, smaller beam packages, and many detector improvements. To explore the phase diagram at even higher μ_B values, a complementary fixed-target program was also done at STAR, reaching values of more than 700 MeV in μ_B (3 GeV in collision energy) [70, 73, 74].

Besides the RHIC-BES, there are other experimental facilities around the world that can study the baryon-rich region of the phase diagram, such as the NA61/SHINE experiment at SPS [75] and the HADES experiment at GSI [76]. Among future facilities with similar goals is the CBM experiment at FAIR in Darmstadt [77], the MPD experiment at NICA in Dubna [78] and the HEF at J-PARC in Japan [79].

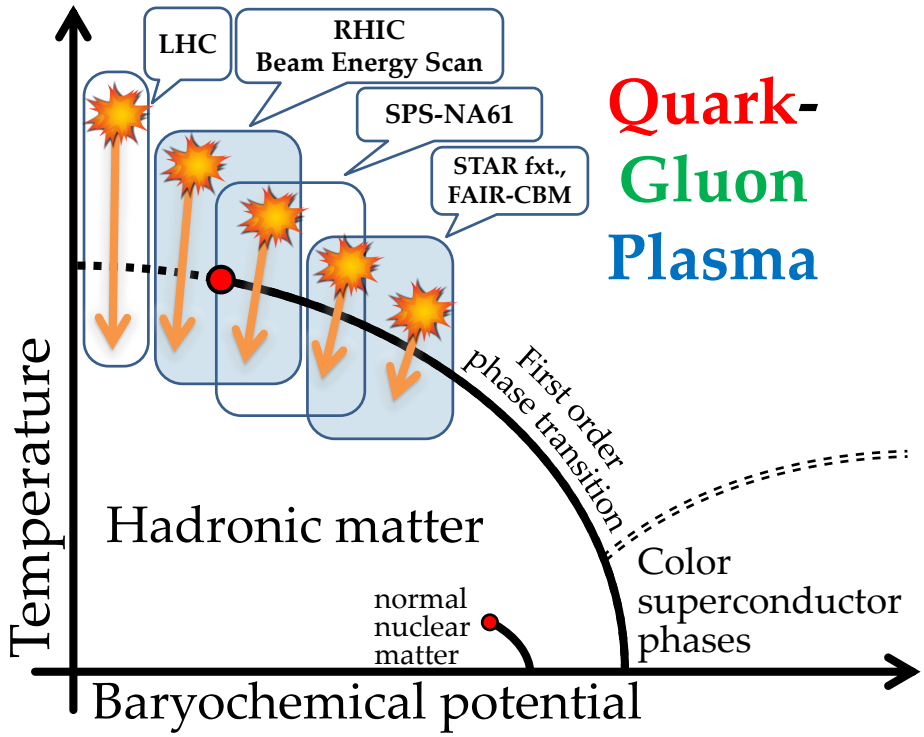

Figure 1.7: Conjectured phase diagram of QCD, with the possibly available ranges for different experimental facilities.

The first phase of the beam energy scan at RHIC already resulted in many exciting observations, and the ongoing data analysis of the second phase is even more promising. For a comprehensive review of recent results, see Ref. [80].

2

EXPERIMENTAL FACILITIES AT BNL-RHIC

Initially, four experiments operated at the Relativistic Heavy Ion Collider [81], as shown in Figure 2.1. Two of these, PHENIX [82] and STAR [83], are extensively discussed in this dissertation; the other two, the Broad RAnge Hadron Magnetic Spectrometer (BRAHMS) [84] and PHOBOS [85] were smaller experiments operating for a much shorter period of time. As discussed in the previous chapter, all four of these experiments played a vital role in the discovery of the strongly interacting QGP [30–33].

2.1 THE PHENIX EXPERIMENT

PHENIX was located at the Relativistic Heavy Ion Collider of the Brookhaven National Laboratory. After almost two decades of data taking, the experiment was decommissioned in 2016. The main goal of the PHENIX collaboration was (and still is) the search for a new state of matter, the QGP, and the investigation of its properties at different center-of-mass collision energies. One of the most important objectives of this mission was to create a map of the QCD phase diagram and study the forces that govern the fundamental building blocks of matter.

Although the detector system does not cover the full acceptance, it has outstanding energy- and momentum resolution. The schematics view of the experiment is shown in Figure 2.2. In the following, I briefly introduce the detectors playing an essential role in the analysis discussed in Chapter 4. A more detailed description can be found in Ref. [82].

2.1.1 *Event characterization detectors*

From the point of the analysis discussed in Chapter 4, the most crucial event characterization detector is the Beam-Beam Counter (BBC). The two arms of the BBC are located along the beamline, ± 144 cm from the center. This detector provides the minimum-bias trigger, which

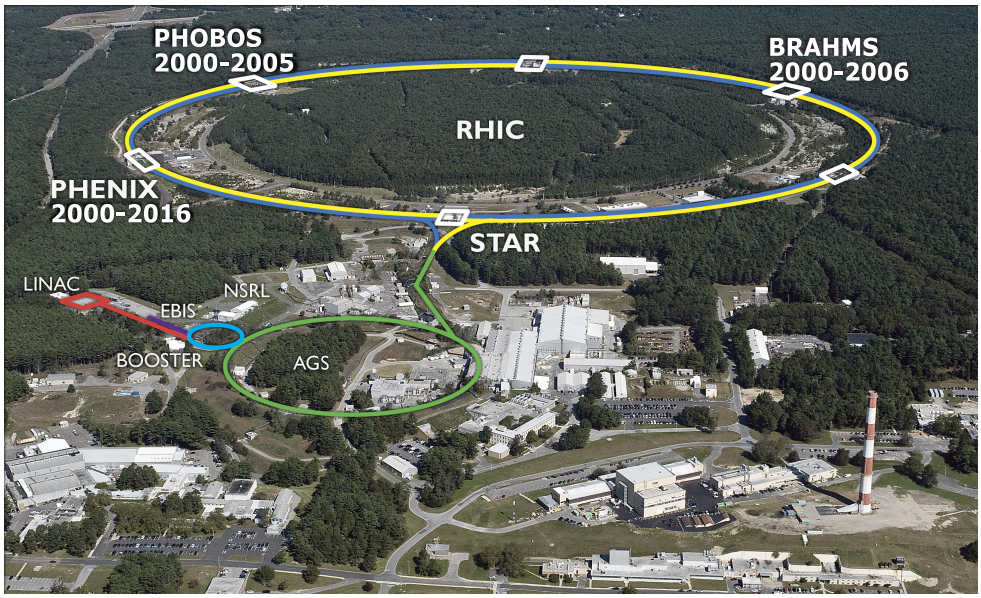

Figure 2.1: The Relativistic Heavy Ion Collider at Brookhaven National Laboratory.

requires hits in both arms in coincidence to record the given event. The charge deposited in the arms is also used to determine event centrality. The measured arrival-time difference in the two arms can be used to determine the collision vertex position along the beamline (z-axis). The time resolution is about 40 ps, so the z-vertex resolution for central and peripheral events is about 0.5 cm and 1.5 cm, respectively.

2.1.2 *Tracking detectors*

To reconstruct the tracks, PHENIX uses hits in different detector layers and the z-vertex position reconstructed by BBC. Detectors used for track reconstruction are the Drift Chamber (DC) and the first Pad Chamber (PC). DC-s are located at 202-246 cm radial distance from the beam, and measure the trajectories of particles in the transverse plane with about 1 mrad angle resolution. PC detectors are multi-wire proportional chambers located right behind the DC-s, and used for position measurement in both the φ and z direction, with about 1.7 mm z-resolution. Transverse momentum p_T is determined from the inclination angle measured by the DC-s, the z component of the momentum is determined by the PC1 z position and the BBC z-vertex.

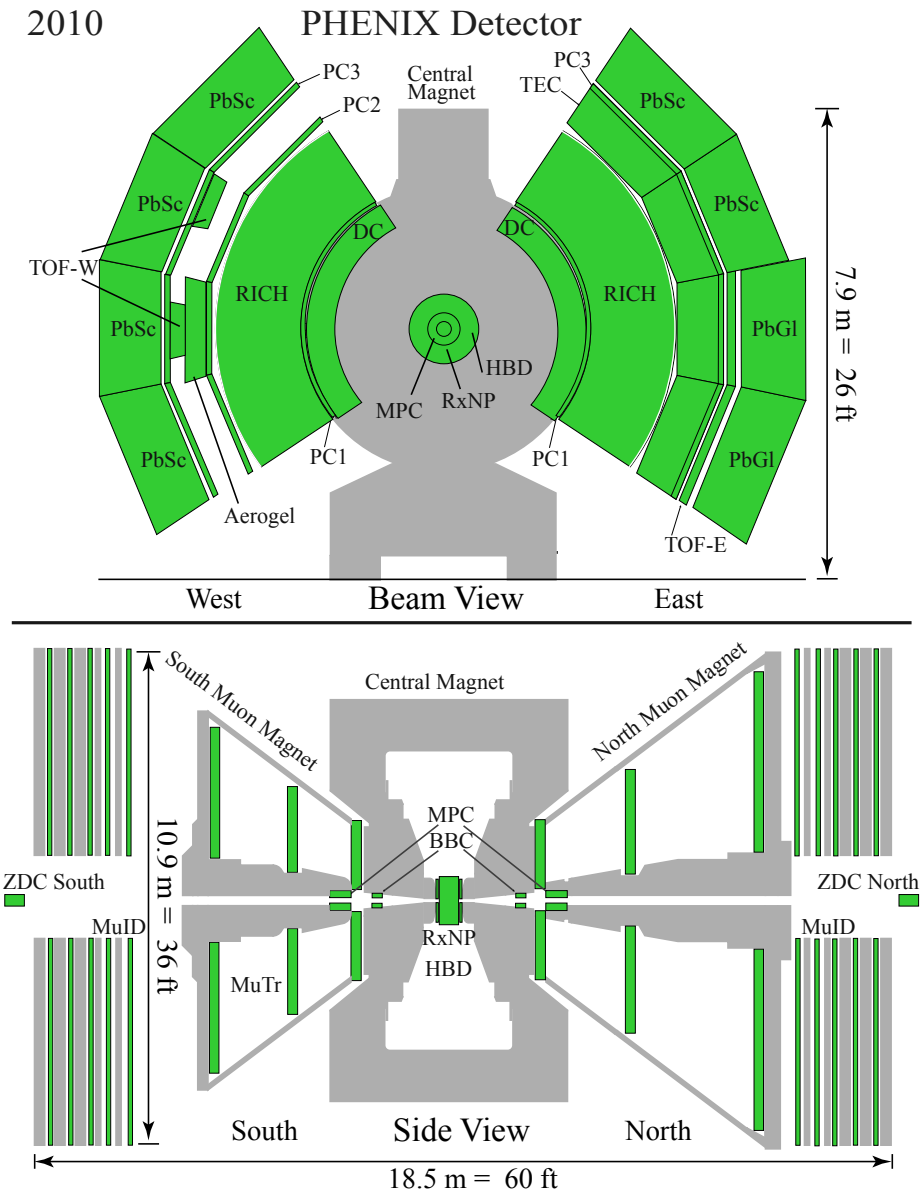

Figure 2.2: Schematics view of the PHENIX detector from the beam (top) and the side direction (bottom). This setup was used during the 2010 running period.

2.1.3 *Detectors used for particle identification*

Charged particles (in case of the analysis discussed in Chapter 4) are identified by the time of flight between the collision point and the outer detector layers. For this, one can use the Lead Scintillator (PbSc) electromagnetic calorimeters (in other notation EMC-E, EMC-W) in the east and west arms and the high-resolution Time-Of-Flight (TOF) detectors. PbSc is a highly segmented (containing 15552 separate

channels) sampling calorimeter located at about 5.1 m radial distance from the beam. After the energy-dependent calibrations, about 400-600 ps time resolution is achievable for pions. Situated at a similar distance from the beam is the TOF-E detector in the east arm, which consists of 960 plastic scintillators with Photo-Multiplier Tubes (PMTs). After calibrations, the obtained resolution is about 140 ps. The TOF-W detector in the west arm is a multi-gap Resistive Plate Chamber (RPC), with two panels located at about 4.8 m radial distance from the beam; its time resolution is about 90 ps.

For particle identification one needs the time-of-flight (t) provided by the BBC and PbSc/TOF detectors, the path-length (L) coming from the track-reconstruction, and the momentum (p) determined by DC/PC1. From these, one can reconstruct the mass-square for a given track:

$$m^2 = \frac{p^2}{c^2}\left[\left(\frac{ct}{L}\right)^2 - 1\right]. \tag{2.3}$$

If we plot the distribution of the particles on a two-dimensional histogram as a function of the reconstructed mass and the charge-momentum product, the pion, kaon, and proton hits are well separated. Using cuts on this distribution, one can get the identified pion sample without sizable contamination from kaons and protons – for this, an example is shown in Chapter 4.

2.1.4 *PHENIX and the RHIC Beam Energy Scan*

Results of high energy experiments (at maximum RHIC energies and LHC energies) coincide with the theoretical expectation [60] that the quark-hadron phase transition is a cross-over transition. At lower energies, however, a first-order transition is expected [70] – this indicates that there could be a CEP in between. Locating and characterizing this point is one of the most important objectives of today's high-energy heavy-ion physics. To be able to study the phase diagram of strongly interacting matter, one needs to conduct measurements at various collision energies and with various colliding nuclei. This was the primary goal of RHIC BES, during which PHENIX collected a vast variety (and amount) of data, as illustrated in Fig.2.3. The data I used for the analysis discussed in Chapter 4 are indicated with boxes.

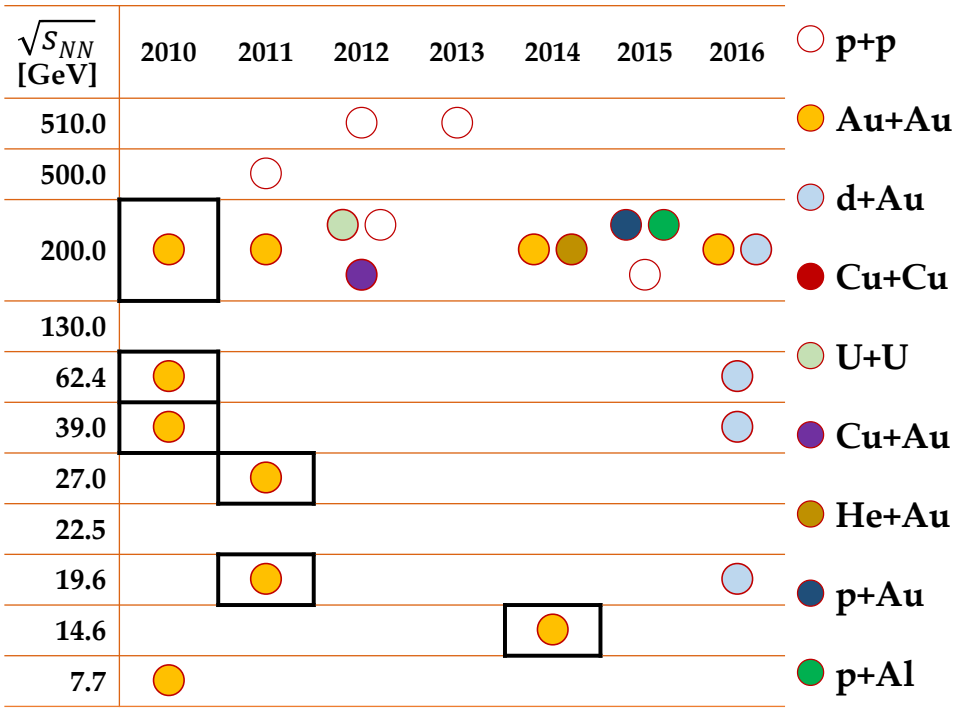

Figure 2.3: Summary of data taken during the first phase of the RHIC Beam Energy Scan program. The Au+Au datasets used for the experimental analyses detailed in Part ii. are indicated with black boxes.

2.2 THE STAR EXPERIMENT

STAR is currently the only active experiment at RHIC. The main goal of the experiment, similarly to PHENIX, is the investigation of the properties of QGP. The scientific goals also include the exploration of cold-QCD with polarized proton-proton collisions [86]. The first phase of the RHIC BES [87] already produced a number of interesting results including direct flow [88], net-proton cumulant [89], and di-electron [90] measurements. To further improve the precision of such results and push the boundaries of the phase-diagram exploration, a second phase of the beam energy scan was proposed along with many detector upgrades for STAR [91]. This second data-taking phase of RHIC was completed in 2021 [72]. It included increased luminosity at low energies, as well as a fixed-target program [92], and new types of collisions such as $Ru+Ru, Zr+Zr, O+O$ interactions. A summary of the Au+Au data taken during RHIC BES is shown in Figure2.4. Besides the study of the QCD phase diagram, STAR also investigated other interesting phenomena such as vorticity [93], the chiral mag-

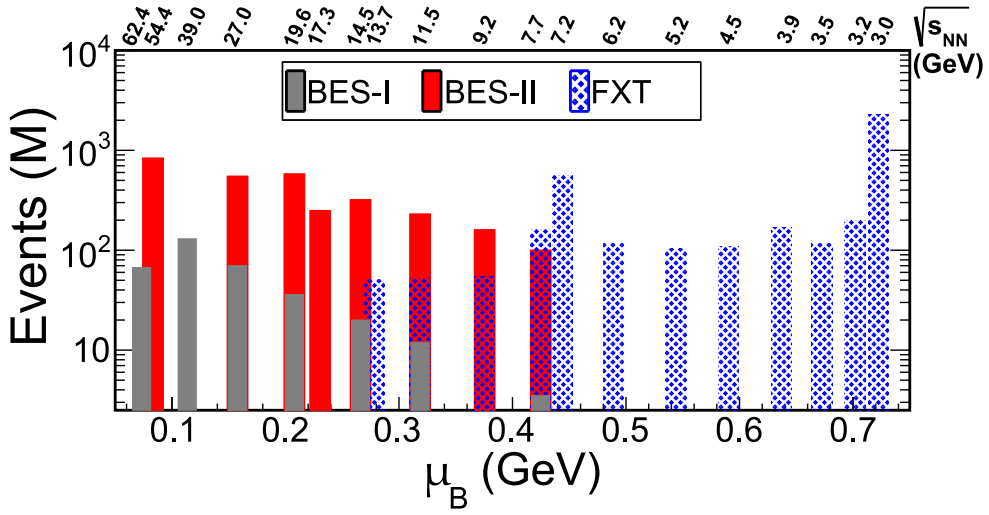

Figure 2.4: Summary of data taken by STAR during the two phases of the RHIC Beam Energy Scan.

netic effect [94], and the spin of the proton [95]. The schematics view of the experiment is shown in Figure 2.5. The setup shown in the Figure was in use during the first phase of the BES. Upgrades for the second phase included an inner expansion of the Time Projection Chamber (TPC) [96], an endcap TOF [97], and an Event Plane Detector (EPD) [98].

2.2.1 *Event characterization detectors*

The position of the primary vertex is measured with the Vertex Position Detector (VPD) [99]. It also provides the start time signal for the TOF and the Muon Telescope Detector (MTD). The detector is made up of two sets of PMTs surrounding the beam pipe, located at ± 5.7 meters from the center. One such set contains 19 PMTs, measuring pulses of photons from π^0 decays. The detector is fully integrated into the STAR trigger system and provides the primary input to the minimum bias triggers in A+A collisions.

Another important detector playing a crucial role in the STAR trigger system is the BBC. Similarly to VPD, it is made up of two sets of detectors (hexagonal scintillator tiles), located at ± 3.75 meters from the center. It is mainly used for polarized proton beam diagnostics, vertex position measurement, and event plane measurements [100].

One of the major detector upgrades for the second phase of the Beam Energy Scan was the EPD, a replacement for the BBC. It has

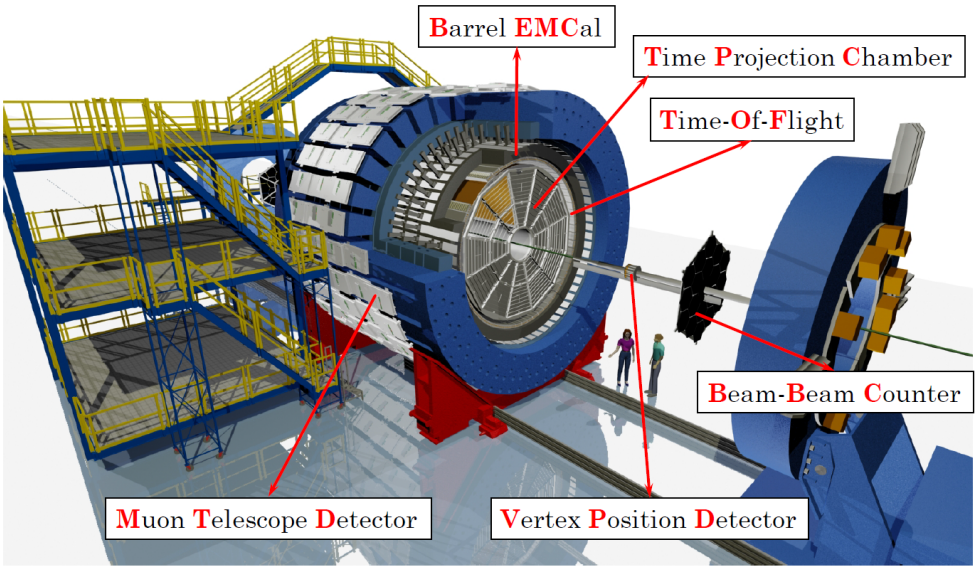

Figure 2.5: Schematic view of the STAR detector.

very similar functionality as the BBC, but its higher granularity and acceptance offer an improved performance [101].

2.2.2 *The Time Projection Chamber*

The main detector in STAR is a TPC, used for tracking, momentum reconstruction, and particle identification by energy-loss (dE/dx) [102]. It is a 4.2 m long cylindrical chamber with a diameter of 4 m, filled with a P10 gas mixture (90% argon, 10% methane). The detector is placed in the 0.5 T magnetic field of a solenoid. Its acceptance is $\eta \in [-1;1]$ in pseudo-rapidity, and full 2π coverage in azimuth angle ϕ. Charged particles ionize the gas mixture within the chamber, and the resulting electrons drift to the two ends in a uniform electric field of 135 V/cm, with a typical drift velocity of 5.45 cm/μs. The readout is based on a Multi-Wire Proportional Chamber (MWPC) approach with 136608 readout segments (pads). A schematics view of the TPC is shown on Figure 2.6.

2.2.3 *Detectors used for particle identification, triggering*

The purpose of the TOF detector at STAR is to improve particle identification at high momentum ($p_T > 1$ GeV/c) [103]. A full barrel TOF with 2π azimuth angle acceptance started to take part in data taking in late 2008 [104, 105]. The detector system is based on small

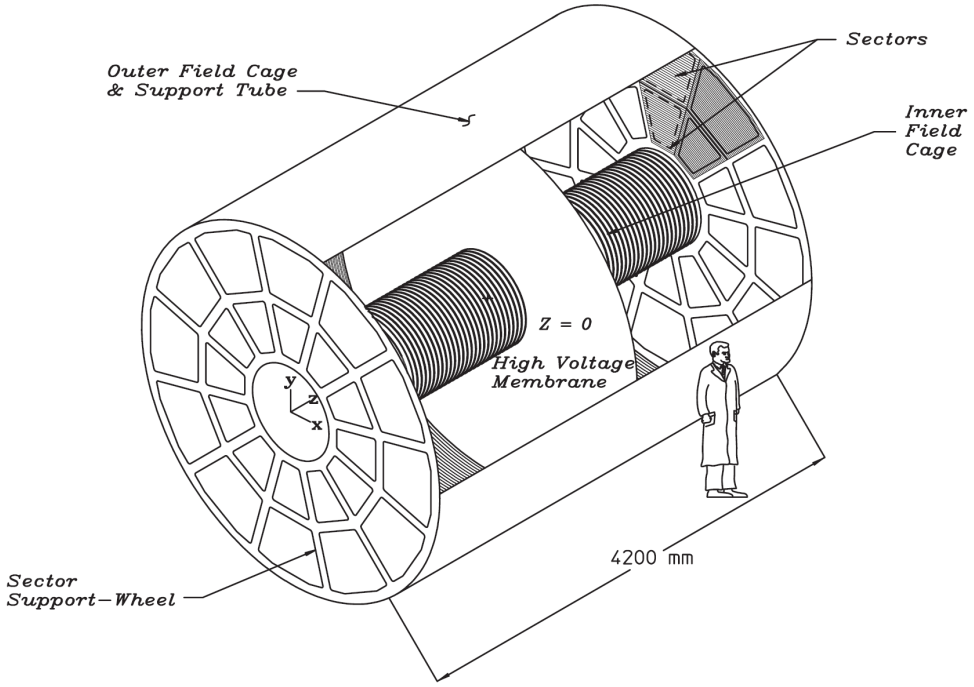

Figure 2.6: Schematics view of the STAR Time Projection Chamber.

Multi-gap Resistive Plate Chamber (MRPC)-s surrounding the TPC. By measuring the time of flight of the particles from the collision point to the detector, the speed of the particles can be calculated. Combining this information with the momentum measured by the TPC, the mass-square distribution of the particles can be reconstructed and used for particle identification (as shown in Equation 2.3).

Another detector layer surrounding the TPC is the Barrel Electromagnetic Calorimeter (BEMC) [106]. This detector is utilized to trigger on and study rare, high p_T processes (jets, leading hadrons, direct photons, heavy quarks) and provide large acceptance for photons, electrons, π^0 and η mesons. It includes a total of 120 calorimeter modules, matching the acceptance for full TPC tracking.

Outside the STAR solenoid, there is a final detector layer, the MTD. This is another large-area TOF system based on much larger MRPCs, which primary purpose is muon identification [105].

3

FROM STARS TO QUARKS – INTENSITY CORRELATIONS ON COSMIC AND NUCLEAR SCALES

One of the most extensively studied sub-fields of high-energy nuclear and particle physics is called femtoscopy. It includes measurements on the femtometer (1 fm = 10^{-15} m) length- and fm/c time-scales and delves into the study of intensity correlations. The well-established methods of such intensity correlation measurements in high-energy physics date back to the 1960-s and originate from a different field of science, radio-astronomy.

The term femtoscopy was coined by R. Lednicky more than two decades ago [107].

3.1 RADIO ASTRONOMY AND HBT-CORRELATIONS

The earliest intensity correlation measurements were performed in radio and optical astronomy by Robert Hanbury Brown and Richard Q. Twiss at the Jodrell Bank Observatory at the University of Manchester [108, 109]. They developed a novel method to measure the angular diameters of main sequence stars by changing the distance between two telescopes on the scale of just a few meters and measuring the correlation in the intensity fluctuations of light coming from the point-like source on the sky. To ensure that their method has a solid theoretical base, they conducted tabletop optical experiments as well [110, 111]. After the initial success, Hanbury Brown and Twiss moved on to Australia to continue their experiments on a larger scale. They founded the Narrabri Stellar Intensity Interferometer (NSII) [115], which had a maximal baseline of 188 meters and a reflector diameter of 6.5 meters. An illustration of this observatory is shown in Figure 3.1. The experimental program was running from 1964 to 1972, during which they measured the angular diameters of 32 stars [116, 117].

The successful application of the intensity correlation techniques in not just radio but optical interferometry caused a controversy among scientists, mainly because the theory of coherent light and lasers was not established yet. This was resolved later by R. J. Glauber [112], whose work provided the basis for a new field of science, quantum-optics [113, 114].

The fundamental idea behind HBT interferometry can be demonstrated with a simple calculation, as detailed in for example Ref. [118]. Let us take two point sources of light (of the same wavenumber, k), a and b, and imagine measuring their light with two independent telescopes A and B, as illustrated in Figure 3.2. Let us assume that

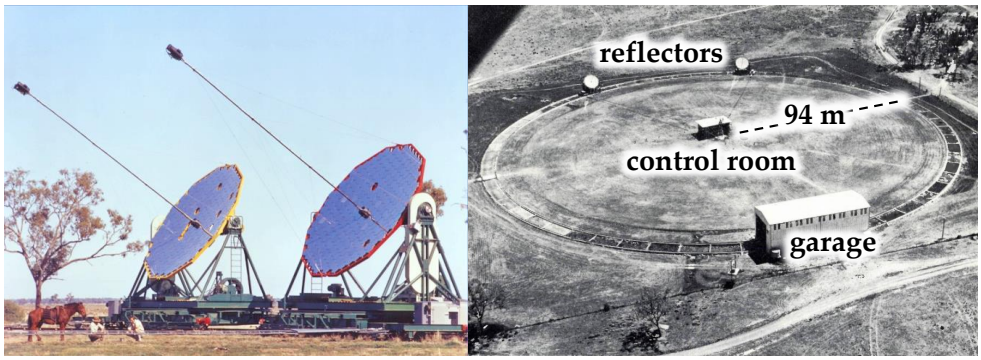

Figure 3.1: The Narrabri Stellar Intensity Interferometer [115].

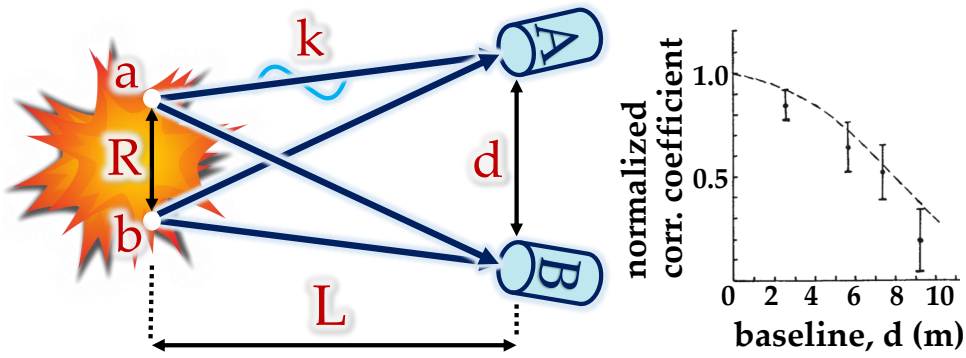

Figure 3.2: Schematic illustration of the Hanbury-Brown-Twiss (HBT) measurement and the original result for Sirius (α Canis Majoris A)) from ref. [109]. The dashed line on the right figure corresponds to the theoretical values calculated for a uniformly illuminated disk of diameter 0.0063".

the spatial separation of the sources is R, and that of the detectors is d, furthermore assume that the distance L from the sources to the detectors is much larger than these separations ($L \gg R \gg d$). The amplitudes of the spherical electromagnetic waves produced by the sources can be written as $\alpha \exp(ik|\boldsymbol{r} - \boldsymbol{r_a}| + i\phi_a)/|\boldsymbol{r} - \boldsymbol{r_a}|$ for source a, and $\beta \exp(ik|\boldsymbol{r} - \boldsymbol{r_b}| + i\phi_b)/|\boldsymbol{r} - \boldsymbol{r_b}|$ for source b. The ϕ_a and ϕ_b terms are random phases, and polarization is ignored. The total amplitude in detector A can be written as

$$A_A = \frac{1}{L}\left(\alpha e^{ik\boldsymbol{r_{Aa}}+i\phi_a} + \beta e^{ik\boldsymbol{r_{Ab}}+i\phi_b}\right). \tag{3.4}$$

The intensity in detector A is the absolute square of the amplitude:

$$I_A = \frac{1}{L^2}\Big(|\alpha|^2+|\beta|^2+\alpha^*\beta e^{i(k(\boldsymbol{r_{Ab}}-\boldsymbol{r_{Aa}})+\phi_b-\phi_a)}+ \\ + \alpha\beta^* e^{-i(k(\boldsymbol{r_{Ab}}-\boldsymbol{r_{Aa}})+\phi_b-\phi_a)}\Big). \tag{3.5}$$

The average intensity in the two detectors will be the same since the exponential terms vanish due to the random phases:

$$\langle I_A \rangle = \langle I_B \rangle = \frac{1}{L^2} \left(\langle |\alpha|^2 \rangle + \langle |\beta|^2 \rangle \right). \tag{3.6}$$

The product of the average intensities does not depend on the detector separation. However, if we take the average after multiplying the intensities, an extra non-vanishing term will appear:

$$\langle I_A I_B \rangle = \langle I_A \rangle \langle I_B \rangle + \frac{2}{L^4} \langle |\alpha|^2 \rangle \langle |\beta|^2 \rangle \cos\left(k(\boldsymbol{r_{Aa}} - \boldsymbol{r_{Ba}} - \boldsymbol{r_{Ab}} + \boldsymbol{r_{Bb}})\right). \tag{3.7}$$

Using the $L \gg R$ approximation, the intensity correlation function as a function of the detector separation can then be written as

$$C(d) = \frac{\langle I_A I_B \rangle}{\langle I_A \rangle \langle I_B \rangle} \approx 1 + 2 \frac{\langle |\alpha|^2 \rangle \langle |\beta|^2 \rangle}{\left(\langle |\alpha|^2 \rangle + \langle |\beta|^2 \rangle \right)^2} \cos\left(\frac{kRd}{L}\right). \tag{3.8}$$

With a knowledge of the individual wavevectors, it is possible to measure the size of the source by varying the detector separation. If instead of two discrete point sources, we have a source distribution $\rho(\boldsymbol{r})$, then the correlation function turns out to be the Fourier-transform of the source function:

$$C(d) - 1 \sim \left| \int d^3 r \rho(\boldsymbol{r}) e^{i(\boldsymbol{k_A} - \boldsymbol{k_B})\boldsymbol{r}} \right|^2, \tag{3.9}$$

where $\boldsymbol{k_i}$ is the wavevector of the light seen in detector i.

3.2 FEMTOSCOPY IN HEAVY-ION PHYSICS

Independently from the HBT experiments, G. Goldhaber and his collaborators found an analogous effect in high-energy proton-antiproton collisions. While looking for the ρ meson, they observed an enhancement in intensity correlations of identical charged pions [119]. The results were explained by G. Goldhaber, S. Goldhaber, W-Y. Lee, and A. Pais using the approach of Bose-Einstein symmetrized wave function of pions [120]. In nuclear- and particle physics these correlations analogous to the HBT effect are also called GGLP- or Bose-Einstein correlations. Similarly to Equation 3.9, it can be shown that the two-

particle Bose-Einstein correlation function is connected to the Fourier-transform of the source-function (see details in section 3.2.1). By measuring such correlation functions in high-energy heavy-ion physics, one can explore the particle-emitting source on the femtometer scale.

Correlated particle emission can have multiple reasons, such as jets, resonance decays, conservation laws. In heavy-ion collisions, the primary source of correlation for identically charged pion pairs at low relative momentum is the quantum-statistical Bose-Einstein, or HBT effect. These correlations stem from the indistinguishability of identical bosons (the symmetric pair wavefunction). Bose-Einstein correlations scale with the average number of particle pairs, which is proportional to the square of the average multiplicity. Other possible sources of correlation scale linearly with the average multiplicity; hence in high-multiplicity heavy-ion collisions at low relative momentum, Bose-Einstein correlations dominate.

At the Relativistic Heavy Ion Collider investigations related to Bose-Einstein correlations played a crucial role in the discovery of the strongly interacting QGP [30–33]. The scale parameters of the Gaussian phase-space density (often called HBT-radii) can be determined experimentally with correlation measurements. HBT-radii scale with the average transverse mass of the particle pairs as $R^{-2} \propto a + bm_T$, where $m_T = \sqrt{m^2 + k_T^2}$, m is the mass of the given particle-type (e.g. pions), and k_T is the average transverse momentum of the pairs. This scaling is more or less universal along centrality, particle type, center-of-mass collision energy, and the size of the colliding nuclei [121, 122]. This type of linear scaling can be explained in the framework of a strong longitudinal and radial hydrodynamical expansion. The Hubble-flow, where the expansion velocity is proportional to the distance, is an important property of QGP [123, 124]. Further details about Bose-Einstein correlations and their application can be found in the review articles of Refs. [125–130].

In the following subsections, I review the basic definitions and properties of femtoscopic correlations, with particular emphasis on the shape of the source function.

3.2.1 *Basic definitions*

The general definition of the two-particle correlation function as a function of the single particle four-momenta is the following:

$$C_2(p_1, p_2) = \frac{N_2(p_1, p_2)}{N_1(p_1)N_1(p_2)}, \tag{3.10}$$

where $N_1(p_1), N_1(p_2)$ and $N_2(p_1, p_2)$ are the one- and two-particle invariant momentum distributions. The pair momentum distribution can be calculated from the $S(x, p)$ source distribution and the $\Psi^{(2)}_{p_1,p_2}(x_1, x_2)$ symmetrized pair wave function:

$$N_2(p_1, p_2) = \int d^4x_1 d^4x_2 S(x_1, p_1) S(x_2, p_2) \left|\Psi^{(2)}_{p_1,p_2}(x_1, x_2)\right|^2. \tag{3.11}$$

Neglecting final-state interactions, the wave function can be described with plane waves, and its absolute square becomes

$$\left|\Psi^{(2)}_{p_1,p_2}(x_1, x_2)\right|^2 = 1 + \cos\left(p_1 - p_2\right)(x_1 - x_2). \tag{3.12}$$

Substituting this to equation 3.10, the correlation function without final-state effects (denoted by the (0) superscript) can be written as

$$C_2^{(0)}(p_1, p_2) = 1 + \Re\left\{\frac{\widetilde{S}(q, p_1)\widetilde{S}^*(q, p_2)}{\widetilde{S}(0, p_1)\widetilde{S}^*(0, p_2)}\right\}, \tag{3.13}$$

where $q = p_1 - p_2$ is the relative four-momentum, the $*$ superscript denotes the complex conjugate, and $\widetilde{S}(q, p)$ is the Fourier-transform of the source distribution:

$$\widetilde{S}(q, p) \equiv \int S(x, p) e^{iqx} d^4x. \tag{3.14}$$

In heavy-ion collisions, within typical kinematic regions the dependence of $\widetilde{S}(q, p)$ on p is much more smooth than the relative momentum q dependence [130]. Hence a usually used approximation is $p_1 \approx p_2 \approx K$, where $K \equiv (p_1 + p_2)/2$ is the average four-momentum of the pair. With this equation 3.13 can be written as

$$C_2^{(0)}(q, K) \simeq 1 + \frac{|\widetilde{S}(q, K)|^2}{|\widetilde{S}(0, K)|^2}. \tag{3.15}$$

The validity of these approximations was investigated in Refs. [127, 128] and for typically exponential single-particle spectra, the difference compared to more detailed calculations was found to be less than 5%.

Using the pair source (or spatial correlation function) $D(r, K)$, defined as

$$D(r, K) = \int S(\rho + r/2, K) S(\rho - r/2, K) d^4\rho, \tag{3.16}$$

equation 3.10 can be reinterpreted as

$$C_2(q, K) = \int d^4r D(r, K) \left|\Psi_q^{(2)}(r)\right|^2. \tag{3.17}$$

This way, instead of the single-particle variables p_1, p_2, x_1, x_2 one can use the following pair variables: the pair separation four-vector r, the pair center of mass four-vector ρ, the relative momentum q, and the average momentum K. Similarly, equation 3.15 becomes

$$C_2^{(0)}(q, K) \simeq 1 + \frac{\widetilde{D}(q, K)}{\widetilde{D}(0, K)}, \tag{3.18}$$

were $\widetilde{D}$ is the Fourier-transform of the pair source function:

$$\widetilde{D}(q, K) = \int D(x, K) e^{iqx} d^4x. \tag{3.19}$$

The Bose-Einstein correlation function is thus in direct connection with the Fourier transform of the pair-source function; that is the quantity that two-particle correlation measurements can reconstruct.

3.2.2 *Strength of the correlation function and the Core-Halo model*

Equation 3.18 shows that if final-state interactions are neglected, the value of the correlation function is 2 if the relative momentum q goes to zero: $C_2^{(0)}(q = 0) = 2$. However, the resolution of the detectors puts strong lower limits on the relative momentum measurement (around a few MeV/c), so experimentally one can only measure at non-zero relative momentum and extrapolate to $q = 0$. To quantify this extrapolated value, the correlation strength can be introduced as

$$\lambda \equiv \lim_{q \to 0} C_2(q) - 1. \tag{3.20}$$

Experimental observations often show $\lambda < 1$ values; this prompted the idea of the core-halo picture [131, 132]. In this model, the particle emitting source has two components: a hydrodynamically behaving fireball-like core, S_{core}, which contains particles created directly from the freeze-out (or from decays of short-lived resonances), and a surrounding halo, S_{halo}, which contains particles that are the decay products of long-lived resonances (such as $\eta, \eta', K^0_S, \omega$). This picture is particularly important for pions, but the general structure of the model may be relevant for other mesons as well. The size of the core is usually no more than 10-15 fm. However, halo pions can be created hundreds or thousands of femtometers from the collision point. Experimentally only the core part is relevant; the width of the Fourier transform of the halo is below the minimal resolvable momentum difference. Within this framework, an interpretation of the λ parameter is possible by reformulating equation 3.15:

$$C_2^{(0)}(q,K) \simeq 1 + \frac{|\widetilde{S}(q,K)|^2}{|\widetilde{S}(0,K)|^2} = 1 + \frac{|\widetilde{S}_{core}(q,K)|^2}{(N_{core}+N_{halo})^2} = \\ = 1 + \lambda \frac{|\widetilde{S}_{core}(q,K)|^2}{|\widetilde{S}_{core}(0,K)|^2}, \tag{3.21}$$

Here an important property of the Fourier transform is used; namely that the Fourier transform of any function $f(x)$ at x=0 is equal to the integral of that function: $\tilde{f}(x{=}0) = \int f(x)dx$.

where $\lambda = N^2_{core}/(N_{core}+N_{halo})^2$ is the squared ratio of the number of particles created from the core to the total number of particles.

If one assumes that the single-particle source has two components ($S = S_{core} + S_{halo}$), it follows that the pair source D will have three – a core-core, a core-halo, and a halo-halo component:

$$D = D_{(c,c)} + D_{(c,h)} + D_{(h,h)}. \tag{3.22}$$

Experimentally, however, similarly to the previous arguments, only the core-core part is relevant. Using the previously introduced correlation strength parameter λ and coupling the core-halo model with the Bowler-Sinyukov procedure [133, 134], the correlation function can be written as

$$C_2(q,K) = 1 - \lambda + \lambda \int d^4r D_{(c,c)}(r,K) \left|\Psi^{(2)}_q(r)\right|^2. \tag{3.23}$$

This form is often used in experiments to fit the measured correlation functions. To calculate the shape of the $C_2(q, K)$ two-particle correlation function, one needs an assumption on the shape of the pair source $D_{(c,c)}(r, K)$ (discussed in section 3.2.3), and a proper description of the effect of final state interactions enclosed in the $\Psi_q^{(2)}(r)$ pair wave function. A detailed calculation of the latter is discussed in Chapter 6.

There can be different reasons behind the experimentally observed deviation from unity in the λ parameter. Within the core-halo interpretation it could be explained for example with an in-medium mass modification of the η' meson [135–138], but other effects, such as partially coherent particle emission [126, 128, 131] could also result in a decrease in the correlation strength.

3.2.3 *The shape of the two-particle source-function*

Since the discovery of quantum statistical correlations of pions produced in high energy reactions [119, 120], more and more experimental data led to a refined understanding of the connection between such correlations and the actual source dynamics, as well as an increased expectation on phenomenological models to reproduce the observations. In heavy ion physics, the usual assumption for the source shape was Gaussian for many years. This was corroborated by phenomenological studies such as hydrodynamical model calculations (see e.g. Refs. [139, 140]). Recent results showed that one must go beyond this simple picture to achieve a statistically acceptable description of the measured correlation functions. The application of the source imaging technique discussed in Ref. [141] to correlation functions measured in high energy heavy ion collisions led to one of the first signs of non-Gaussian behavior in such reactions [142]; it was found that the two-pion source function indeed exhibits a power-law behavior. Since then, a lot of experimental as well as theoretical work has been done in this direction.

In rapidly expanding systems such as the hadron gas created in heavy-ion collisions, the variance of the elementary processes (independent random variables) might not be finite; the generalized central limit theorem suggests that the spatial distribution might be defined by a process called anomalous diffusion [143], stemming from the

time-dependent increasing mean free path of particles. In this case, the shape of the two-particle source could be described by Lévy-stable distributions. Recent experimental results indicate that for pion pairs, indeed such distributions may play the role of the source function [5, 9, 144, 145]. Besides anomalous diffusion, there could be other competing reasons behind the appearance of Lévy-distributions, such as jet fragmentation [146], critical behavior [147], event-averaging [3, 148, 149], resonance decays [3]. The latter two will be discussed in Chapter 7.

Stable distributions are of utmost importance when studying the limiting distributions of random variables based on a sum of elementary processes. It is well known that in case of one-dimensional random variables, the stable distributions can be given through the following formula:

$$f(x;\alpha,\beta,R,\mu) = \frac{1}{2\pi}\int_{-\infty}^{\infty}\varphi(q;\alpha,\beta,R,\mu)e^{iqx}dq, \tag{3.24}$$

where the characteristic function is given as:

$$\varphi(q;\alpha,\beta,R,\mu) = \exp\left(iq\mu - |qR|^{\alpha}(1 - i\beta\,\mathrm{sgn}(q)\Phi)\right), \tag{3.25}$$

$$\text{where } \Phi = \begin{cases} \tan(\frac{\pi\alpha}{2}), \alpha \neq 1, \\ -\frac{2}{\pi}\log|q|, \alpha = 1. \end{cases}$$

In case of heavy-ion collisions, the symmetric, centered ($\beta = 0$, $\mu = 0$) stable distributions may play a role of the source distribution if that results from a statistical process. In multiple dimensions, the situation is far less clear. It is, however, known that the following distribution in N dimensions is stable [150]:

$$\mathcal{L}(\boldsymbol{r};\alpha,R) = \frac{1}{(2\pi)^3}\int d^3\boldsymbol{q}e^{i\boldsymbol{q}\boldsymbol{r}}e^{-\frac{1}{2}|\boldsymbol{q}\mathbf{R}\boldsymbol{q}|^{\alpha/2}}, \tag{3.26}$$

from which in case of spherical symmetry ($R_{ij} = R^2\delta_{ij}$), one obtains

$$\mathcal{L}(\boldsymbol{r};\alpha,R) = \frac{1}{(2\pi)^3}\int d^3\boldsymbol{q}e^{i\boldsymbol{q}\boldsymbol{r}}e^{-\frac{1}{2}|\boldsymbol{q}R|^{\alpha}}. \tag{3.27}$$

The two main parameters of such distributions are the index of stability, α, and the scale parameter, R. The $\alpha = 2$ case corresponds

to the Gaussian distribution, while in case of $\alpha < 2$, the distribution exhibits a power-law behavior. In the latter case the tail can be described in three dimensions as $L(\boldsymbol{r}; \alpha, R) \propto (r/R)^{-(3-\alpha)}$, if $r/R \to \infty$ (and $r \equiv |\boldsymbol{r}|$). Similarly, for the angle averaged distribution:

$$r^2 L(\boldsymbol{r}; \alpha, R) \propto r^{-1-\alpha}. \tag{3.28}$$

The most important property of this distribution is that any moment greater than α is not defined, and it retains the same α under convolution of random variables. From the latter it is apparent that if the single particle source $S_{core}(\boldsymbol{r})$ is a Lévy-stable distribution, then the pair-source $D_{(c,c)}(\boldsymbol{r})$ also has a Lévy shape with the same index of stability α:

$$S_{core}(\boldsymbol{r}) = \mathcal{L}(\boldsymbol{r}; \alpha, R) \Rightarrow D_{(c,c)}(\boldsymbol{r}) = \mathcal{L}(\boldsymbol{r}; \alpha, 2^{1/\alpha} R) \tag{3.29}$$

An illustration of the shape of such distributions can be seen in Fig. 3.3. The average momentum dependence appears through the two parameters of $D_{(c,c)}(\boldsymbol{r})$:

$$D_{(c,c)}(\boldsymbol{r}, \boldsymbol{K}) = \mathcal{L}(\boldsymbol{r}; \alpha(\boldsymbol{K}), 2^{1/\alpha(\boldsymbol{K})} R(\boldsymbol{K})). \tag{3.30}$$

The dependence of the Lévy source parameters on the pair average momentum K is non-trivial and is often the subject of experimental investigations.

Besides a better description of the shape of the source function, another primary motivation of Lévy HBT measurements in heavy-ion collisions is the search for the critical endpoint on the QCD phase diagram. It can be shown that the Lévy-exponent α (describing the power-law tail of the distribution) is connected to the η critical exponent known from statistical physics [147]. The η exponent describes the power-law behavior of the spatial correlations at the critical point in case of a second-order phase transition:

Of course, the picture is more complex than this simple equivalence; finite-size effects and dynamical critical behavior may also play an important role [151, 152].

$$\langle \phi(r)\phi(0) \rangle \propto r^{-1-\eta}, \tag{3.31}$$

where ϕ is the order parameter. Comparing this to equation 3.28 suggests that at the critical point, the α Lévy exponent might be identical to η. It is expected that a possible second-order phase transition of

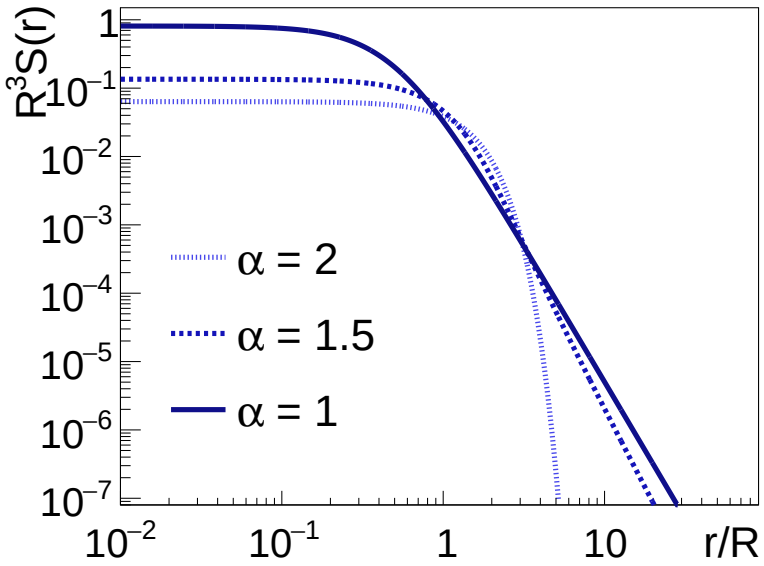

Figure 3.3: Lévy-stable source distributions with $S(r) = \mathcal{L}(|r|; \alpha, R)$ for α = 2, 1.5, and 1. The dependence on R is scaled out.

QCD falls into the same universality class as the 3D Ising model [153, 154], where the expected value of this exponent is η=0.03631(3) [155] (or in case of random external fields, η=0.5±0.05 [156]). One of the main goals of Lévy femtoscopy is to measure the values of the α Lévy exponent as a function of center-of-mass collision energy and use these measurements as a tool in the exploration of the QCD phase diagram.

3.3 EXPERIMENTAL METHODS OF FEMTOSCOPY

Although each high-energy detector system is unique on its own, there are general aspects of correlation measurement techniques that can be utilized in any experiment. In this section, I review some of these methods, while the experiment-specific details will be presented in Chapters 4 and 5.

3.3.1 *Kinematic variables of the correlation function*

One of the most important first steps of an experimental analysis is to determine the nature and dimensionality of the correlation function and find the best variable to use for the measurements, as it can be fundamentally different depending on the underlying physical processes. Usually, as I discussed before, the correlation function

depends on the p_1 and p_2 four-momenta, or in other notation the q and K relative- and average momentum variables. It is known, that the Lorentz product of $q = (q_0, \boldsymbol{q})$ and $K = (K_0, \boldsymbol{K})$ is zero, i.e. $qK = q_0 K_0 - \boldsymbol{qK} = 0$, where $\boldsymbol{q} \equiv (q_x, q_y, q_z)$ and $\boldsymbol{K} \equiv (K_x, K_y, K_z)$. This means that the energy component of q can be expressed as

$$q_0 = \boldsymbol{q}\frac{\boldsymbol{K}}{K_0}. \tag{3.32}$$

Based on this relation, one may transform the q dependent correlation function to depend on the three-momentum component $\boldsymbol{q}$ only. Furthermore, if the energy of the particles contributing to the correlation function are similar, then K is approximately on shell, so the correlation function can be measured as a function of the three-momentum variables $\boldsymbol{q}$ and $\boldsymbol{K}$.

As the $\boldsymbol{K}$ dependence is usually more smooth than the dependence on $\boldsymbol{q}$, the latter can be considered the main kinematic variable. The usual method for the experimental investigation is to measure the correlation function in different $\boldsymbol{K}$ average pair momentum bins and assume a parametrization for the shape in the $\boldsymbol{q}$ relative momentum variable ($C_2(\boldsymbol{q})$). This parametrization can then be tested via fits to the measured correlation functions, the source parameters can be extracted, and their average transverse momentum dependence can be investigated. Close to mid-rapidity, instead of $\boldsymbol{K}$ one can investigate the average transverse momentum $k_T \equiv 0.5\sqrt{K_x^2 + K_y^2}$ dependence, or alternatively the average transverse mass $m_T = \sqrt{m^2 + (k_T/c)^2}$ dependence, where m is the mass of the given particle type (e.g. pion).

For any fixed value of the pair average-transverse mass, the correlation function $C_2(\boldsymbol{q}, m_T)$ can be thus measured as a function of the relative momentum $\boldsymbol{q}$ only. An often used decomposition is the out-side-long or Bertsch-Pratt (BP) coordinate-system [157, 158], where $\boldsymbol{q} \equiv (q_{out}, q_{side}, q_{long})$. In this case, the 'long' direction is identical to the beam- or z-direction, 'out' is the direction of the pair average transverse momentum k_T, and 'side' is orthogonal to the previous two. Changing to the BP frame is essentially a rotation in the transverse plane. It is customary, furthermore, to use a Lorentz-boost in the long direction and change to the Longitudinal Co-Moving System (LCMS) where the average longitudinal momentum of the pair is zero [127, 128].

Usually, a drawback of a three-dimensional measurement as a function of the $q_{out}, q_{side}, q_{long}$ variables is the lack of statistics and thus the difficulties of a precise shape-analysis. To overcome these issues, one often measures the two-particle correlation functions as a function of a one-dimensional relative momentum variable. The definition of the Lorentz-invariant relative momentum is the following:

$$q_{inv} \equiv \sqrt{-q^{\mu}q_{\mu}} = \sqrt{q_x^2 + q_y^2 + q_z^2 - (E_1 - E_2)^2}. \tag{3.33}$$

It is easy to see that this is equivalent to the three-momentum difference in the Pair Co-Moving System (PCMS), where $E_1 = E_2$:

$$q_{inv} = |\boldsymbol{q}_{PCMS}|. \tag{3.34}$$

In the LCMS system, using the BP variables, q_{inv} can be written as

$$q_{inv} = \sqrt{(1-\beta_T)^2 q_{out}^2 + q_{side}^2 + q_{long}^2}, \tag{3.35}$$

where $\beta_T = 2k_T/(E_1 + E_2)$ is the 'average transverse speed' of the pair. This form also shows that $q_{inv} \to 0$ does not necessarily mean that the components tend to zero as well, i.e. $q_{out} \to 0$, $q_{side} \to 0$, $q_{long} \to 0$ is not necessarily true simultaneously. The value of q_{inv} can be small even when q_{out} is relatively large. This also means that the $q \to 0$ extrapolation (detailed in section 3.2.2) is not independent of the choice of variable.

It is known that the Bertsch-Pratt-radii (R_{out},R_{side},R_{long}) are of similar magnitude in case of $\sqrt{s_{NN}} = 200$ GeV Au+Au collisions at RHIC, i.e. the Bose-Einstein correlations are nearly spherically symmetric in the LCMS [121, 122, 159, 160]. However, the correlation function boosted to PCMS will not be spherically symmetric, especially for higher k_T values where β_T is close to 1. Based on this, in case of 200 GeV Au+Au collisions, q_{inv} is not the right variable to use for one-dimensional pion correlation measurements.

Let us look for a one-dimensional variable, which can only take small values when the values of the out-side-long components are also small. Let us introduce the following variable invariant to Lorentz-boosts in the beam direction:

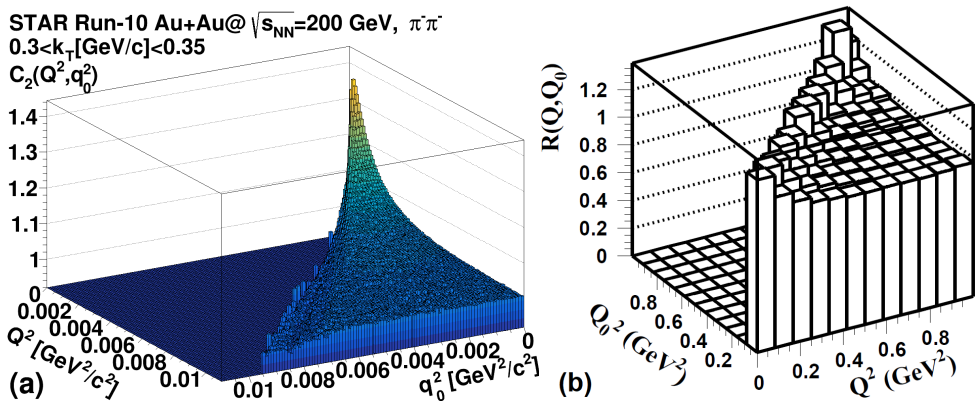

Figure 3.4: Example two-dimensional pion correlation functions for $\sqrt{s_{NN}} = 200$ GeV Au+Au collisions (a) and $\sqrt{s} = 91$ GeV e^+e^- collisions (b). The latter figure is taken from the thesis of Tamás Novák [161].

$$Q \equiv |\boldsymbol{q}_{LCMS}| = \sqrt{(p_{1x} - p_{2x})^2 + (p_{1y} - p_{2y})^2 + q_{z,LCMS}^2}, \quad (3.36)$$

$$\text{where } q_{z,LCMS}^2 = \frac{4(p_{1z}E_2 - p_{2z}E_1)^2}{(E_1 + E_2)^2 - (p_{1z} + p_{2z})^2}. \quad (3.37)$$

Since the correlation functions in the LCMS are nearly spherically symmetric, the measured correlation function does not depend strongly on the direction of $\boldsymbol{q}_{LCMS}$, hence its magnitude is a good choice of variable.

In experiments one can investigate the nature of the one-dimensional variable by looking at the correlation function in two dimensions, as a function of $q_0 = E_1 - E_2$ and $|\boldsymbol{q}|$. In case of a q_{inv} dependent correlation function, a maximum can be expected along the diagonal. An example where this turned out to be true is an analysis of pion correlation functions in electron-positron collisions [161], as shown on Figure 3.4 (b). In case of the analyses presented in Chapters 4 and 5, however, no maximum along the diagonal has been observed (as shown in Figure 3.4 (a)); hence Q was used as the one-dimensional variable of choice.

Finally, let me show the result of two simple toy model calculations with two radically different source-function types that can lead to q_{inv} or Q dependent correlation functions [162]. First, let us take a Gaussian source in both space and time coordinates:

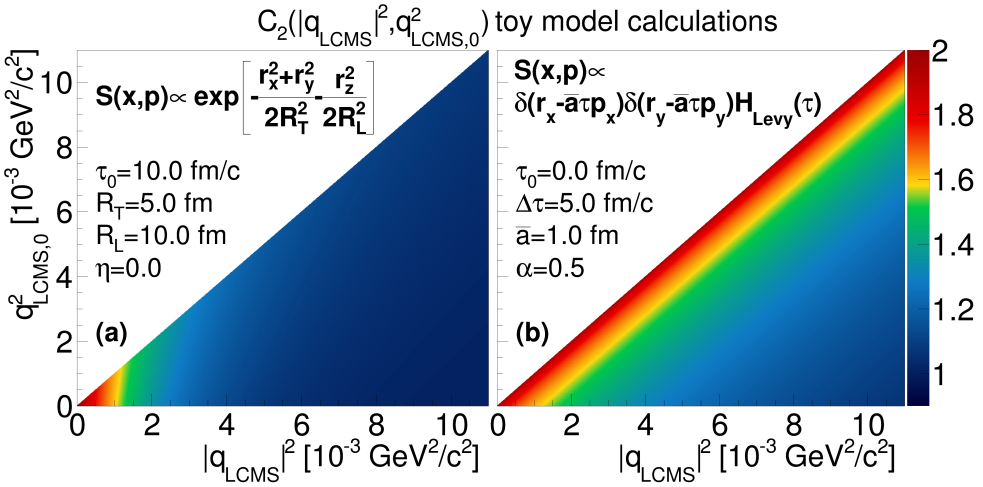

Figure 3.5: Toy model calculation for two different types of source functions. Taking a Gaussian source in both space and time leads to a correlation function that depends mostly on $|q_{LCMS}|$ (a), while a source that shows strong space-time and momentum space correlation leads to a q_{inv} dependent correlation function (b).

$$S(x,p) \propto \exp\left[-\frac{r_x^2+r_y^2}{2R_T^2} - \frac{r_z^2}{2R_L^2} - \frac{(\tau-\tau_0)^2}{2\Delta\tau^2}\right]. \tag{3.38}$$

With this, the correlation function (calculated based on equation 3.15) will also be Gaussian in both the transverse (q_T) and longitudinal (q_L) directions, and the widths will depend on the time-like component (q_0) as well. This correlation function barely depends on q_0; its values are determined mainly by the magnitude of the relative three-momentum, as shown in Figure 3.5 (a). Let us take next a source function that shows a strong momentum-space - coordinate-space correlation, i.e., in spatial coordinates the emission is a Dirac-delta, characterized by a maximal emission point proportional to momentum, and in proper time the emission distribution is characterized by a one-sided Lévy distribution:

$$S(x,p) \propto \delta(r_x - \bar{a}\tau p_x)\delta(r_y - \bar{a}\tau p_y)H_{\text{Lévy}}(\tau). \tag{3.39}$$

These types of source functions are investigated within the framework of the τ-model detailed in Refs. [163, 164]. The correlation function in this case depend solely on q_{inv} as shown on Figure 3.5 (b).

3.3.2 *The event mixing method*

The method of the experimental reconstruction of the correlation function is called event-mixing. First, one has to take pairs of particles (e.g., identical pions) created in the same event, then measure the relative momentum distribution of these pairs – this is called the actual distribution, denoted by $A(Q)$. This distribution contains effects stemming from kinematics and detector acceptance, which must be excluded. One can then create a distribution where the pair members are from separate events – this is called the background distribution, denoted by $B(Q)$. Taking the normalized ratio of these two distributions, the correlation function can be constructed:

$$C_2(Q) = \frac{A(Q)}{B(Q)} \cdot \frac{\int_{Q_1}^{Q_2} B(Q)dQ}{\int_{Q_1}^{Q_2} A(Q)dQ}, \tag{3.40}$$

where the integral is calculated at a $[Q_1, Q_2]$ range where the correlation function does not exhibit quantum-statistical effects. It is vital that during the mixing, the actual and background distribution must contain similar acceptance and kinematic effects – to achieve this, actual and background events must have similar centrality and collision vertex positions.

The technical execution of the event mixing is not straightforward. The traditional way is to keep a background event pool with a predefined size (N_{pool}) and correlate all pions of the actual event with all same-charge pions from the background pool. In this case, residual kinematic or detector effects may remain, stemming from using multiple pions from a given background event. A more "careful" way to proceed is to randomly choose a number of events (matching the actual event multiplicity) from the background pool. From each selected event, randomly select one pion. This way, the number of chosen background pions is the same as the number of pions in the actual event, and all of these background pions are from different events. The background distribution is then created by correlating these randomly chosen pions with each other. Of course, in this case, it is essential to have a greater number of events in the pool than the maximum possible event multiplicity. An illustration of this event mixing method can be seen in Figure 3.6.

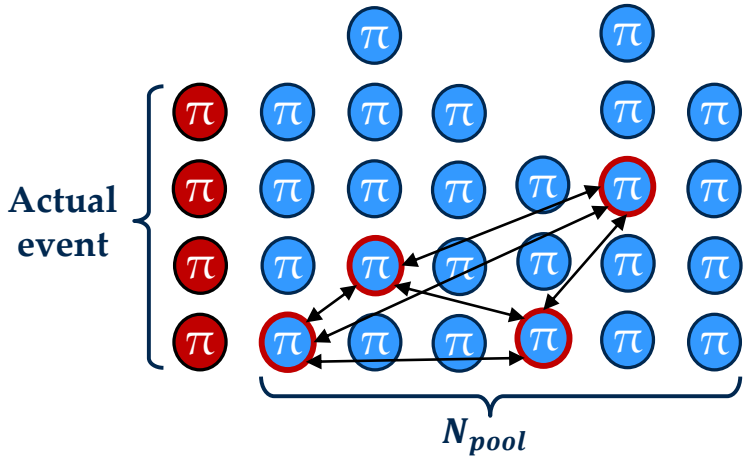

Figure 3.6: Illustration of the event mixing method. In this example, the maximum event multiplicity is 5, and the size of the background pool is $N_{pool} = 6$. To match the actual event multiplicity, 4 events are chosen randomly from the pool, and one pion is chosen randomly from each of these events. These pions are then correlated with each other to form the background distribution.

3.3.3 *Coulomb correction and fitting of the correlation function*

After the rigorous event, track, and pair selection, the next step in an experimental analysis is to fit the measured correlation functions. First, one has to make an assumption on the shape of the source function, and coupling this assumption with a proper treatment of final-state interactions, one has to calculate the shape of the correlation function. This shape can then be tested on the experimental data. If a good description is found, the source parameters can be extracted and analyzed as a function of, e.g., average transverse momentum or centrality.

Let us combine the conclusions of section 3.3.1 with equation 3.23:

$$C_2(Q, k_T) = 1 - \lambda + \lambda \int d^3\boldsymbol{r} D_{(c,c)}(\boldsymbol{r}, k_T) \left|\Psi_Q^{(2)}(\boldsymbol{r})\right|^2. \tag{3.41}$$

Neglecting final-state effects and using a Lévy-stable source function (discussed in section 3.2.3), this becomes

$$C_2^{(0)}(Q, k_T) = 1 + \lambda e^{-|RQ|^\alpha}. \tag{3.42}$$

Details about the calculation of the integral in equation 3.41 for Lévy-type sources are discussed in chapter 6. To accelerate the fit-

ting process, a database can be created, storing the numerically pre-calculated shape of the correlation function for various source parameter (α, R) values. This database can then be used to quickly calculate the shape for any set of parameters, iterating between the pre-calculated values. This way, however, using equation 3.41 as a fit function often results in a numerically fluctuating χ^2 landscape, which makes it difficult to find the correct minimum. To get around this problem, it is customary to detach the part containing the final-state interactions and treat it as a correction factor:

$$K(Q, k_T) = \frac{C_2(Q, k_T)}{C_2^{(0)}(Q, k_T)}. \tag{3.43}$$

Dividing the measured correlation function with this leads to a purely quantum-statistical correlation function (without final-state effects) which can be fitted with the analytically expressible $C_2^{(0)}$ function. Since the correction factor also depends on the source parameters, an iterative method can be used where the fit function is defined as

Here I omit the k_T dependence; as it was mentioned before, it appears through the source parameters λ, R, α.

$$C_2^{(fit)}(Q; \lambda, R, \alpha) = C_2^{(0)}(Q; \lambda, R, \alpha) \cdot K(Q; \lambda_0, R_0, \alpha_0). \tag{3.44}$$

Here λ_0, R_0, α_0 are the initial parameter values used to calculate the correction factor, and λ, R, α are the fit parameters. Let us denote the resulting fit parameters with λ_1, R_1, α_1. If the difference compared to the λ_0, R_0, α_0 parameters is significant, these are set as the input for the correction factor, and another round of fitting is done $(\lambda_0 = \lambda_1, R_0 = R_1, \alpha_0 = \alpha_1)$. This iterative procedure is continued until the $\Delta_{iteration}$ difference calculated from the new parameters and the parameters from the previous round is small enough, e.g., less than 1%:

$$\Delta_{\text{iteration}} = \sqrt{\frac{(\lambda_{n+1} - \lambda_n)^2}{\lambda_n^2} + \frac{(R_{n+1} - R_n)^2}{R_n^2} + \frac{(\alpha_{n+1} - \alpha_n)^2}{\alpha_n^2}} < 0.01. \tag{3.45}$$

These types of iterations usually converge within 2-3 rounds. With this method, the physical fit parameters can be reliably extracted from the experimental data with a proper treatment of final-state interactions.

Another important complication that needs to be mentioned is the difference between frames. The calculation of the Coulomb-correction detailed in Chapter 6 is done in the PCMS frame, and the transformation to LCMS is not straightforward [165]. A possible solution in case of one-dimensional measurements is to use a weighted average for the Coulomb correction:

$$K_{weighted}(Q) = \frac{\int A(Q, q_{inv}) K(q_{inv}) dq_{inv}}{\int A(Q, q_{inv}) dq_{inv}}, \tag{3.46}$$

where $A(Q, q_{inv})$ is the actual distribution of particle pairs measured in two dimensions, using both variables. This approach can be further improved by substituting R_{PCMS} into the Coulomb correction [165], defined as

$$R_{PCMS} = \sqrt{\frac{1 - \frac{2}{3}\beta_T^2}{1 - \beta_T^2}} R, \text{ where } \beta_T = \frac{k_T}{m_T}. \tag{3.47}$$

This way the fit function (omitting the λ, α dependence) becomes:

$$C_2^{(fit)}(Q; R) = C_2^{(0)}(Q; R) \cdot K_{weighted}(Q; R_{PCMS}). \tag{3.48}$$

This is a sound approach, however, in reality the fitting process can become quite slow due to the calculation of these weighted averages. When one tries to investigate detailed k_T, and centrality dependence, not to mention systematic uncertainty investigations where these fits have to be done for countless settings of different track and pair selections, this type of fitting process can become extremely time-consuming. Another approach that is easier to implement is to make an appropriate approximation of the $Q - q_{inv}$ relation (in case of $q_{out} = q_{side} = q_{long}$) [165]. This way the fit function becomes

$$C_2^{(fit)}(Q; R) = C_2^{(0)}(Q; R) \cdot K\left(Q\sqrt{1 - \beta_T^2/3}; R_{PCMS}\right). \tag{3.49}$$

The R_{PCMS}/R_{LCMS} and q_{inv}/Q approximations as a function of the average transverse mass m_T are shown on Figure 3.7.

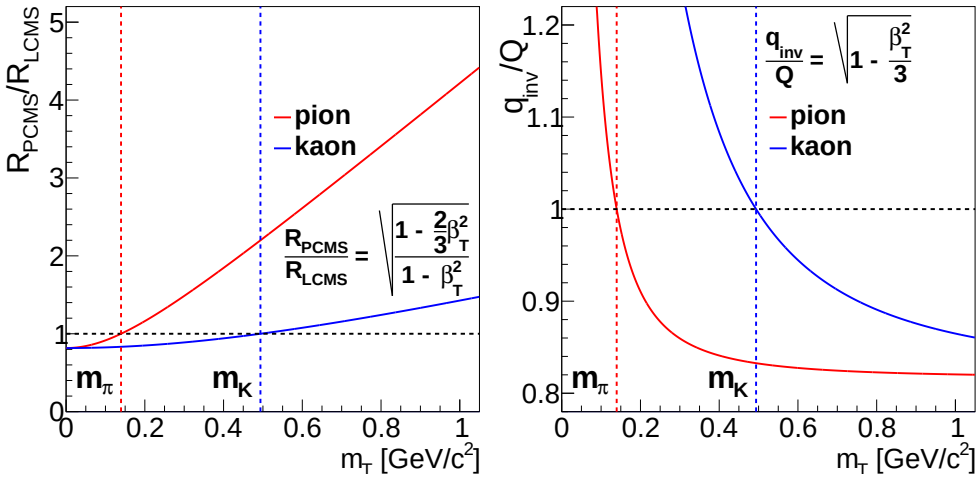

Figure 3.7: Approximate translation between the PCMS and LCMS frames for the scale parameter and the relative momentum variables as a function of average transverse mass m_T. The red and blue vertical dashed lines correspond to the pion and kaon mass, respectively.

Part II

EXPERIMENTAL MEASUREMENTS

It does not make any difference how beautiful your guess is. It does not make any difference how smart you are, who made the guess, or what his name is — if it disagrees with experiment it is wrong.

— Richard P. Feynman [166]

4

LÉVY-HBT ANALYSIS AT PHENIX

In this chapter, I present a data analysis that I started to develop before enrolling in the Ph.D. program. Although the PHENIX publication [9] discussed in Section 4.2 that provides the basis for this chapter was published during my Ph.D. studies, it is not officially part of the thesis points since it was a joint effort with Máté Csanád and Sándor Lökös, both of whom used the paper for their respective D.Sc. and Ph.D. dissertations. A follow-up analysis, however, published in Ref. [1] and presented in Section 4.3, represents an essential part of the thesis points of the dissertation. These experimental analyses aim to explore the shape of the two-pion source function in heavy-ion collisions in more detail than it was done before. It seems that utilizing a Lévy distribution as a source function can provide a good description, and investigation of the Lévy source parameters may shed light on previously unexplored properties of the Quark-Gluon-Plasma and the phase-diagram of QCD.

4.1 DETAILS OF THE ANALYSIS

In this section, I present the details of an analysis I conducted on data of Au+Au collisions recorded by the PHENIX experiment. Although the analysis of the $\sqrt{s_{NN}} = 200$ GeV data can be considered a separate one from the beam-energy scan investigation done on the $\sqrt{s_{NN}} = 62.4, 39.0, 27.0, 19.6, 14.6$ GeV datasets, much of the technical details are the same, so in this section these are discussed in parallel. The goal of these analyses is to investigate quantum-statistical correlations of pion pairs and gain information about the pion pair source distribution.

4.1.1 *Single track cuts, particle identification*

In PHENIX, the tracks (and thus the momentum) of the particles are reconstructed by the DC and PC detectors. The reconstructed tracks are then projected onto the outer detector layers (PbSc, TOF, PC3). The

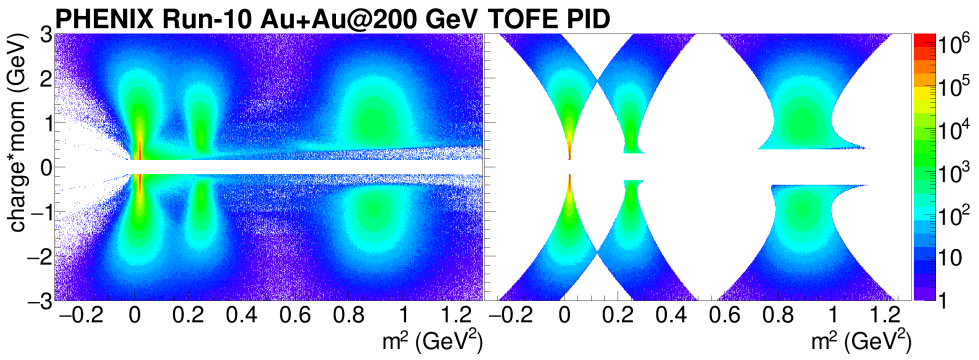

Figure 4.1: Particle identification with PHENIX-TOF detectors, using a 2σ cut. On the distribution of the momentum-charge product vs. mass-square the pion-kaon-proton hits are well separated.

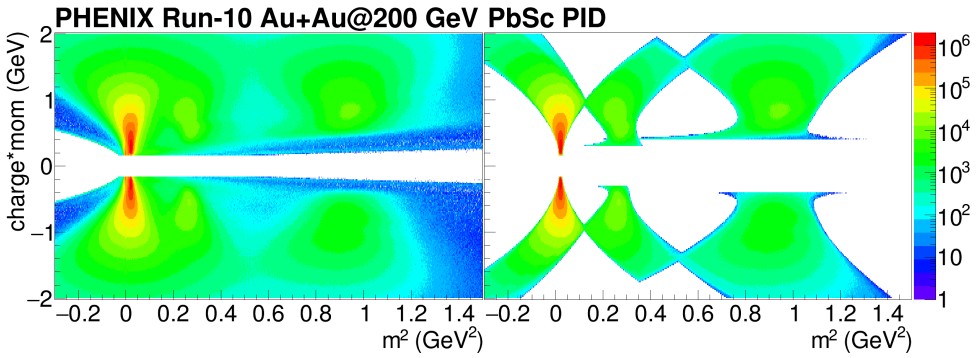

Figure 4.2: Particle identification with PHENIX-PbSc detectors, using a 2σ cut. On the distribution of the momentum-charge product vs. mass-square the pion-kaon-proton hits are not as well separated as for TOF, because of the different time resolution of the detectors.

difference between the projection coordinates and the closest actual hit is calculated in both the z and the φ directions, and a matching cut is applied to this variable. The effect of this cut is taken into account later in the systematic uncertainty calculations.

The used pion sample must be devoid of contamination from other types of particles – for this, a strict and effective particle identification is needed. The method was discussed in Chapter 2.1.3, and a few example plots are shown below in Figures 4.1, 4.2. During the systematic uncertainty calculations, I investigated the stability of the results for different values of the used Particle Identification (PID) cut.

4.1.2 *Measurement of the correlation functions*

The reconstruction of the correlation functions were done with the event-mixing method described in section 3.3.2. In my analysis, I used

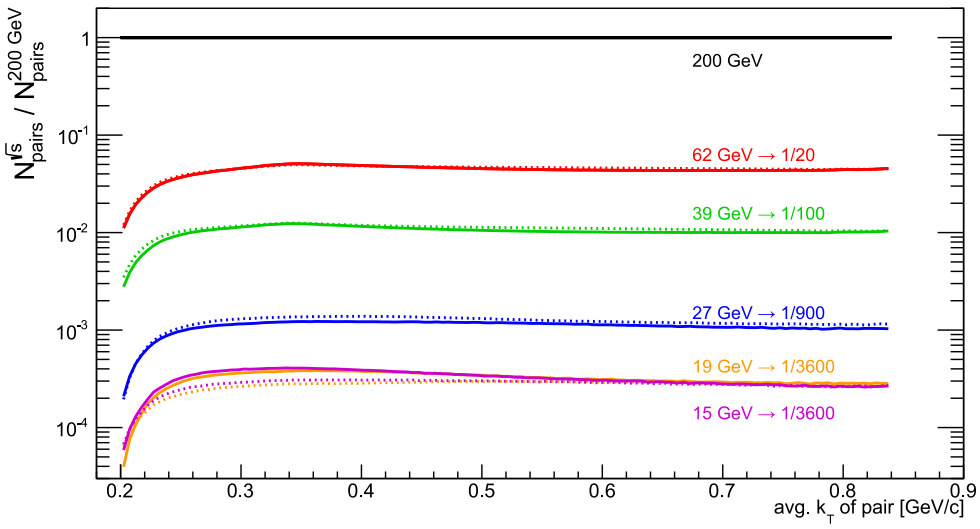

Figure 4.3: Number of pion pairs as a function of average transverse momentum, compared to the 200 GeV data. The $\pi^+\pi^+$ pairs are denoted with a dashed line, while the $\pi^-\pi^-$ pairs are denoted with a continuous line.

3% wide centrality (9% in case of lower energies) and 2 cm wide z-vertex bins and mixed only those actual and background events that fell into the same event class.

When moving on to the lower collision energies, it becomes increasingly difficult to do precise measurements because of the difference in the amount of data. In order to increase precision by improving on the low statistics of these data sets, I had to come up with new ideas. First, to compare the statistics of the 200 GeV data to the lower collision energies, I created a histogram of the number of pion pairs. For a given relative momentum range (0.02 GeV $< Q <$ 0.15 GeV) encompassing the Bose-Einstein peak, I plotted the number of pairs as a function of the average transverse momentum ($dN/dk_T(k_T)$). For each lower energy data set, I divided this with the 200 GeV histogram – this is shown in Figure 4.3. The ratio for 62 GeV is about 1/20, for 39 GeV about 1/100, for 27 GeV about 1/900, while for 19 GeV and 15 GeV, it is about 1/3600.

I found three methods to increase statistics, two of which are connected to the event-mixing. In the case of the event-mixing method illustrated in Figure 3.6., the size of the background event is identical to the size of the actual event. However, increasing the number of generated background events can decrease the statistical uncertainties on the bins of the background histogram. The statistical uncertainties on the points of the correlation function then can be reduced by a

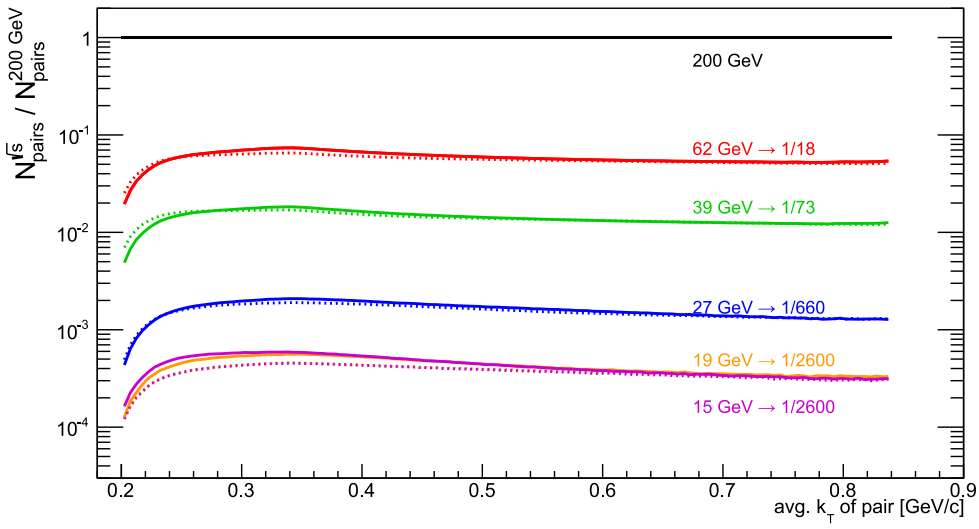

Figure 4.4: Number of pion pairs as a function of average transverse momentum, compared to the 200 GeV data, including PbSc-TOF mixed pairs. The $\pi^+\pi^+$ pairs are denoted with a dashed line, while the $\pi^-\pi^-$ pairs are denoted with a continuous line.

factor of $\sqrt{2}$. During the analysis, I thoroughly investigated what happens to the correlation function when increasing the number of generated background events. I found that it indeed decreases the statistical uncertainties, and the values change within errors. I chose the number of generated background events for the lower energy analyses to be 5.

It is important to note that the previous method does not decrease the statistical uncertainties by increasing the number of pairs. There is a way, however, to gain more pairs as well. As I have shown before, there are four detectors used for particle identification – a PbSc and a TOF detector in each arm. In the case of the 200 GeV analysis, pairs were only mixed within a given detector used for identification. The number of pairs can be increased if we use mixed pairs, where in a given arm, one member of the pair is from PbSc, and the other is from TOF. For the lower energy analyses, I included these mixed pairs as well – the increase in the number of pairs can be seen in Figure 4.4.

4.1.3 *Pair cuts*

When forming pairs to construct the previously mentioned $A(Q)$ and $B(Q)$ distributions, one has to consider the efficiency of the various detectors and the peculiarities of the track reconstruction algorithm.

Sometimes, the algorithm splits a track into two and creates a "ghost" particle next to a real one. It can also happen that two real tracks cannot be separated if they are too close to each other – in this case, the algorithm merges the two and reconstruct them as one. To correct for these effects, I measured the spatial separation distributions as a function of azimuth angle and beam direction coordinate difference $(\Delta\varphi, \Delta z)$ for the actual and background events separately. Using these, I created a correlation function defined as

$$C(\Delta\varphi, \Delta z) = \frac{A(\Delta\varphi, \Delta z)}{B(\Delta\varphi, \Delta z)} \cdot \frac{\int_{\Delta\varphi_1}^{\Delta\varphi_2} \int_{\Delta z_1}^{\Delta z_2} B(\Delta\varphi, \Delta z)}{\int_{\Delta\varphi_1}^{\Delta\varphi_2} \int_{\Delta z_1}^{\Delta z_2} A(\Delta\varphi, \Delta z)}, \tag{4.50}$$

where $[\Delta\varphi_1, \Delta\varphi_2]$ and $[\Delta z_1, \Delta z_2]$ is a range where the splitting and merging effects are not relevant. On these correlation histograms the splitting and merging effects show up as peaks and valleys – these regions, where the distribution is not uniform, can be cut out in order to get rid of these "false" pairs. The cuts I have defined in the $\Delta\varphi - \Delta z$ variables are the following:

$$\text{TOF-E: } \Delta\varphi > \Delta\varphi_0 - \frac{\Delta\varphi_0}{\Delta z_0}\Delta z \tag{4.51}$$

$$\text{TOF-W: } \Delta\varphi > \Delta\varphi_0 \text{ and } \Delta z > \Delta z_0 \tag{4.52}$$

$$\text{DC/PbSc (200 GeV): } \Delta\varphi > \Delta\varphi_0 - \frac{\Delta\varphi_0}{\Delta z_0}\Delta z \text{ and } \Delta\varphi > \Delta\varphi_1 \tag{4.53}$$

$$\text{DC (62-15 GeV): } \Delta\varphi > \Delta\varphi_0 \text{ or } (\Delta\varphi > \Delta\varphi_1 \text{ and } \Delta z > \Delta z_1) \text{ or } \Delta z > \Delta z_0 \tag{4.54}$$

$$\text{PbSc (62-15 GeV): } \Delta\varphi > \Delta\varphi_0 \text{ and } \Delta z > \Delta z_0. \tag{4.55}$$

The parameters of the cuts are listed in Tables 4.1-4.2. An example for the $\Delta\varphi - \Delta z$ correlation histograms can be seen in Figures 4.5-4.7. For the final results, I used cut 0; the rest was used for the systematic uncertainty calculations. Another customary pair cut I applied is randomly throwing out one member of the pair if both arrived in the same segment within a given detector.

200 GeV						
cut	TOF-E			TOF-W		
	Δz_0 [cm]	$\Delta\varphi_0$ [rad]		Δz_0 [cm]	$\Delta\varphi_0$ [rad]	
0	13	0.13		15.0	0.085	
1	13	0.13		15.0	0.085	
2	13	0.13		15.0	0.085	
3	12	0.12		14.5	0.080	
4	14	0.14		15.5	0.090	
cut	DC			PbSc		
	Δz_0 [cm]	$\Delta\varphi_0$ [rad]	$\Delta\varphi_1$ [rad]	Δz_0 [cm]	$\Delta\varphi_0$ [rad]	$\Delta\varphi_1$ [rad]
0	11	0.15	0.025	18	0.14	0.020
1	10	0.14	0.020	18	0.14	0.020
2	12	0.16	0.030	18	0.14	0.020
3	11	0.15	0.025	17	0.13	0.015
4	11	0.15	0.025	19	0.15	0.025

Table 4.1: Parameters of the 200 GeV pair cuts to be substituted to Equations (4.51)-(4.53).

62-15 GeV						
cut	TOF-E		TOF-W		PbSc	
	Δz_0 [cm]	$\Delta\varphi_0$ [rad]	Δz_0 [cm]	$\Delta\varphi_0$ [rad]	Δz_0 [cm]	$\Delta\varphi_0$ [rad]
0	15	0.14	15	0.085	20	0.06
1	15	0.14	15	0.085	20	0.06
2	15	0.14	15	0.085	20	0.06
3	14	0.13	14	0.080	19	0.05
4	17	0.16	16	0.090	21	0.09
cut	DC					
	Δz_0 [cm]	$\Delta\varphi_0$ [rad]	Δz_1 [cm]	$\Delta\varphi_1$ [rad]		
0	80	0.14	8.0	0.025		
1	75	0.13	7.5	0.020		
2	85	0.15	8.5	0.030		
3	80	0.14	8.0	0.025		
4	80	0.14	8.0	0.025		

Table 4.2: Parameters of the lower energy pair cuts to be substituted to Equations (4.51)-(4.52) and (4.54)-(4.55).

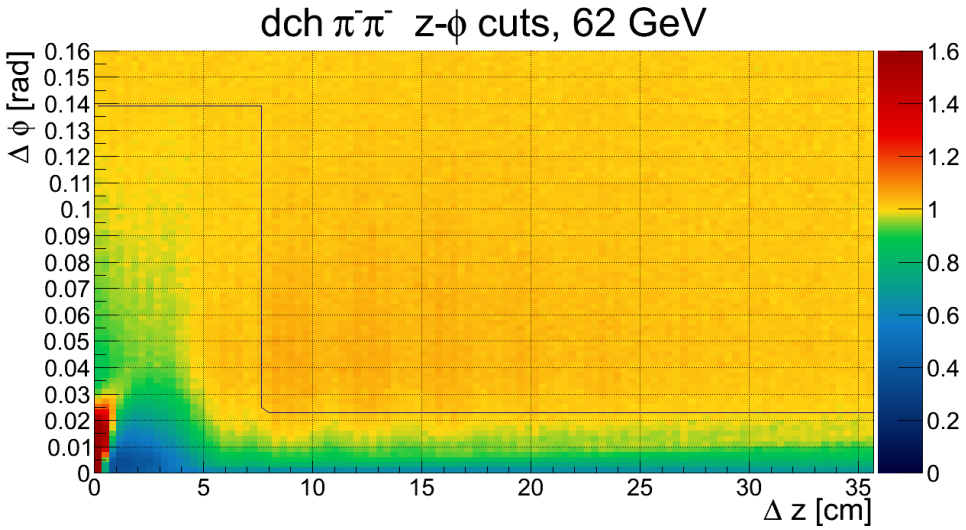

Figure 4.5: $C(\Delta\varphi, \Delta z)$ correlations measured by the DC detector, and the defined pair cuts for $\sqrt{s_{NN}} = 62$ GeV Au+Au collisions.

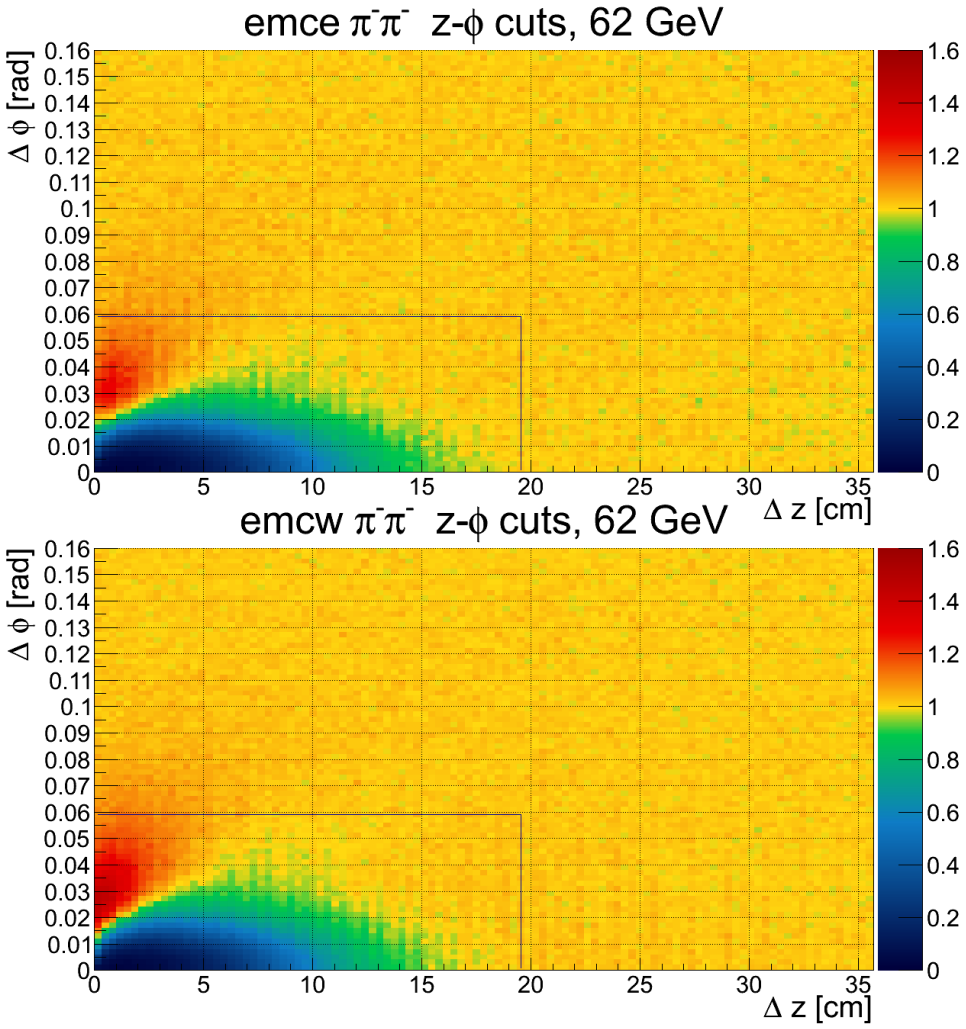

Figure 4.6: $C(\Delta\varphi, \Delta z)$ correlations measured by the PbSc-E and PbSc-W detectors, and the defined pair cuts for $\sqrt{s_{NN}} = 62$ GeV Au+Au collisions.

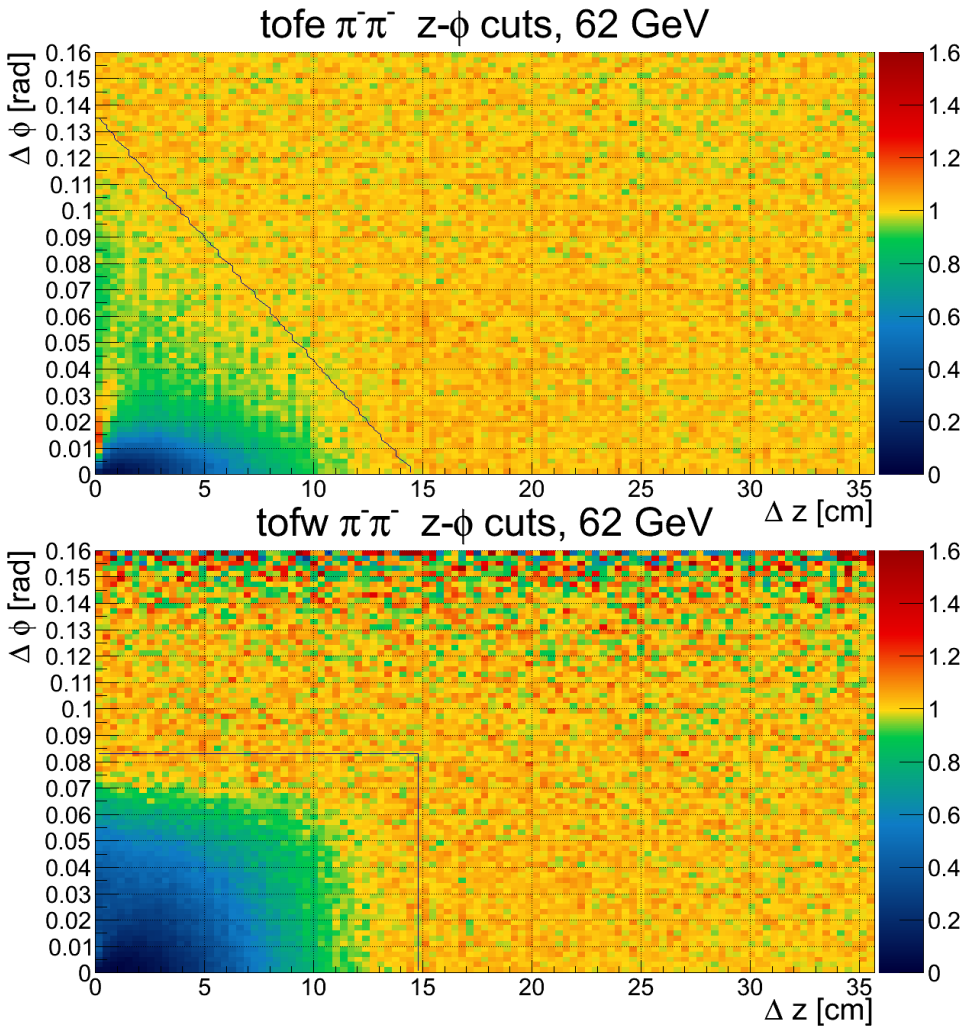

Figure 4.7: $C(\Delta\varphi, \Delta z)$ correlations measured by the TOF-E and TOF-W detectors, and the defined pair cuts for $\sqrt{s_{NN}} = 62$ GeV Au+Au collisions.

4.1.4 *Fitting of the correlation functions*

The fitting process was done with the help of the ROOT MINUIT2 χ^2 minimization libraries [167], following along the lines of section 3.3.3. The shape of the correlation function was numerically pre-calculated, and these values were used as an input for the $K(Q)$ Coulomb-correction. An iterative process was also applied where the fit function contained only analytic dependencies on the fit parameters. The fit function was the following:

$$C_2^{(fit)}(Q;\lambda,R,\alpha)=C_2^{(0)}(Q;\lambda,R,\alpha)K(Q;\lambda_0,R_0,\alpha_0)\times N(1+\varepsilon Q), \tag{4.56}$$

where $C_2^{(0)}$ and $K(Q)$ are defined in equations 3.42 and 3.43, and λ_0, R_0, α_0 are the previous-round fit parameters. The iterative process was done as described in section 3.3.3. Normalization parameters N and ε were introduced to describe a possible long-range background. Their values almost always turned out to be $N \approx 1$ and $\varepsilon \approx 0$, so they were not used in the convergence criteria. A fit was accepted only if a valid minimum was reached, the error matrix was positive definite, and the χ^2/NDF values corresponded to a confidence level greater than 0.1%. An example of such fits is shown in Figure 4.8.

4.1.5 *Systematic uncertainties*

The parameter values extracted from fits to the measured correlation functions depend on several experimental variables like single-track and pair cuts, fit limits, and different settings of the fitting algorithm. During the systematic uncertainty investigations I identified seven important sources. Let us denote the the given fit parameter with P ($P = R, \lambda, \alpha$), and the given average transverse momentum bin with i ($i \in [0, 31]$). With the default cut settings the value of the parameter is $P^0(i)$. Let us denote furthermore the different sources of systematic uncertainties with n, and the different settings of the given source with j. The different settings of the systematic uncertainty sources are summarized in Table 4.3. The asymmetric systematic uncertainty of the given parameter in the given average transverse momentum bin then can be calculated as

$$\delta P^{\uparrow}(i) = \sqrt{\sum_n \frac{1}{N_n^{j\uparrow}} \sum_{j \in J_n^{\uparrow}} (P_n^j(i) - P^0(i))^2} \tag{4.57}$$

$$\delta P^{\downarrow}(i) = \sqrt{\sum_n \frac{1}{N_n^{j\downarrow}} \sum_{j \in J_n^{\downarrow}} (P_n^j(i) - P^0(i))^2}, \tag{4.58}$$

where the $J_n^{\uparrow}$ is the set of j values where $P_n^j(i) > P^0(i)$, and $N_n^{j\uparrow}$ is the cardinality of this set. The latter can assume zero value as well if all settings decrease the parameter (compared to the default setting). Similarly, $J_n^{\downarrow}$ is the set of j values where $P_n^j(i) < P^0(i)$, and $N_n^{j\downarrow}$ is the cardinality of this set. The sum on j in the above definition is only done if the cardinality of the given set is not zero. To smooth out non-

n	source of uncertainty	settings ($j = 0, 1, \ldots$)
0	PID in east/west arm	both, east, west
1	Lower limit of the fit in Q	3 different limits
2	Upper limit of the fit in Q	7 different limits
3	PID cut	$2\sigma, 1.5\sigma, 2.5\sigma$
4	Matching cut in the PID detectors	$2\sigma, 1.5\sigma, 2.5\sigma$
5	Matching cut in PC3 detector	$\infty\sigma, 1.5\sigma, 2.5\sigma$
6	Pair cut in the PID detectors	3 settings (Tables 4.1-4.2)
7	Pair cut in the DC detector	3 settings (Tables 4.1-4.2.)
8	Coulomb effect	2 settings

Table 4.3: Different settings of the sources of systematic uncertainties

physical fluctuations, a 5 point weighted average is also applied on the different average transverse momentum bins. I investigated further possible sources of systematic uncertainties as well (e.g. changing the number of bins in Q, and in m_T), and found their effect to be negligible. The last setting listed in Table 4.3 refers to using Equation 3.48 instead of Equation 4.56 as a fit function. The detailed values of the systematic uncertainties corresponding to the different settings can be found in Ref. [9].

4.2 RESULTS FOR $\sqrt{s_{NN}} = 200$ GEV AU+AU COLLISIONS

Using the methods detailed above, the measurement and fitting of the $\pi^+\pi^+$ and $\pi^-\pi^-$ Bose-Einstein correlation functions have been done for 31 average transverse mass (m_T) bins ranging from 228 MeV/c^2 up to 871 MeV/c^2, for 0-30% central Au+Au events at $\sqrt{s_{NN}} = 200$ GeV. Three physical (λ, R, α) and two normalization ($N{\approx}1, \varepsilon{\approx}0$) parameters were extracted for each m_T bin. In the following I present the dependence of the extracted physical fit parameters on m_T.

The average transverse mass dependence of the λ, R, α parameters are shown on Figures 4.9, 4.10, and 4.11, respectively. The $\pi^+\pi^+$ and $\pi^-\pi^-$ results are statistically compatible. In case of the correlation strength parameter λ a saturation can be observed for higher m_T values, while for lower values, a strong decrease is seen. The Lévy scale parameter R shows a decreasing trend, similarly to the behav-

ior predicted by hydro calculations assuming a three-dimensional expansion for Gaussian ($\alpha \equiv 2$) sources. The Lévy index of stability α shows very little dependence on m_T, and a strong deviation from the Gaussian case. The parameters are also strongly correlated with each other, all combinations having correlation coefficients well above 90%.

4.2.1 *Discussion and interpretation of the results*

In this subsection more subtle physical interpretations of the measured trends of the parameters of the two-pion Bose-Einstein correlation functions are discussed. Starting with the Lévy exponent, one can observe that in each of the investigated cases, α values fall between 1 and 1.5. It is known, that for the random field 3 dimensional Ising model, the value of the η critical exponent is 0.5 ± 0.05 [156] while for the 3 dimensional Ising model (without external random fields) it is much less, 0.03631(3) [155]. If one assumes that a possible second order QCD phase transition falls in the same universality class as the 3 dimensional Ising-model [153, 154], and the η critical exponent is identical to the Lévy exponent α at the critical point [168], one can conclude (as expected), that for $\sqrt{s_{NN}} = 200$ GeV Au+Au collisions no signatures for a QCD critical point are seen. It is important however, to repeat similar measurements at different (lower) center-of-mass collision energies, and look for a possible non-monotonic behavior in the $\sqrt{s_{NN}}$ dependence. Results for the excitation function of the Lévy exponent α are shown in the following chapter.

Hydrodynamic calculations describing heavy-ion collisions often assume Gaussian source shapes [124]. The previous observations, however, show that in the investigated average pair momentum range the charged pion pair source function is well described with a Lévy distribution, having an index of stability $\alpha \approx 1.207$. The Lévy scale parameter R defines the length scale of the source. The hydro calculations for the Gaussian radius predict a transverse momentum scaling of $1/R^2 \propto m_T$. This scaling behavior, although clearly not having a Gaussian source, still holds approximately as shown in Figure 4.12. A linear $Am_T + B$ fit to $1/R^2$ versus m_T is also shown, taking into account only the statistical uncertainties when determining the best values and the statistical errors of the fit parameters.

The three physical fit parameters λ, α, and R are strongly correlated, which means that reasonably good (although not necessarily statistically acceptable) fits can be obtained with multiple sets of co-varied parameters. This motivated a search for less correlated parameter combinations, and without any theoretical motivation an interesting behavior was found for a new parameter defined as

$$\widehat{R} = \frac{R}{\lambda(1+\alpha)}. \tag{4.59}$$

If we substitute this parameter in place of the Lévy scale R in the fitting process, the obtained λ, R and α parameters remain the same, but the correlation coefficients will be substantially reduced, to the region of 20-30%. One can also observe an interesting linear m_T scaling in $1/\widehat{R}$ as shown in Figure 4.13. The possible physical interpretation of this fascinating affine linear dependence on m_T is yet unknown. More details about this parameter can be found in Ref. [9].

As it was discussed before, the deviation of $\lambda(m_T)$ from unity can have different implications. One of the possible scenarios is that for low m_T values a significant fraction of pions is a product of long-lived resonances (such as η, η', ω). The shape of $\lambda(m_T)$ can be compared to different theoretical models, taking into account in-medium mass modification, or partial coherence. Previous measurements and simulations often used the Gaussian approximation for the shape of the source, which usually result in lower λ values (due to the anti-correlation of λ and α). It is useful to investigate the normalized parameter $\lambda/\lambda_{\mathrm{max}}$, where the maximal value λ_{max} is defined as the average of $\lambda(m_T)$ on an m_T region where $\lambda(m_T)$ is approximately constant. Since $\lambda/\lambda_{\mathrm{max}}$ is less sensitive to the shape of the correlation function, some of the systematic uncertainties will be significantly decreased. The average transverse mass dependence of the normalized correlation strength parameter is shown on Figure 4.14. Within systematics, the data are not inconsistent with results of Refs. [137, 138] using a modified η' mass. To quantify the m_T dependence, a fit is shown with the following fit function:

$$\lambda(m_T)/\lambda_{\mathrm{max}} = 1 - H \exp\left[-(m_T^2 - m_\pi^2)/(2\sigma^2)\right]. \tag{4.60}$$

In this function, parameter H measures the depth (intercept at $m_T = m_\pi$, i.e., $K_T = 0$), while parameter σ measures the width of the low-m_T decrease. The values of the two fit parameters are significantly different from zero, so the decrease in $\lambda(m_T)$ is statistically significant.

4.3 BEAM ENERGY AND CENTRALITY DEPENDENT RESULTS

The finalized results at $\sqrt{s_{NN}}$ = 200 GeV paved the way for multiple new types of measurements, such as three-particle correlations [169], three-dimensional correlations [170], centrality dependence [171], and beam energy dependence [1, 6]. In this section I present my results on the latter two cases, and discuss how I tackled the challenges presented by the low statistics of the lower energy datasets.

As I showed before, the main obstacle I had to face when turning to the lower center of mass collision energies was the smaller amount of data. I found three methods to increase statistics. I increased the number of generated background events for the event mixing, included mixed-detector pairs where the two members were identified in different detectors, and combined the correlation functions of positive and negative pion pairs. Furthermore, I used less average transverse momentum bins, to have more pairs in a given bin. In case of $\sqrt{s_{NN}} = 62$ GeV I used 8 m_T and 4 centrality classes, while for $\sqrt{s_{NN}} = 39$ GeV I used 6 m_T and 2 centrality classes. Even with all the previously mentioned methods, for the three lower energies ($\sqrt{s_{NN}} = 27$ GeV, 19 GeV, 15 GeV) it was still impossible to investigate m_T or centrality dependence. In order to measure the excitation function of the Lévy source parameters for all available collision energies, I also made a measurement using just one wide centrality selection (0-30%) and one average transverse mass range. At lower energies, I used wider m_T ranges while keeping the mean value, $\langle m_T \rangle$ the same.

In the following I review the beam energy, centrality and average transverse mass dependent preliminary results. For completeness, I also include the centrality dependent preliminary results at $\sqrt{s_{NN}} = 200$ GeV, published in ref. [171]. For the top three collision energies, the centrality and m_T dependence of the source parameters are shown on Figures 4.15-4.26. The excitation functions of the source parameters are shown on Figures 4.27-4.30.

For each centrality class and every center of mass collision energies the correlation strength parameter λ shows a decrease at low average transverse mass, and a saturation at higher values of m_T.

The Lévy scale parameter R shows a geometrical centrality dependence. For more central events, where the initial size of the system is bigger, values of R are higher. In contrast to the obvious centrality dependence, it seems that collision energy does not affect strongly the values of R at a given m_T and centrality range.

The Lévy exponent α is not constant as a function m_T but shows a weak dependence. It can be observed that its values are between 0.5 and 2 in all cases. This means that the shape of the two particle source function in these collision energies and centrality classes are far from both the Gaussian ($\alpha = 2$) case and the critical behavior ($\alpha \simeq 0.5$).

The newly found $\widehat{R}$ parameter still shows the surprising scaling behavior with the average transverse mass; only at higher m_T values can some deviation be seen. The geometrical centrality dependence is also apparent in this case.

The excitation functions of the source parameters show a weak non-monotonicity. It is important to note, however, that the statistical and systematic uncertainties become quite large at lower energies. It is also important to note that the Lévy scale α parameter is above 1 at the whole energy range so we are still far from the conjectured critical point value. Among all parameters, the previously discussed scaling parameter $\widehat{R}$ shows the statistically most significant change with energy.

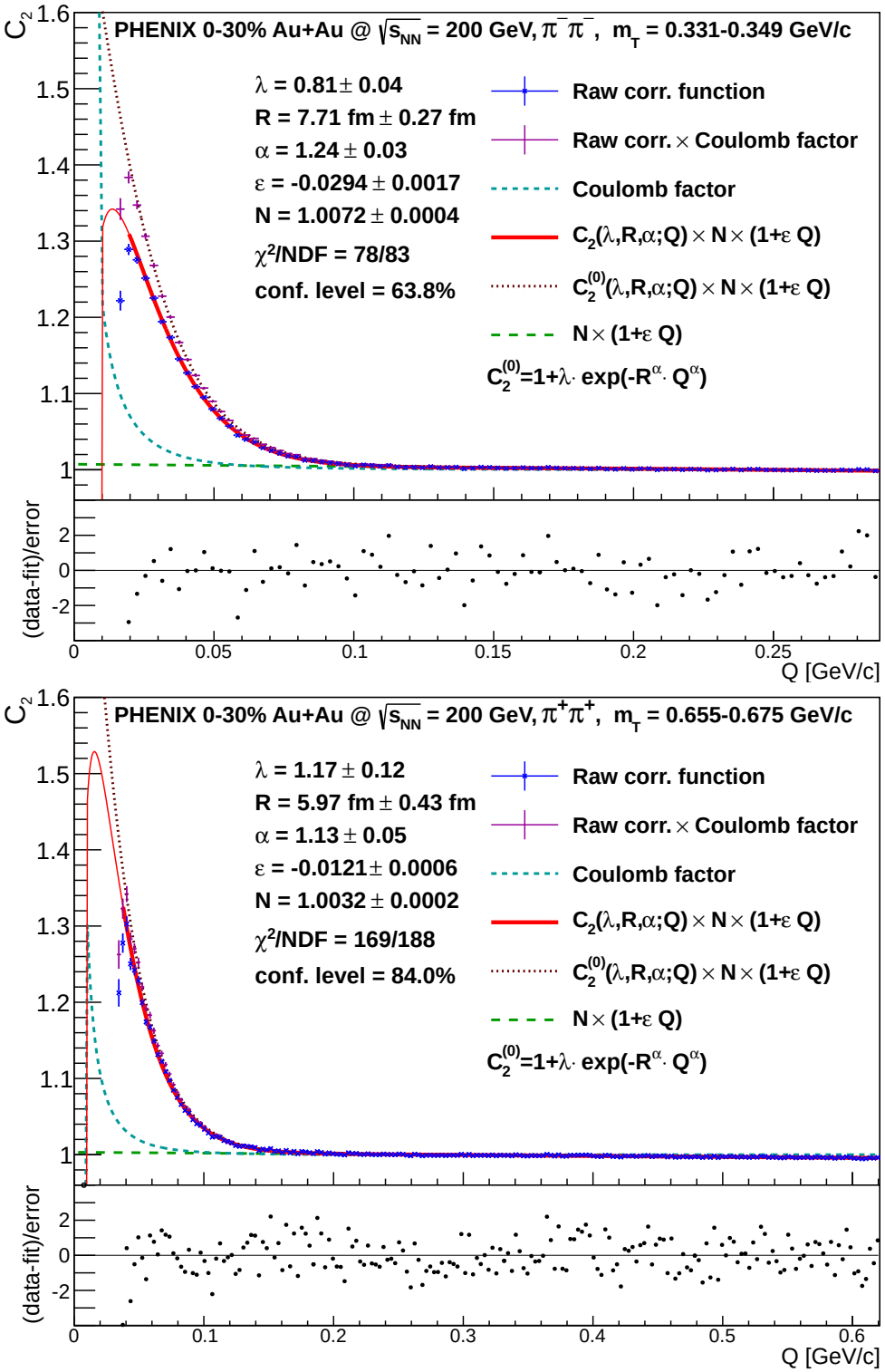

Figure 4.8: Example fits of Bose-Einstein correlation functions of (top) $\pi^-\pi^-$ pairs with average transverse mass m_T between 0.331 and 0.349 GeV/c^2 and of (bottom) $\pi^+\pi^+$ pairs with m_T between 0.655 and 0.675 GeV/c^2, as a function of relative momentum variable $Q \equiv |\boldsymbol{q}_{\mathrm{LCMS}}|$. Both fits show the measured correlation function and the complete fit function (described in 3.3.3), while a Bose-Einstein fit function $C_2^{(0)}(Q)$ is also shown, with the raw data multiplied by $C_2^{(0)}(Q)/C_2(Q)$. The first visible point on both panels corresponds to Q values below the accessible range (based on an evaluation of the two-track cuts), these were not taken into account in the fitting.

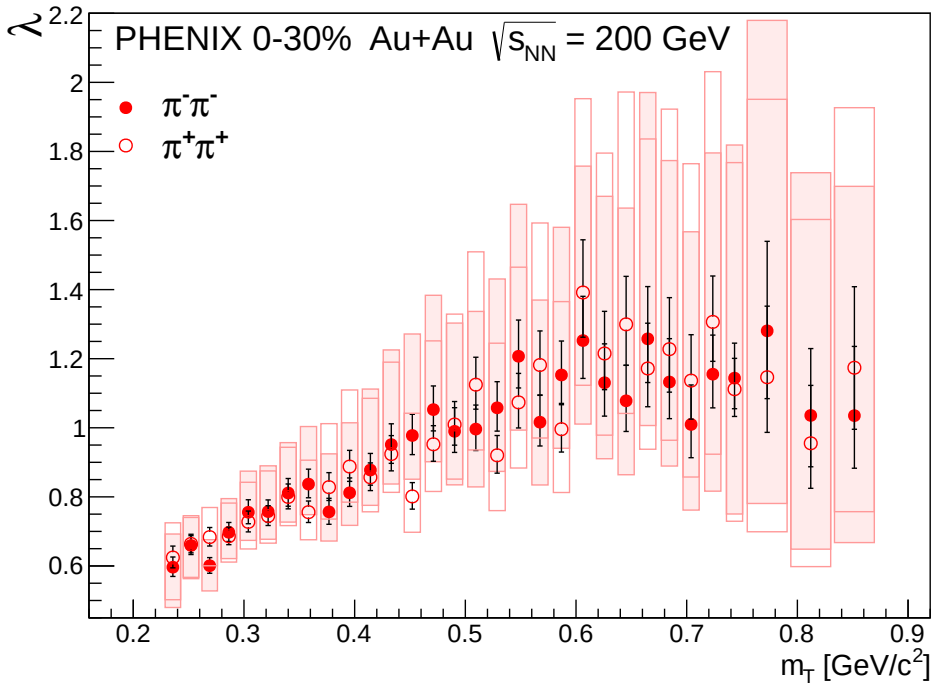

Figure 4.9: Correlation strength parameter λ versus average m_T of the pair, for 0%–30% centrality Au+Au collisions. The filled and empty markers represent negatively and positively charged pion pairs, respectively. Statistical and systematic uncertainties are shown as bars and boxes, respectively.

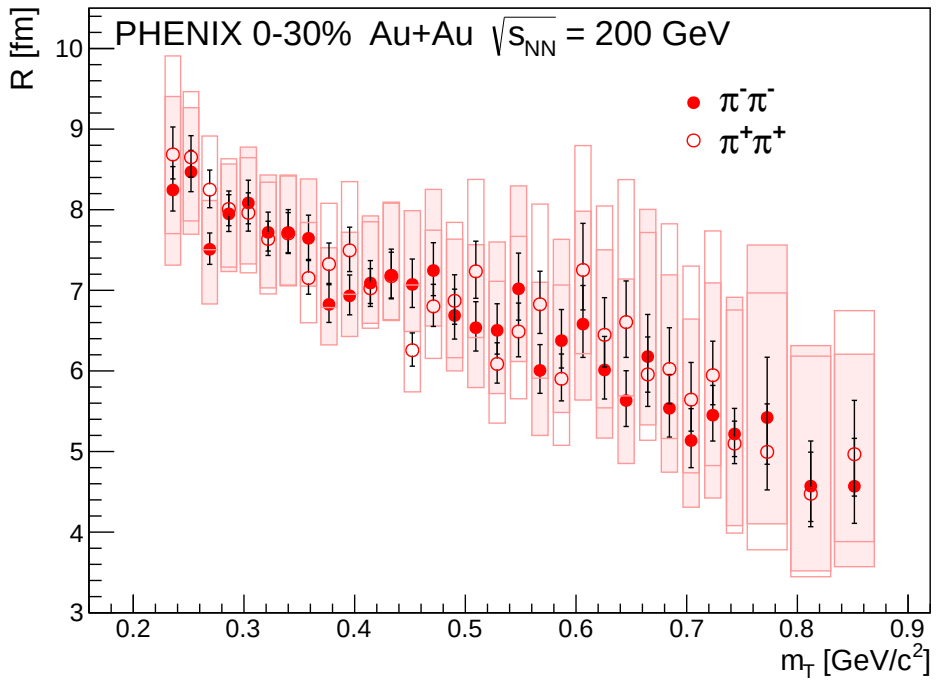

Figure 4.10: Lévy scale parameter R versus average m_T of the pair, for 0%–30% centrality Au+Au collisions. The filled and empty markers represent negatively and positively charged pion pairs, respectively. Statistical and systematic uncertainties are shown as bars and boxes, respectively.

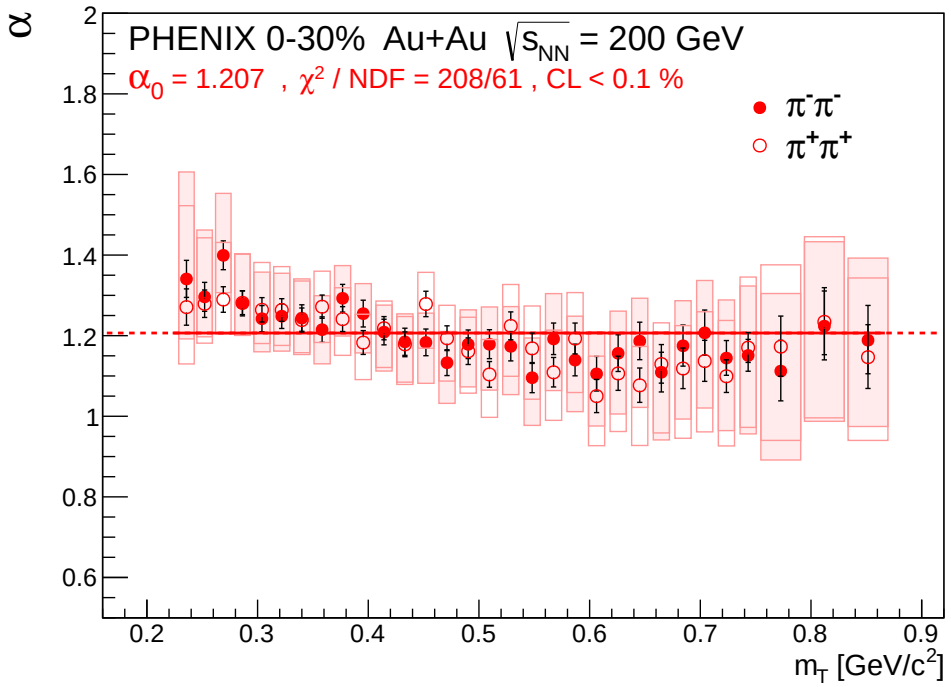

Figure 4.11: Lévy exponent parameter α versus average m_T of the pair, for 0%–30% centrality Au+Au collisions. The filled and empty markers represent negatively and positively charged pion pairs, respectively. Statistical and systematic uncertainties are shown as bars and boxes, respectively. The horizontal line, α_0=1.207, represents the m_T average value of α.

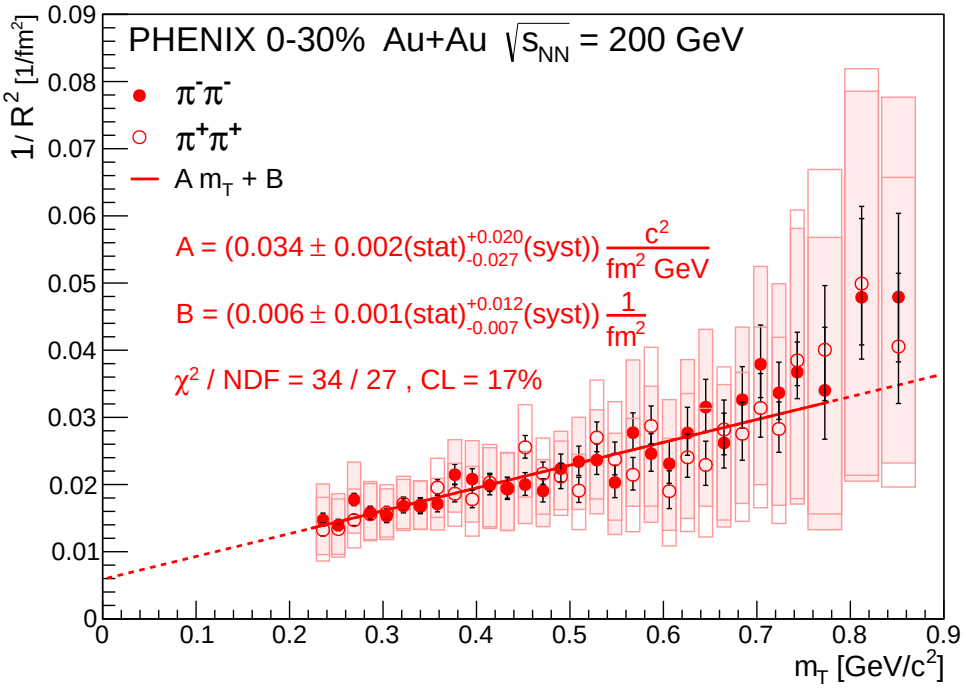

Figure 4.12: Inverse square of the Lévy scale parameter $1/R^2$ versus average m_T of the pair. Statistical and systematic uncertainties shown as bars and boxes, respectively.

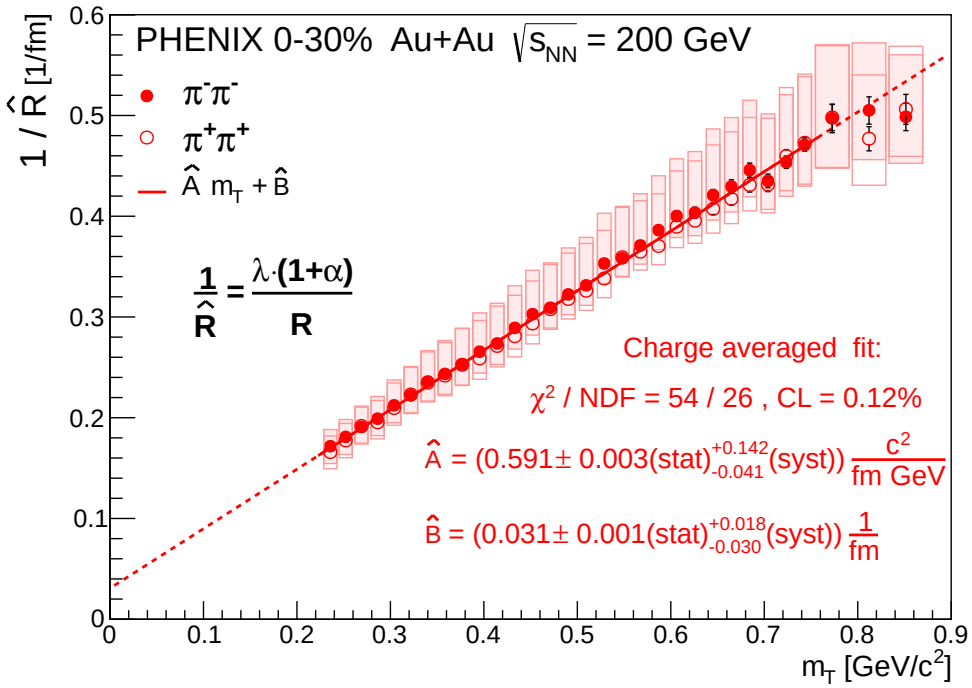

Figure 4.13: New scale parameter $\hat{R}$ versus average m_T of the pair, with a linear fit. Statistical and systematic uncertainties shown as bars and boxes, respectively.

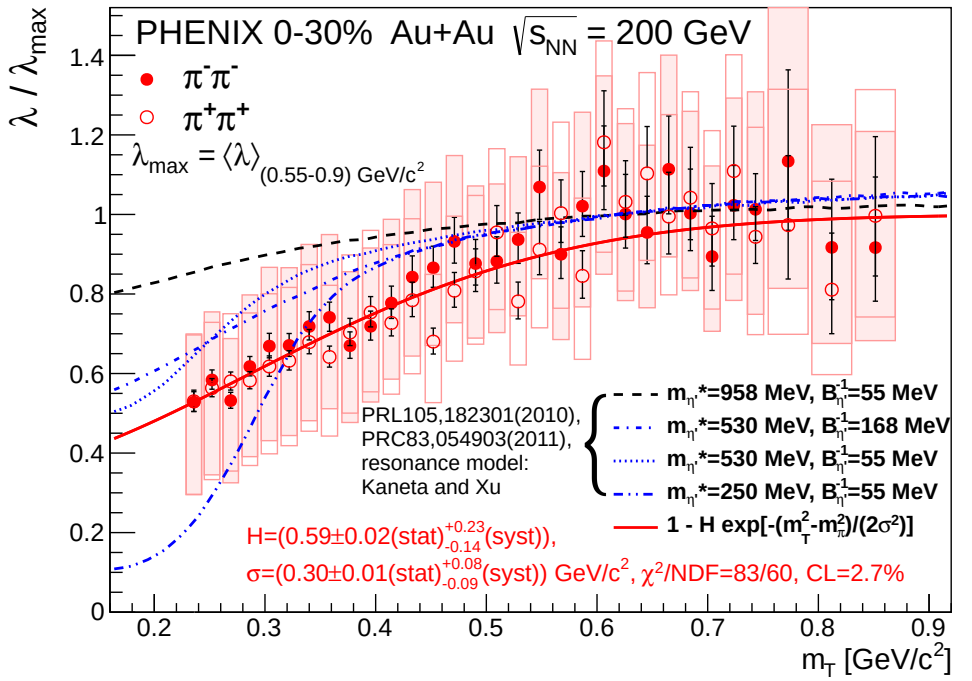

Figure 4.14: Normalized correlation strength parameter $\lambda/\lambda_{\max}$ versus average m_T of the pair. The data are compared with parameter scans from Refs. [137, 138] using different values of in-medium η' mass $m^*_{\eta'}$ and slope parameter $B^{-1}_{\eta'}$. To quantify the m_T dependence a fit with Equation 4.60 and the resulting H and σ parameters are also shown.

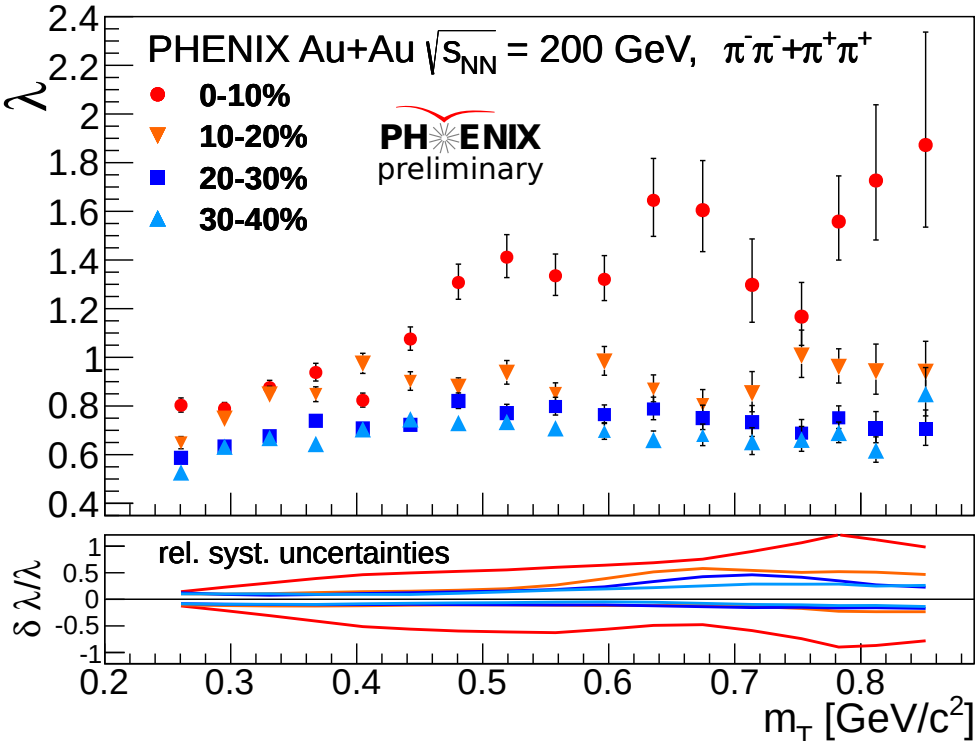

Figure 4.15: Centrality and average transverse mass m_T dependence of the correlation strength parameter λ for $\sqrt{s_{NN}}$ = 200 GeV Au+Au collisions. The different colors and marker styles indicate the different centrality classes. The auxiliary plot at the bottom shows relative systematic uncertainties.

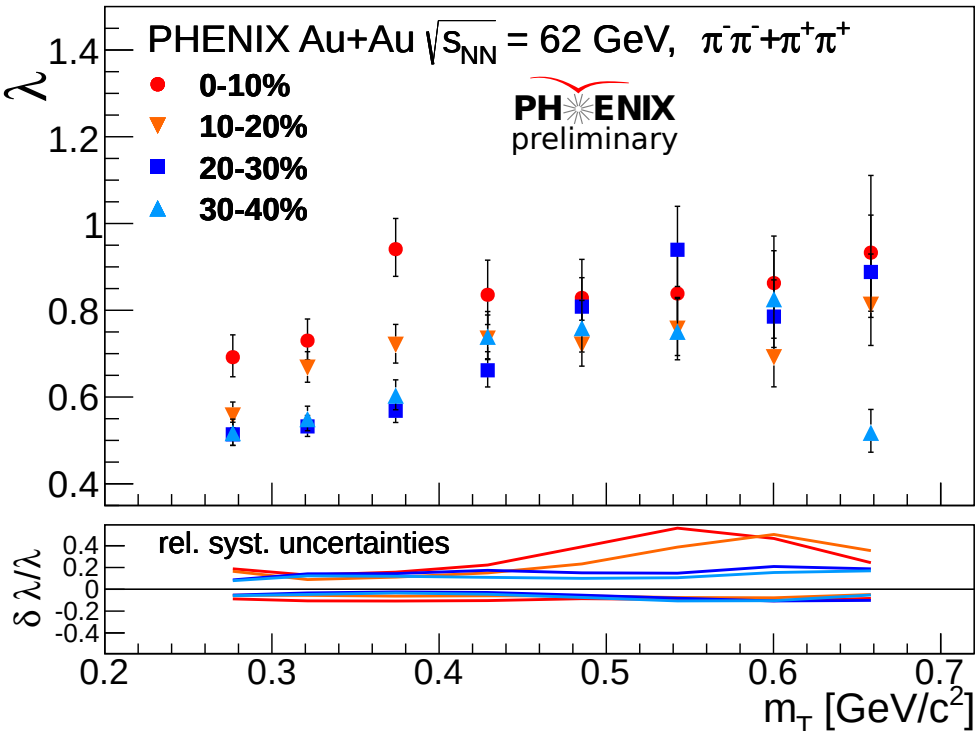

Figure 4.16: Centrality and average transverse mass m_T dependence of the correlation strength parameter λ for $\sqrt{s_{NN}}$ = 62 GeV Au+Au collisions. The different colors and marker styles indicate the different centrality classes. The auxiliary plot at the bottom shows relative systematic uncertainties.

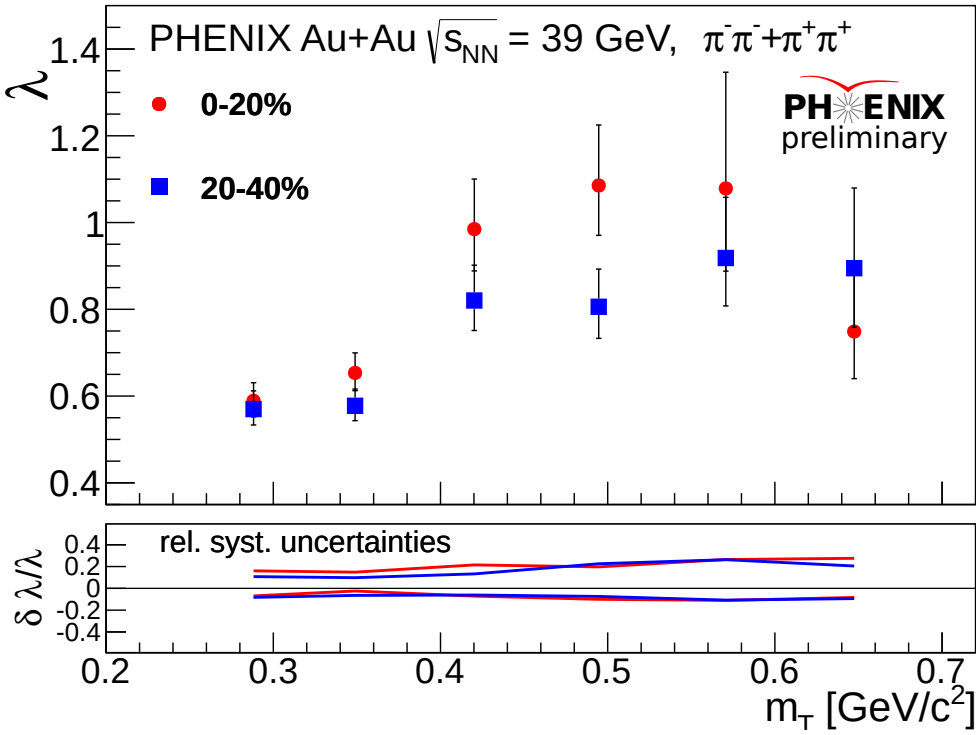

Figure 4.17: Centrality and average transverse mass m_T dependence of the correlation strength parameter λ for $\sqrt{s_{NN}}$ = 39 GeV Au+Au collisions. The different colors and marker styles indicate the different centrality classes. The auxiliary plot at the bottom shows relative systematic uncertainties.

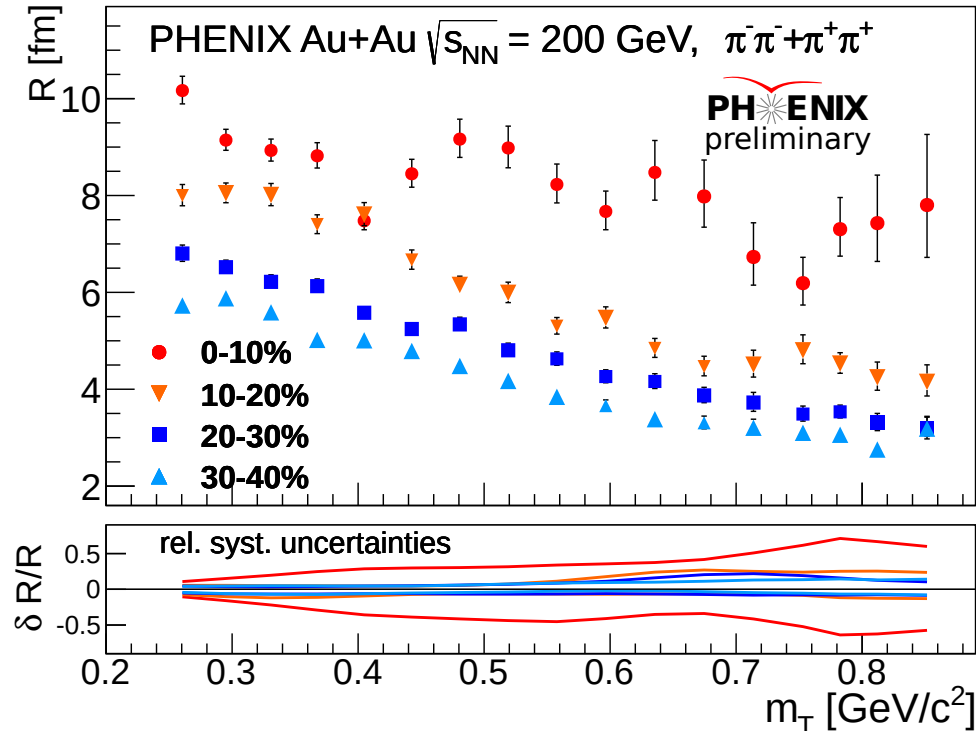

Figure 4.18: Centrality and average transverse mass m_T dependence of the Lévy scale R parameter for $\sqrt{s_{NN}}$ = 200 GeV Au+Au collisions. The different colors and marker styles indicate the different centrality classes. The auxiliary plot at the bottom shows relative systematic uncertainties.

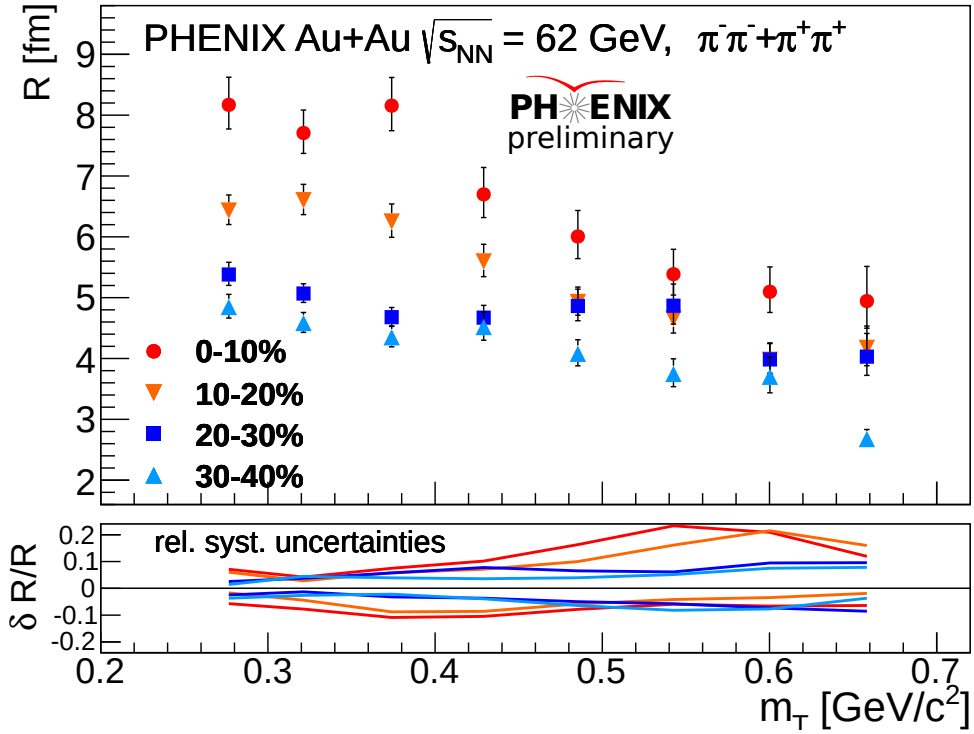

Figure 4.19: Centrality and average transverse mass m_T dependence of the Lévy scale R parameter for $\sqrt{s_{NN}}$ = 62 GeV Au+Au collisions. The different colors and marker styles indicate the different centrality classes. The auxiliary plot at the bottom shows relative systematic uncertainties.

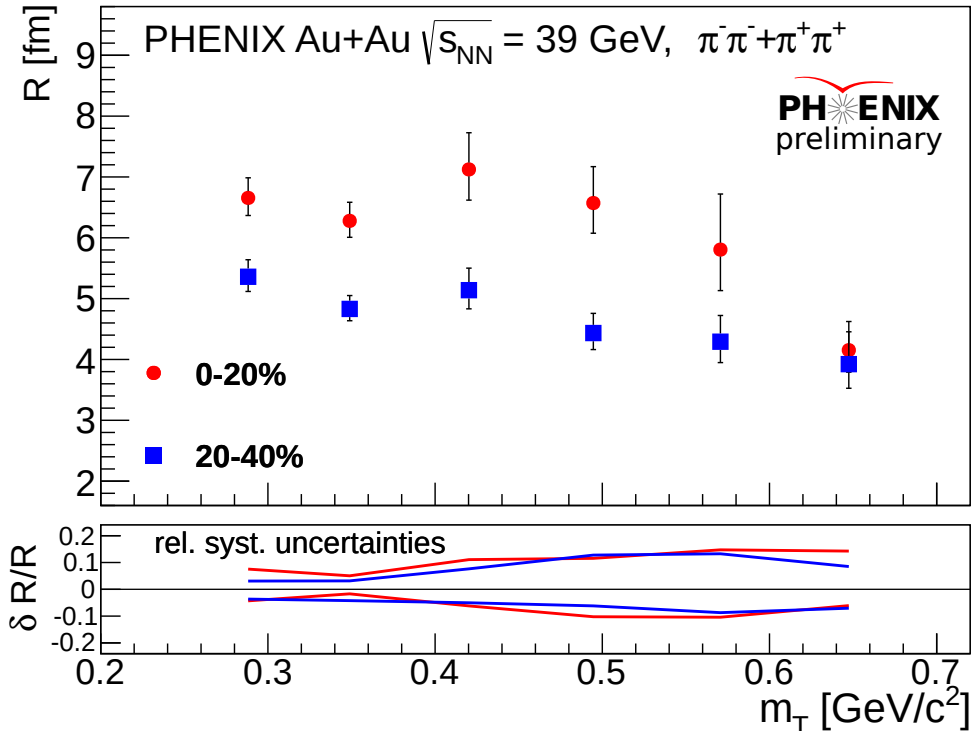

Figure 4.20: Centrality and average transverse mass m_T dependence of the Lévy scale R parameter for $\sqrt{s_{NN}}$ = 39 GeV Au+Au collisions. The different colors and marker styles indicate the different centrality classes. The auxiliary plot at the bottom shows relative systematic uncertainties.

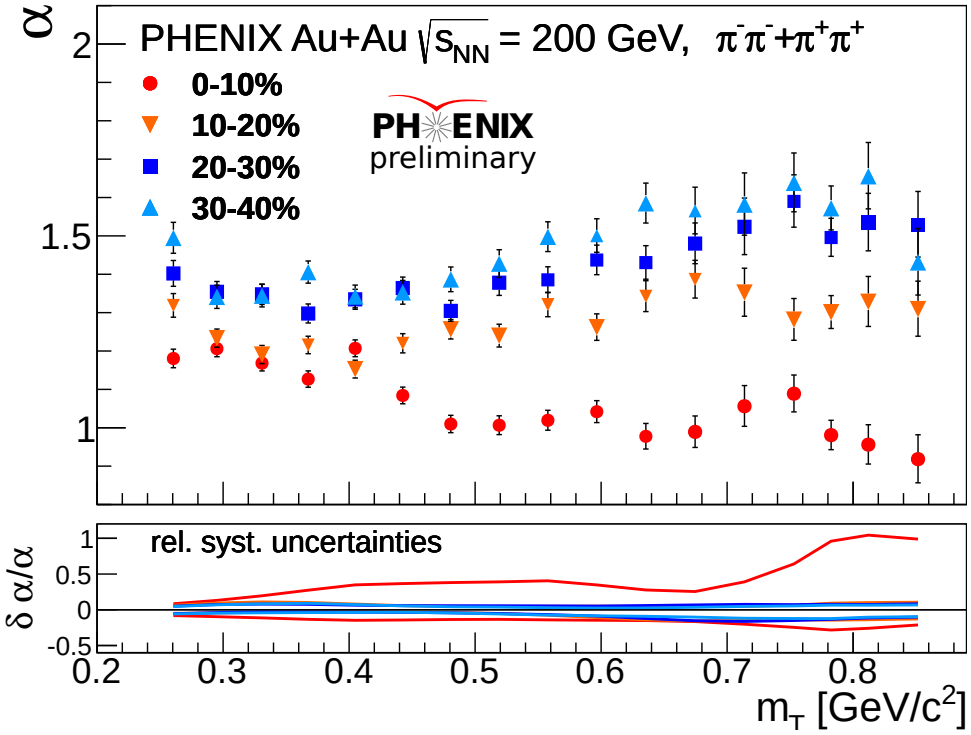

Figure 4.21: Centrality and average transverse mass m_T dependence of the Lévy exponent α parameter for $\sqrt{s_{NN}}$ = 200 GeV Au+Au collisions. The different colors and marker styles indicate the different centrality classes. The auxiliary plot at the bottom shows relative systematic uncertainties.

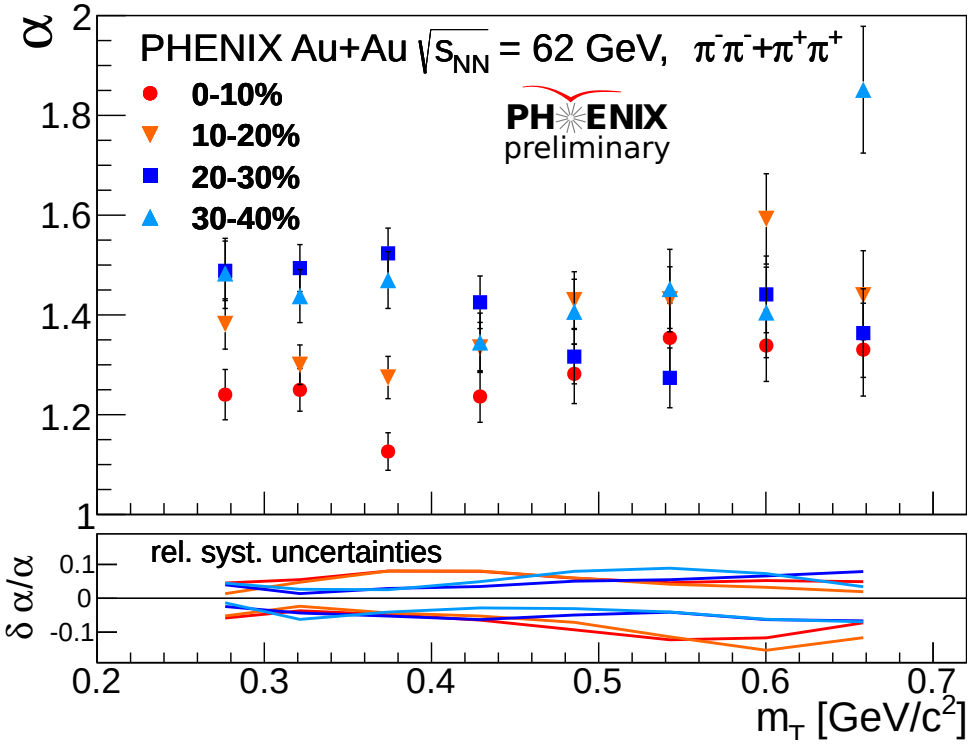

Figure 4.22: Centrality and average transverse mass m_T dependence of the Lévy exponent α parameter for $\sqrt{s_{NN}}$ = 62 GeV Au+Au collisions. The different colors and marker styles indicate the different centrality classes. The auxiliary plot at the bottom shows relative systematic uncertainties.

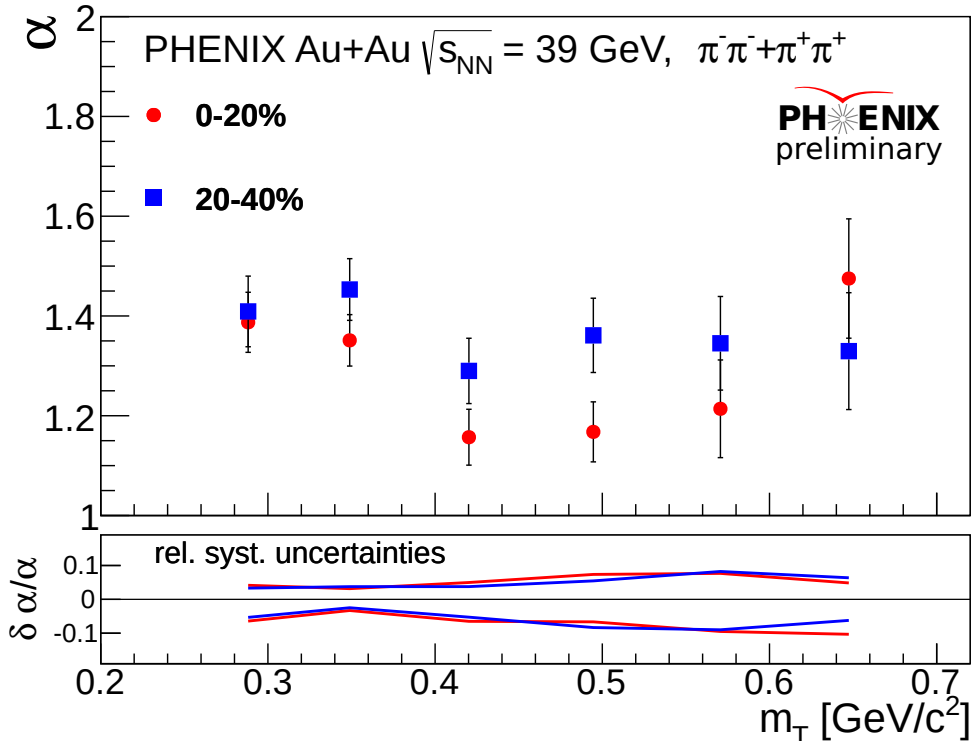

Figure 4.23: Centrality and average transverse mass m_T dependence of the Lévy exponent α parameter for $\sqrt{s_{NN}}$ = 39 GeV Au+Au collisions. The different colors and marker styles indicate the different centrality classes. The auxiliary plot at the bottom shows relative systematic uncertainties.

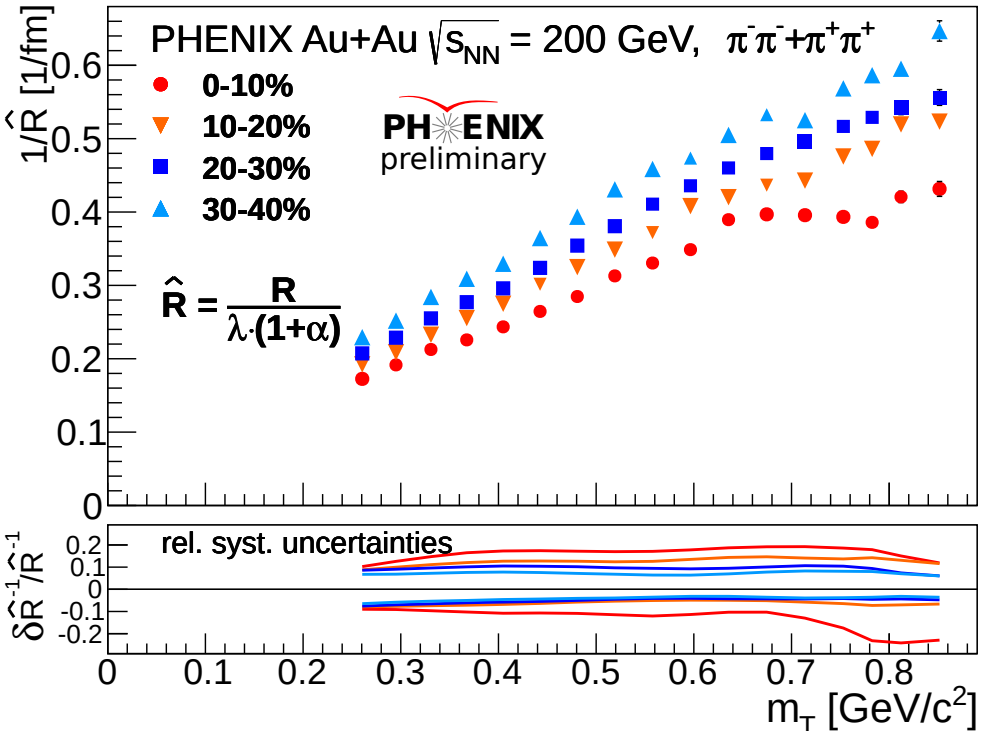

Figure 4.24: Centrality and average transverse mass m_T dependence of the inverse $\widehat{R}$ parameter for $\sqrt{s_{NN}}$ = 200 GeV Au+Au collisions. The different colors and marker styles indicate the different centrality classes. The auxiliary plot at the bottom shows relative systematic uncertainties.

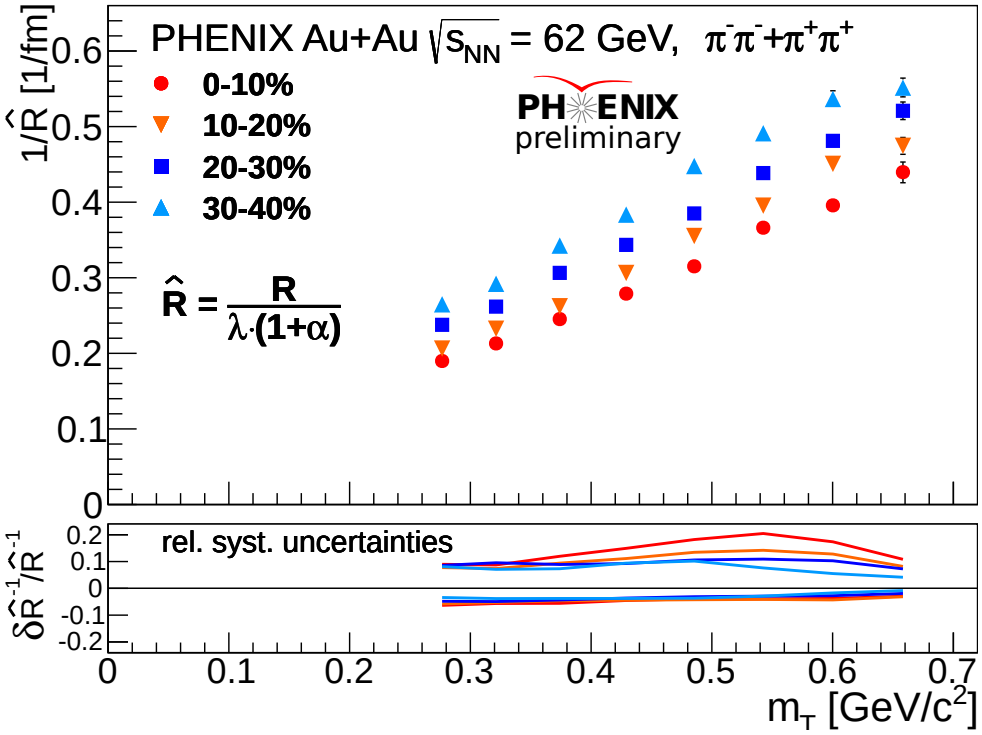

Figure 4.25: Centrality and average transverse mass m_T dependence of the inverse $\widehat{R}$ parameter for $\sqrt{s_{NN}}$ = 62 GeV Au+Au collisions. The different colors and marker styles indicate the different centrality classes. The auxiliary plot at the bottom shows relative systematic uncertainties.

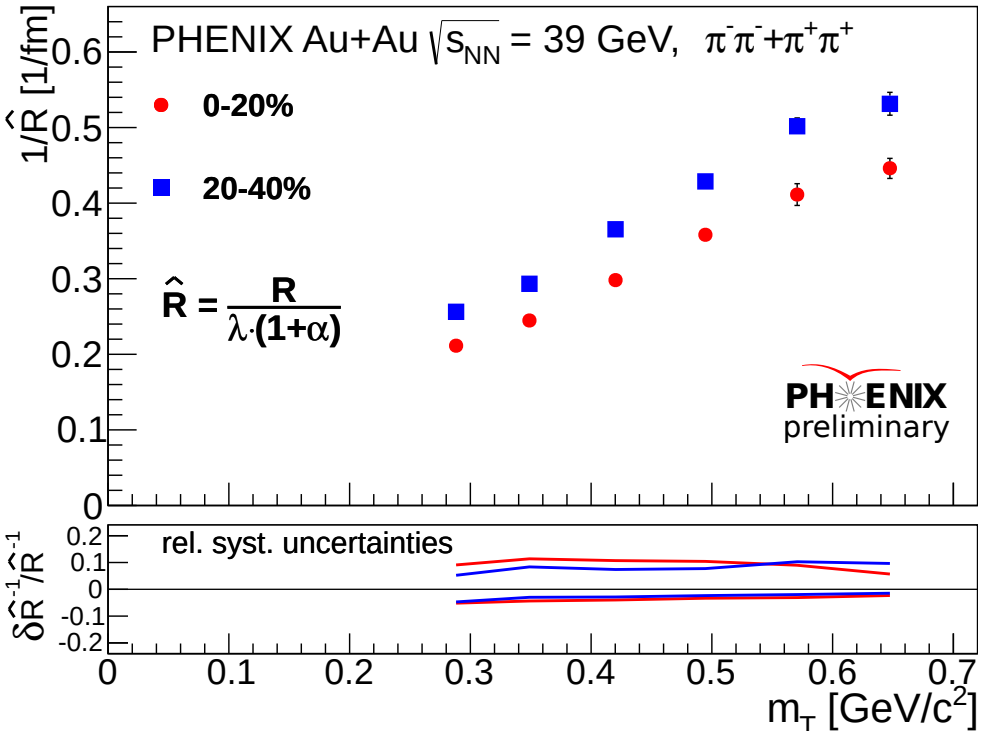

Figure 4.26: Centrality and average transverse mass m_T dependence of the inverse $\widehat{R}$ parameter for $\sqrt{s_{NN}}$ = 39 GeV Au+Au collisions. The different colors and marker styles indicate the different centrality classes. The auxiliary plot at the bottom shows relative systematic uncertainties.

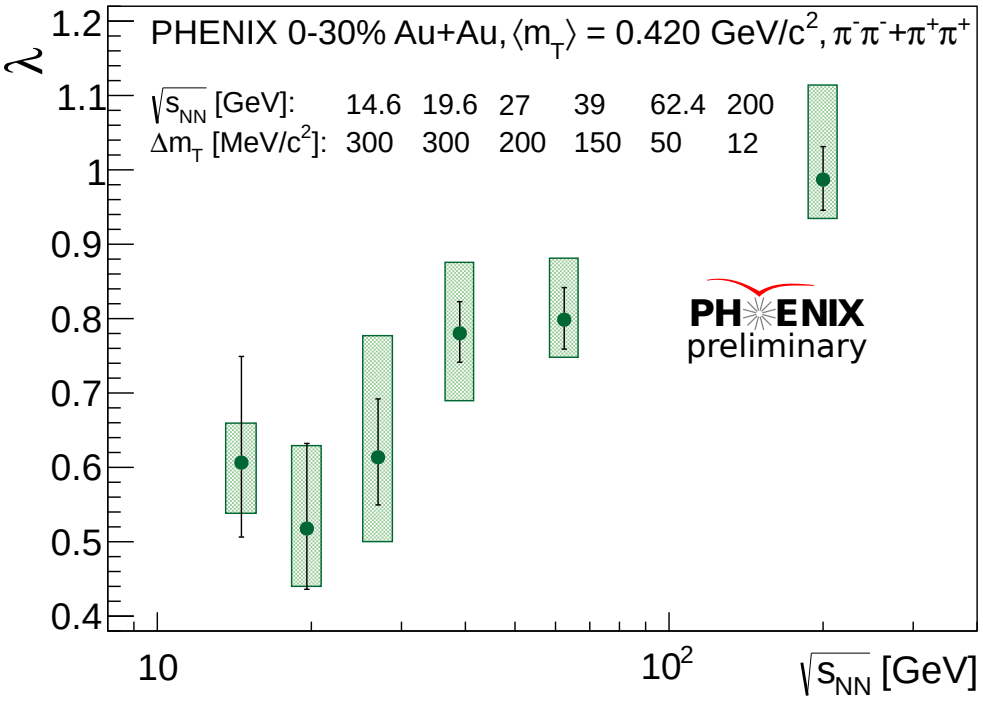

Figure 4.27: Excitation function of the correlation strength parameter λ in Au+Au collisions. The error bars represent the statistical uncertainties, while the filled boxes show the systematic uncertainties.

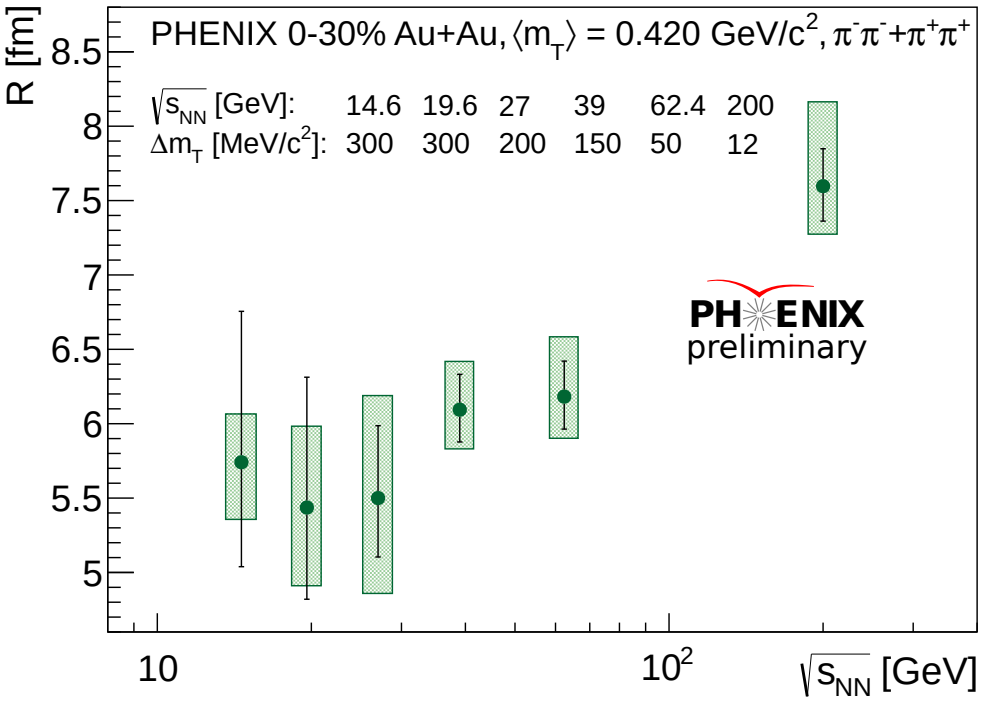

Figure 4.28: Excitation function of the Lévy scale parameter R in Au+Au collisions. The error bars represent the statistical uncertainties, while the filled boxes show the systematic uncertainties.

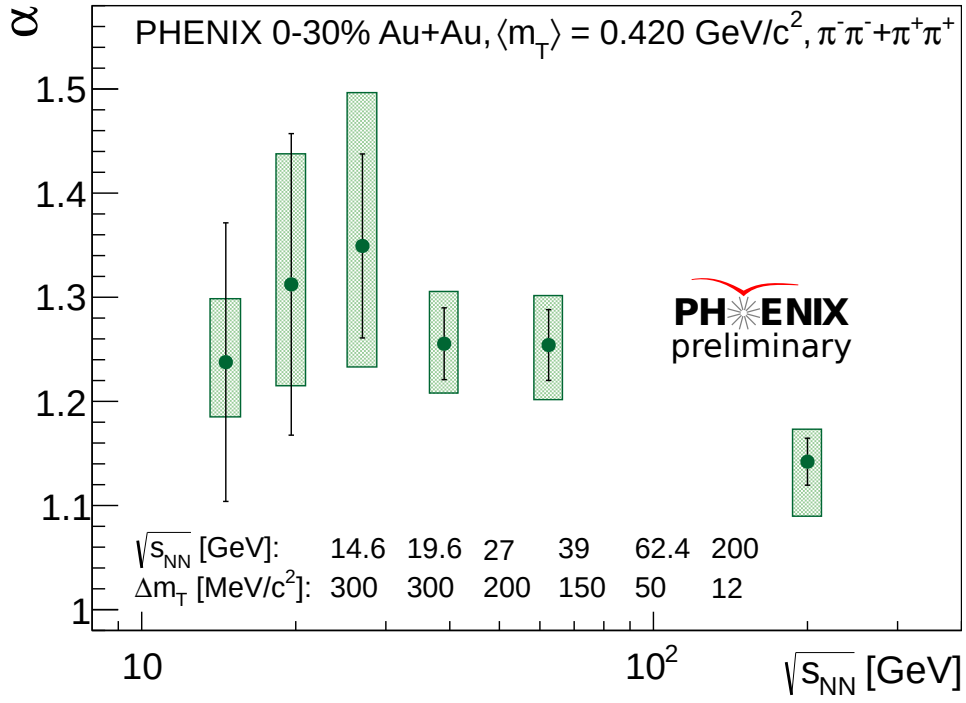

Figure 4.29: Excitation function of the Lévy exponent parameter α in Au+Au collisions. The error bars represent the statistical uncertainties, while the filled boxes show the systematic uncertainties.

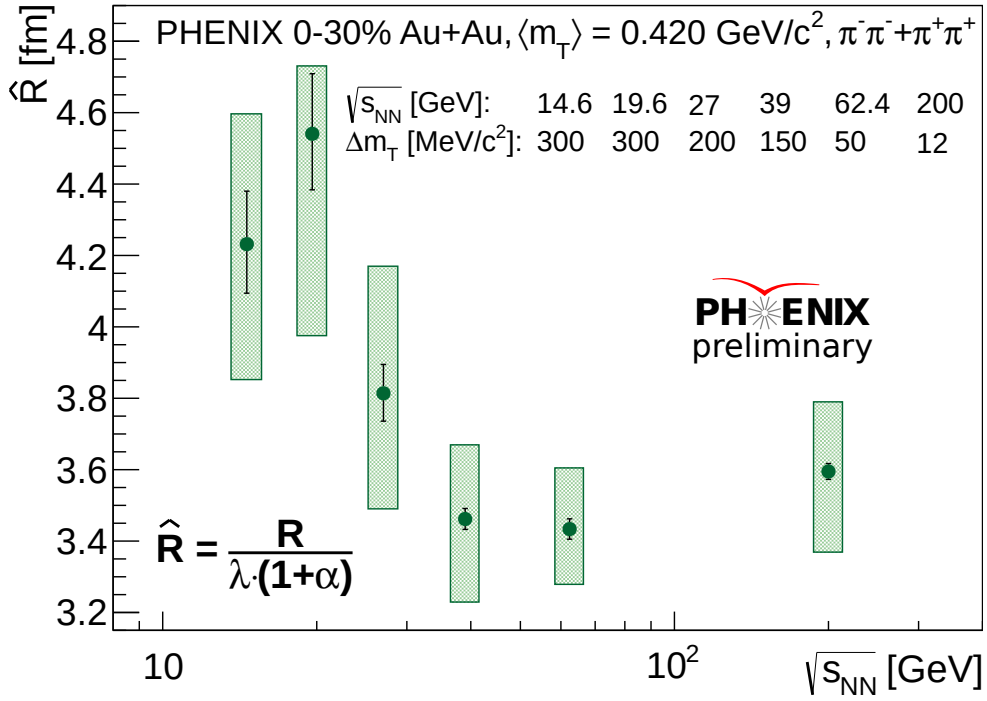

Figure 4.30: Excitation function of the $\hat{R}$ scaling parameter in Au+Au collisions. The error bars represent the statistical uncertainties, while the filled boxes show the systematic uncertainties.

5

LÉVY-HBT ANALYSIS AT STAR

Finalizing the PHENIX preliminary results on the beam energy dependence of the Lévy source parameters became quite challenging due to the low statistics and therefore the extremely large systematic and statistical uncertainties. To have a chance at getting results published for the Beam Energy Scan, after PHENIX was decommissioned I joined the STAR experiment, and started a similar pion correlation analysis (first for the top RHIC energy of 200 GeV). In this chapter I present the details of this work, and discuss the first preliminary results.

5.1 DETAILS OF THE ANALYSIS

The main steps of the analysis are the same as the one discussed in the previous chapter; however, there are detector specific event, track, and pair selection criteria that are unique to STAR. I summarized these in Table 5.1, and detail them below.

5.1.1 *Event selection*

For the analysis I used Run-10 Au+Au data recorded with the minimum-bias trigger. The full dataset contained about 400 million events. Although the total number of events is less than in the PHENIX Run-10 dataset (by almost a factor of 10), the statistics (the total number of pairs) is still much higher due to the full 2π acceptance of the detector in the azimuth angle. For a given event, the vertex position is determined by both the VPD and the TPC detectors. I applied the following vertex cuts (illustrated on Figure 5.1):

$$\begin{aligned} &|v_z^{VPD}| < 30 \text{ cm}, \\ &|v_z^{TPC}| < 30 \text{ cm}, \\ &|v_r^{TPC}| < 2 \text{ cm}, \\ &|v_z^{VPD} - v_z^{TPC}| < 3 \text{ cm}. \end{aligned} \tag{5.61}$$

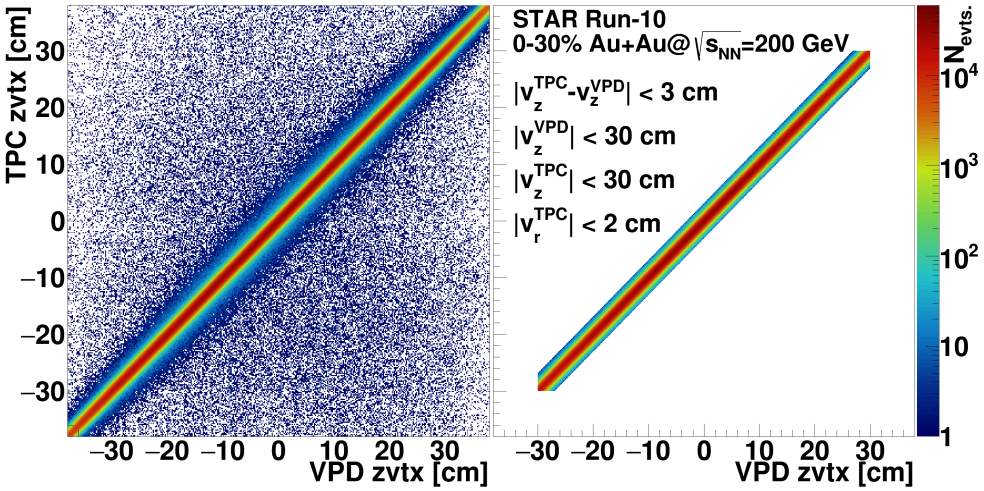

Figure 5.1: Vertex position v_z in the beam direction measured by TPC versus v_z measured by VPD.

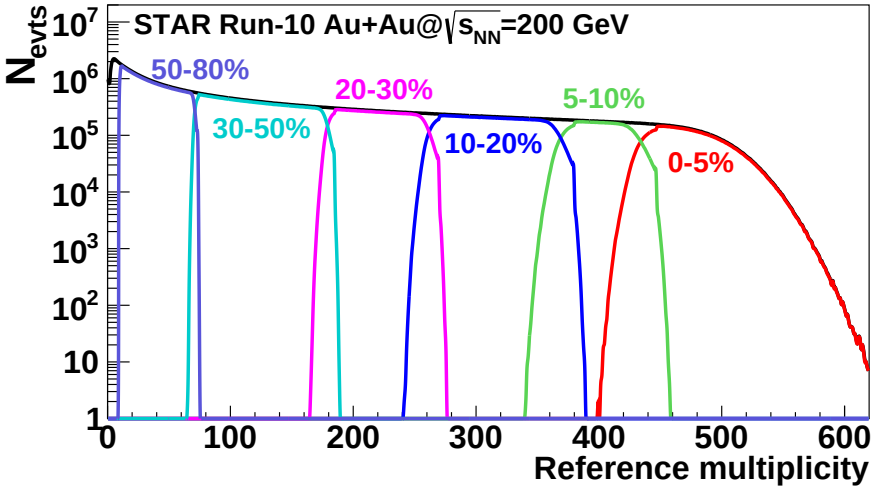

Figure 5.2: Reference multiplicity measured by the STAR TPC, and the defined centrality classes.

I used a centrality selection of 0-30%, inferred from reconstructed charged particle multiplicity in the TPC (reference multiplicity, illustrated on Figure 5.2). This reference multiplicity, together with multiplicity measured by TOF, was also used to cut on pile-up (multiple collision) events, as illustrated on Figure 5.3.

5.1.2 *Track selection*

Particle identification in STAR is mainly done by measurement of ionization energy loss (dE/dx) in the TPC, as illustrated on Figure 5.4. For a higher momentum range a complementary TOF identification can be used as well, however, for the momentum range used in this analysis this was not necessary. To obtain a clear pion sample I used

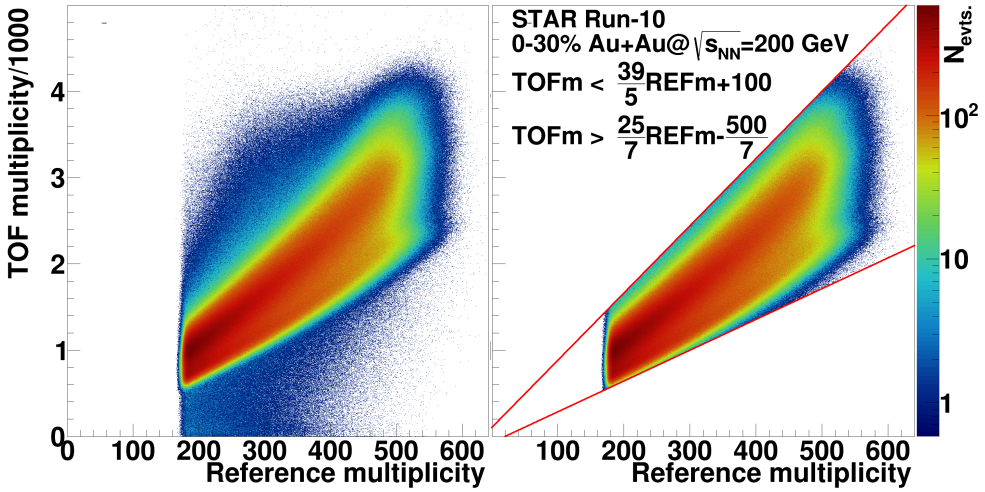

Figure 5.3: Multiplicity measured by TOF versus Reference multiplicity measured by TPC.

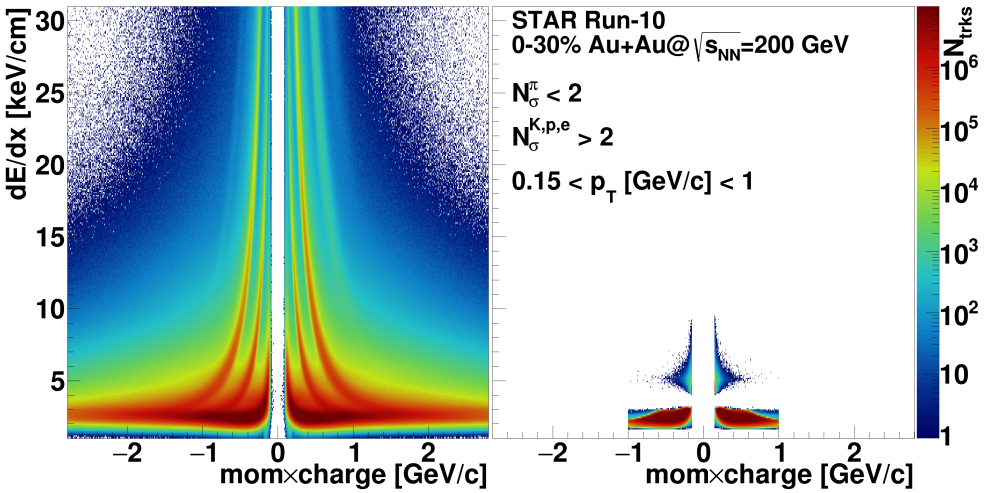

Figure 5.4: Pion identification with the STAR Time Projection Chamber using ionization energy loss.

a 2σ PID cut based on Ref. [172], as well as a 2σ veto cut on electrons, kaon, and protons.

When reconstructing tracks, a maximum number of 45 hits are avalable from the TPC readout segments (pad-rows) [102]. To filter out possible broken track fragments, I used a lower limit of 15 on the number of hits used to reconstruct a track. Furthermore, I used a track cut on the Distance of Closest Approach (DCA) variable (the smallest distance between the track and the primary vertex), requiring it to be less than 3 cm. I also applied a transverse momentum cut of $0.15\text{GeV}/c < p_T < 1\text{GeV}/c$.

5.1.3 *Pair selection*

As it is customary in STAR correlation analyses [173], I used separate methods to correct for the merging and splitting effects. The latter is investigated by defining the Splitting Level (SL) quantity for each pair of tracks:

$$SL = \frac{\sum_i S_i}{N_{hits,1} + N_{hits,2}}, \text{ where} \tag{5.62}$$

$$S_i = \begin{cases} +1 & \text{if one track leaves a hit on pad-row} \\ -1 & \text{if both tracks leaves a hit on pad-row} \\ 0 & \text{if neither track leaves a hit on pad-row,} \end{cases}$$

where i is the number of the TPC pad-row, and $N_{hits,1}$ and $N_{hits,2}$ are the total number of hits associated to each track in the pair. The range of the possible SL values is between -0.5 and 1, and usually the higher values correspond to possible split tracks, as illustrated on Figure 5.5 (a)-(b). In my analysis I used pairs with associated splitting level $SL < 0.6$.

Correcting for the merging effect was done by requiring that the Fraction of Merged Hits (FMH) value of a pair is less than 10%. Assuming that the tracks originated at the center of the TPC, using a helix model the pad-row hit positions, and then the distances between hits are calculated. The pair of hits is considered merged if their distance is less than a given value. For this calculation, TPC local coordinates are used, as illustrated on Figure 5.5 (c). The limiting values were $\Delta u^{in}_{min} = 0.8$ cm and $\Delta z^{in}_{min} = 3$ cm for the inner pad-rows, and $\Delta u^{out}_{min} = 1.4$ cm and $\Delta z^{out}_{min} = 3.2$ cm for the outer pad-rows.

5.2 RESULTS FOR $\sqrt{s_{NN}} = 200$ GEV AU+AU COLLISIONS

Using the previously discussed event, track, and pair selections, I measured the one-dimensional correlation functions of identical pion pairs with the event mixing method detailed in Section 3.3.2. For the background event pool I used 2 cm wide z vertex bins, and 5% wide centrality bins. I fitted the measured correlation function with the same method discussed in Section 4.1.4. An example Gaussian fit (with fixed $\alpha = 2$ value) is shown on Figure 5.6 (a), and an example Lévy fit (with a free α parameter) is shown on Figure 5.6 (b).

STAR 0-30% Au+Au @ $\sqrt{s_{NN}}$ = 200 GeV analysis cuts		
Event cuts	Track cuts	Pair cuts
$\lvert v_z^{VPD} \rvert < 30$ cm	$N_\sigma^\pi < 2$	$SL < 0.6$
$\lvert v_z^{TPC} \rvert < 30$ cm	$N_\sigma^{K,p,e} > 2$	$FMH < 0.1$
$\lvert v_r^{TPC} \rvert < 2$ cm	$N_{hits} > 15$	$\Delta u_{min}^{in} = 0.8$
$\lvert v_z^{VPD} - v_z^{TPC} \rvert < 3$ cm	$DCA > 3$ cm	$\Delta z_{min}^{in} = 3$
TOFm $< \frac{39}{5}$REFm$+100$	$0.15 < p_T[\mathrm{GeV}/c] < 1$	$\Delta u_{min}^{out} = 1.4$
TOFm $> \frac{25}{7}$REFm$-\frac{500}{7}$		$\Delta z_{min}^{out} = 3.2$

Table 5.1: Summary of the event, track, and pair selection criteria used in the STAR 0-30% Au+Au @ $\sqrt{s_{NN}}$ = 200 GeV data analysis.

Gaussian fits clearly do not provide a statistically acceptable description of the measured correlation functions (χ^2 values are more than a factor of 10 higher than the number of degrees of freedom). Despite this, the obtained values of the Lévy scale parameter R coincide with those measured in three-dimensional analyses such as Ref. [175]. Furthermore, what is immediately visible is the difference in fit quality between the two cases. The obtained χ^2 values drop by a factor of 3-5 after introducing the Lévy exponent α as a free fit parameter. Although there seems to be a much better agreement between the data points and the fit curve, since the data is extremely precise, the fit quality is still not acceptable.

The fact that the obtained Gaussian scale parameter values agree with those obtained from three-dimensional measurements, further support the use of the Q one-dimensional variable, as opposed to q_{inv}. In the latter case the obtained one-dimensional radii values differ, see e.g. Figures 6.6 and 6.7 of Ref. [174].

On Figure 5.6 (b) two main parts of the correlation function can be distinguished. There is a striking deviation between the data points and the fit curve at low values of the relative momentum variable, just below the correlation peak, at around $Q < 20$ MeV. Furhermore, on the range above, a characteristic oscillation pattern is observed in the auxiliary graph labeled (data-fit)/error. This graph shows the deviation of the data points from the fit curve values, divided by the statistical uncertainty of the data points. On this type of graph small deviations that are hard to see by eye are clearly visible.

The next step in the analysis was investigating the reason behind the observed behavior of the Lévy fits. I found that for small Q values,

the data is strongly affected by systematic variation of the pair cuts. The deviation of the data from the fit on this range is likely related to detector effects, such as the finite momentum resolution, and the pair reconstruction efficiency. These can be studied by Monte-Carlo simulations, which is an ongoing investigation. However, since on this region the systematic variation of the data points are extremely large, one can exclude this range from the fit limits. It is also important to note, that this low-Q deviation is not specific to the STAR detector system. Although much less prominent, it is visible for the PHENIX analysis as well (see Figure 4.8), and also present in the case of the CMS and NA61/SHINE analyses discussed in Refs. [145] and [176], respectively.

Even if the low-Q range is excluded from the fit interval, the extreme precision of the data points require a better description on the whole relative momentum interval. To have a deeper understanding of the shape of the correlation function, and possibly obtain a better description of the data, I turned to phenomenological investigations. In the next part of the thesis I detail the results of these approaches.

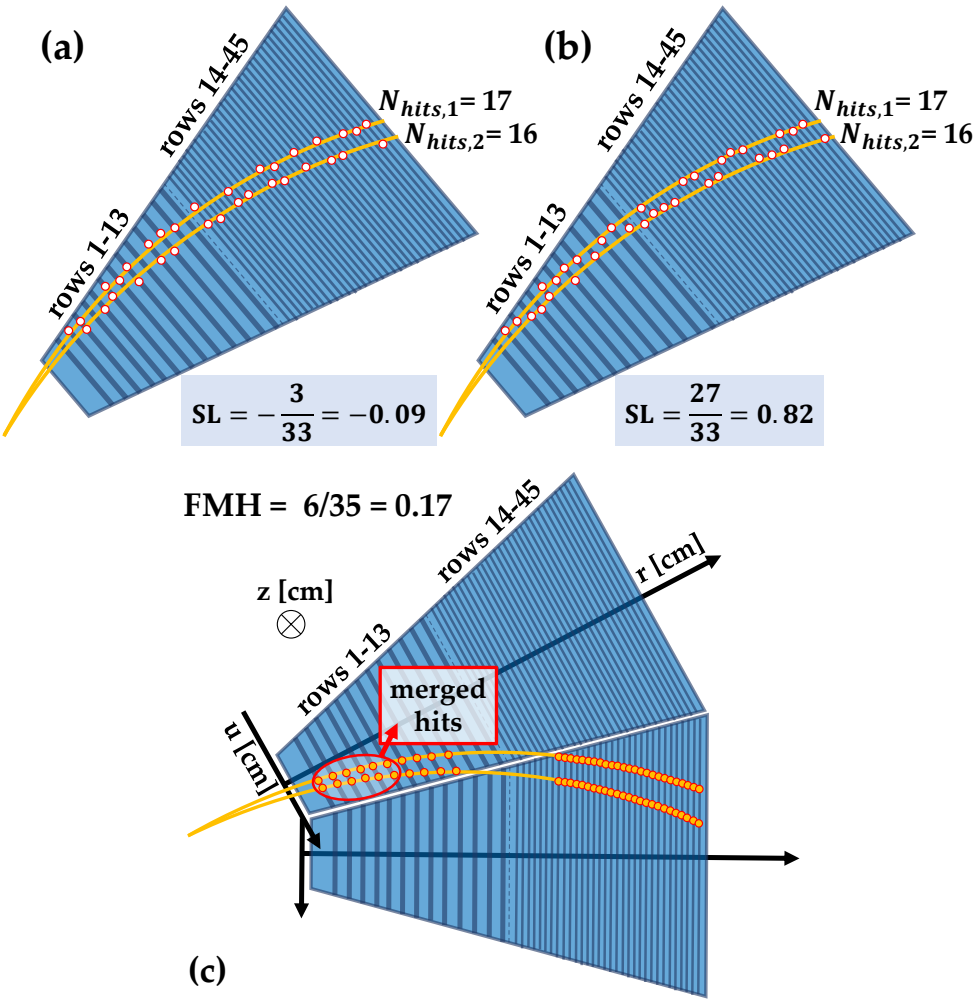

Figure 5.5: An illustration of the Splitting Level and Fraction of Merged Hits quantities. On panel (a)-(b), example distributions of the same total number of hits in two tracks are shown in a TPC sector. In case (a) the calculated splitting level is -0.09, these are likely separate tracks. In case (b) SL is 0.82, this is likely a split track. FMH is illustrated on panel (c). In this case, out of 45 pad rows there are 35 where the two tracks are in the same sector. For these the hit distances in the local coordinate u and z are calculated. Out of the 35 separation values, 6 is under the limit, so the value of FMH is 0.17.

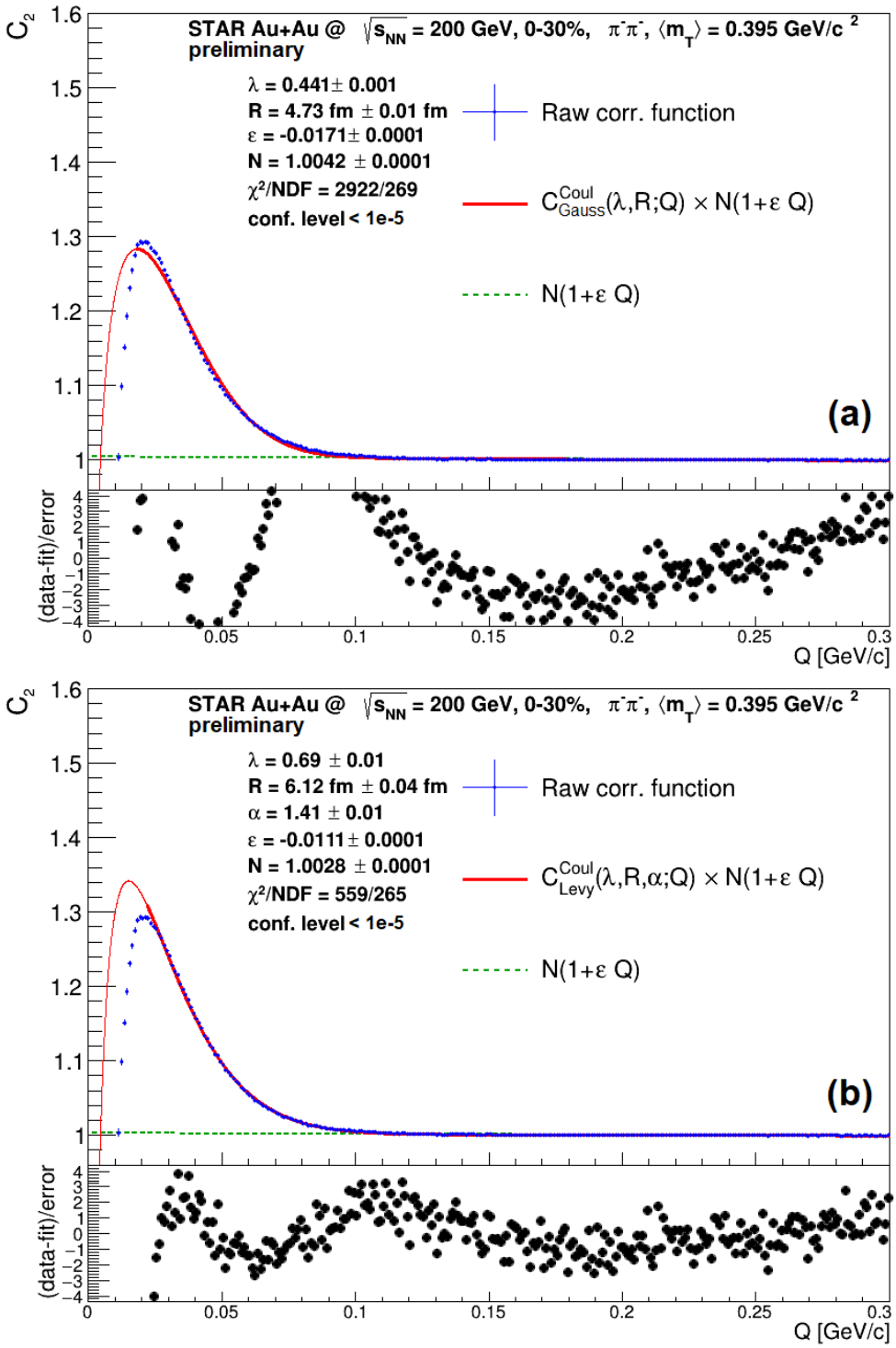

Figure 5.6: Example Gaussian (a) and Lévy (b) fits of a Bose-Einstein correlation function of $\pi^-\pi^-$ pairs with average transverse momentum k_T between 0.36 and 0.38 GeV/c as a function of relative momentum variable $Q \equiv |\boldsymbol{q}_{\mathrm{LCMS}}|$, defined in Equation 3.37. Both fits show the measured correlation function and the complete fit function (described in 3.3.3). The lower limit of the fit is around 20 MeV in both cases, marked with a line-width change.

Part III

PHENOMENOLOGICAL INVESTIGATIONS

Anyhow, after a lot of argument, drinking of sherry and chanting songs by Wagner and Schubert, Richard finally produced a mathematical theory of an optical intensity interferometer.

— R. Hanbury Brown [177]

6

COULOMB AND STRONG INTERACTIONS IN THE FINAL STATE OF HANBURY-BROWN-TWISS CORRELATIONS FOR LÉVY-TYPE SOURCE FUNCTIONS

When one tries to extract information about the two-particle source function through the analysis of femtoscopic correlations, it is of utmost importance to properly take into account final state interactions (FSI). The shapes of the experimentally measured correlation functions are significantly affected by these interactions (such as Coulomb repulsion and also strong interaction), and taking them into account in the theoretical framework is crucial. The effect of the Coulomb interaction and the methods to properly include it in the description of the correlation functions have been widely studied before, for details see e.g. Refs. [134, 178, 179]. However, final state strong interaction between like-sign pions is generally thought to have a small effect [180], so in most experimental analyses it is neglected. In this chapter I present a detailed calculation of the shape of two-pion HBT correlation functions with the assumption of Lévy stable source functions taking into account Coulomb and strong final state interactions.

This chapter is based on Ref. [2], and the structure is as follows:

Building on the basic definitions introduced in Sections 3.2.1-3.2.3, in Section 6.1. I investigate the effect of final state interactions on the pair wave function, and subsequently on the correlation function. In Section 6.2. I present results of a numerical calculation of the correlation function and investigate the differences between using only Coulomb or both Coulomb and strong interactions. Finally, in Section 6.3. I conclude and summarize my findings.

6.1 FINAL STATE INTERACTIONS

In this section I review the methodology of the calculation of a correlation function that includes the effect of the final state Coulomb and strong interactions. In doing so, I closely follow along the lines of

Ref. [178]. For the calculations discussed below, it is more advantageous to use the $\boldsymbol{k} = \boldsymbol{q}/2$ notation. With this, the correlation function can be written as

$$C_2(\boldsymbol{k}) = 1 - \lambda + \lambda \int d^3\boldsymbol{r} D_{(c,c)}(\boldsymbol{r}) \left|\Psi_{\boldsymbol{k}}^{(2)}(\boldsymbol{r})\right|^2. \tag{6.63}$$

As it was already discussed in the previous chapters, to calculate the shape of the $C_2(\boldsymbol{k})$ two-particle correlation function, one needs an assumption on the shape of the pair source $D_{(c,c)}(\boldsymbol{r})$, and a proper description of the effect of final state interactions enclosed in the $\Psi_{\boldsymbol{k}}^{(2)}(\boldsymbol{r})$ pair wave function. In the following, in Section 6.1.1. I proceed by discussing the calculation of $\Psi_{\boldsymbol{k}}^{(2)}(\boldsymbol{r})$ with the Coulomb and strong final state interactions included. Finally, in Section 6.1.2. I combine the previous calculations to derive the shape of the correlation function.

6.1.1 *The pair wave function*

Firstly let me introduce the Sommerfeld parameter η that appears frequently during calculations concerning the quantum mechanical Coulomb problem:

$$\eta \equiv \frac{\mu c^2 \alpha_{\text{QED}}}{\hbar c k}, \quad \mu = \frac{m_1 m_2}{m_1 + m_2}. \tag{6.64}$$

Here μ is the reduced mass of the particle pair, and $\alpha_{\text{QED}} \approx 1/137$ is the fine structure constant (not to be confused with the Lévy index α introduced earlier).

A normalization constant $\mathcal{N}$ appears in many contexts in the Coulomb wave function. Its definition is

$$\mathcal{N} = e^{-\pi\eta/2}\Gamma(1+i\eta), \tag{6.65}$$

and its modulus square, which is called the Gamow factor, can be calculated with elementary functions (owing to the well known step and reflection properties of the gamma function) as

$$|\mathcal{N}|^2 = \frac{2\pi\eta}{e^{2\pi\eta} - 1}. \tag{6.66}$$

The Schrödinger equation in a repulsive Coulomb potential can be written as

$$\triangle\psi_{\boldsymbol{k}}(\boldsymbol{r}) - \frac{2\eta k}{r}\psi_{\boldsymbol{k}}(\boldsymbol{r}) = k^2\psi_{\boldsymbol{k}}(\boldsymbol{r}). \tag{6.67}$$

For the treatment of the final state interactions, one has to utilize the scattering wave solutions whose asymptotic form is a plane wave plus a spherical wave. Such solutions for the Coulomb potential are well known:

$$\begin{aligned}\psi_{\boldsymbol{k}}^{(+)}(\boldsymbol{r}) &= \mathcal{N}e^{i\boldsymbol{kr}}\mathbf{F}(-i\eta, 1, i(kr-\boldsymbol{kr})) = \\ &= \mathcal{N}e^{ikr}\mathbf{F}(1+i\eta, 1, -i(kr-\boldsymbol{kr})), \qquad (6.68)\\ \psi_{\boldsymbol{k}}^{(-)}(\boldsymbol{r}) &= \mathcal{N}^*e^{i\boldsymbol{kr}}\mathbf{F}(i\eta, 1, -i(kr+\boldsymbol{kr})) = \\ &= \mathcal{N}^*e^{-ikr}\mathbf{F}(1-i\eta, 1, i(kr+\boldsymbol{kr})). \qquad (6.69)\end{aligned}$$

Here $\mathbf{F}(a, b, z)$ is the (renormalized) confluent hypergeometric function (Kummer's function); its definition and some basic properties are recited in Appendix A. A well-known property shows that the two forms of each functions introduced here are indeed equal.

The connection between these wave functions is

$$\psi_{\boldsymbol{k}}^{(+)}(\boldsymbol{r}) = \left(\psi_{-\boldsymbol{k}}^{(-)}(\boldsymbol{r})\right)^*. \tag{6.70}$$

From the asymptotic expression of the confluent hypergeometric function one can verify that the asymptotic form of these wave functions is

$$\psi_{\boldsymbol{k}}^{(+)}(\boldsymbol{r}) \approx e^{i\boldsymbol{kr}}e^{i\eta\log(kr-\boldsymbol{kr})} + f_c(\vartheta)\frac{e^{ikr}}{r}e^{-i\eta\log(kr-\boldsymbol{kr})}, \tag{6.71}$$

$$\psi_{\boldsymbol{k}}^{(-)}(\boldsymbol{r}) \approx e^{i\boldsymbol{kr}}e^{-i\eta\log(kr+\boldsymbol{kr})} + f_c^*(\vartheta)\frac{e^{-ikr}}{r}e^{i\eta\log(kr+\boldsymbol{kr})}. \tag{6.72}$$

Here the notation $f_c(\vartheta)$ stands for the Coulomb scattering amplitude, which is defined as

$$f_c(\vartheta) = -\frac{\eta}{2k}\frac{1}{\sin^2\frac{\vartheta}{2}}\frac{\Gamma(1+i\eta)}{\Gamma(1-i\eta)}. \tag{6.73}$$

One indeed sees that asymptotically the $\psi_{\boldsymbol{k}}^{(+)}(\boldsymbol{r})$ and the $\psi_{\boldsymbol{k}}^{(-)}(\boldsymbol{r})$ wave functions contain a plane wave plus an outgoing or an incoming

spherical wave, respectively. There are logarithmic factors stemming from the long range nature of the Coulomb interaction that distort both of them; these factors do not influence the physical meaning of the wave functions. The $\psi_{\boldsymbol{k}}^{(+)}(\boldsymbol{r})$ and the $\psi_{\boldsymbol{k}}^{(-)}(\boldsymbol{r})$ functions are called *in* and *out* scattering states, respectively.

It is a known fact that when calculating transition matrix elements, one has to utilize the $\psi_{\boldsymbol{k}}^{(-)}(\boldsymbol{r})$ state (the out state) for the wave function of the final state; this might seem somewhat counter-intuitive, since this function contains an incoming spherical wave. Similarly, one has to use $\psi_{\boldsymbol{k}}^{(+)}(\boldsymbol{r})$ for the initial state. See e.g. Ref. [181] for some details.

The scattering states written up here can be expanded in terms of energy eigenstates which are also angular momentum eigenstates. For given l and m angular momentum quantum numbers, one has two linearly independent angular momentum eigenstate solutions of the Schrödinger equation: their angle dependence is that of the $Y_{lm}(\vartheta,\varphi)$ spherical harmonic function, and their radial parts are called *regular* and *singular* Coulomb waves, respectively. I denote them here by $\mathcal{F}_{k,l}(r)$ and $\mathcal{G}_{k,l}(r)$ (as they depend on the k wave number magnitude and the l total angular momentum quantum number but not on the magnetic quantum number m); their expression is

$$\mathcal{F}_{k,l}(r) = e^{\pi\eta/2}(-1)^{l+1}4k(2kr)^l\times \\ \times\Re\Big\{e^{ikr+i\delta^c_{k,l}}\times U\big(l{+}1{+}i\eta,2l{+}2,-2ikr\big)\Big\}, \tag{6.74}$$

$$\mathcal{G}_{k,l}(r) = -e^{\pi\eta/2}(-1)^{l+1}4k(2kr)^l\times \\ \times\Im\Big\{e^{ikr+i\delta^c_{k,l}}\times U\big(l{+}1{+}i\eta,2l{+}2,-2ikr\big)\Big\}, \tag{6.75}$$

where the so-called Tricomi's function, $U(a,b,z)$ is another solution of the confluent hypergeometric equation (see Appendix A for some details). They are chosen for the set of linearly independent solutions because $\mathcal{F}_{k,l}$ is finite at the $r{=}0$ origin, and their asymptotic form is quite simple and straightforward: for $r\to\infty$ they can be expressed as

$$\mathcal{F}_{k,l}(r) \approx \frac{2}{r}\sin\left(kr-\frac{l\pi}{2}+\delta^c_{k,l}-\eta\log(2kr)\right), \tag{6.76}$$

$$\mathcal{G}_{k,l}(r) \approx \frac{2}{r}\cos\left(kr-\frac{l\pi}{2}+\delta^c_{k,l}-\eta\log(2kr)\right), \tag{6.77}$$

where the so-called Coulomb phase shift $\delta^c_{k,l}$ is defined as

$$\delta^c_{k,l} \equiv \arg\Gamma(l{+}1{+}i\eta). \tag{6.78}$$

One can also take a linear combination of these two functions whose asymptotic form contains an additional arbitrary $\Delta_{k,l}$ phase shift.

$$\mathcal{M}_{k,l}(r) := \cos\Delta_{k,l}\cdot\mathcal{F}_{k,l}(r)+\sin\Delta_{k,l}\cdot\mathcal{G}_{k,l}(r), \tag{6.79}$$

whose asymptotic form is

$$\mathcal{M}_{k,l}(r)\approx\frac{2}{r}\sin\left(kr-\frac{l\pi}{2}+\Delta_{k,l}+\delta^c_{k,l}-\eta\log(2kr)\right). \tag{6.80}$$

The above scattering-like solutions of the Schrödinger equation can be expanded in partial waves as

$$\psi^{(-)}_{\boldsymbol{k}}(\boldsymbol{r})=\sum_{l=0}^{\infty}\frac{2l+1}{2k}(-i)^l P_l(\cos\vartheta)e^{-i\delta^c_l}\mathcal{F}_{k,l}(r). \tag{6.81}$$

Owing to the short range of strong interaction, we can treat its effect by introducing the $\Delta^s_{k,0}$ s-wave „strong" phase shift, and modifying the s-wave component of the exact Coulomb wave function to a s-wave which contains this additional phase shift (see more details in e.g. Ref [182]). This is done by replacing the $\mathcal{F}_{k,0}$ function in the l=0 term in the expansion (6.81) with the above defined $\mathcal{M}^s_{k,0}(r)$ function which contains the additional $\Delta^s_{k,0}$ phase shift:

$$\psi^{(-)}_{\boldsymbol{k}}(\boldsymbol{r}) \quad\rightarrow\quad \Psi^{\mathrm{cs}}_{\boldsymbol{k}}(\boldsymbol{r}), \tag{6.82}$$

so the wave function incorporating the Coulomb and strong interaction effects, $\Psi^{\mathrm{cs}}_{\boldsymbol{k}}(\boldsymbol{r})$, becomes

$$\begin{aligned}\Psi^{\mathrm{cs}}_{\boldsymbol{k}}(\boldsymbol{r}) &= \psi^{(-)}_{\boldsymbol{k}}(\boldsymbol{r})-\frac{e^{-i\delta^c_{k,0}}}{2k}\mathcal{F}_{k,0}(r)+\frac{e^{-i\delta^c_{k,0}}}{2k}e^{-i\Delta^s_{k,0}}\mathcal{M}^s_{k,0}(r)= \\ &= \psi^{(-)}_{\boldsymbol{k}}(\boldsymbol{r})-\frac{i}{2k}e^{-i(\delta^c_{k,0}+\Delta^s_{k,0})}\sin\Delta^s_{k,0}\big(\mathcal{F}_{k,0}+i\mathcal{G}_{k,0}\big).\end{aligned} \tag{6.83}$$

Substituting the formulas for the respective wave functions encountered here, we get

$$\begin{aligned}\Psi^{\mathrm{cs}}_{\boldsymbol{k}}(\boldsymbol{r}) &= e^{-ikr}\Big\{\mathcal{N}^*\mathbf{F}\big(1-i\eta,1,i(kr+\boldsymbol{kr})\big)+ \\ &+2i\sin\Delta^s_{k,0}e^{-i\Delta^s_{k,0}}e^{\pi\eta/2}e^{-2i\delta^c_{k,0}}U\big(1-i\eta,2,2ikr\big)\Big\}.\end{aligned} \tag{6.84}$$

For identical bosonic particles (e.g. pions) one needs the symmetrized two-particle wave function:

$$\Psi_{\boldsymbol{k}}^{(2)}(\boldsymbol{r}) := \frac{1}{\sqrt{2}}\left(\Psi_{\boldsymbol{k}}^{\mathrm{cs}}(\boldsymbol{r}) + \Psi_{\boldsymbol{k}}^{\mathrm{cs}}(-\boldsymbol{r})\right) =$$
$$= \frac{e^{-ikr}\mathcal{N}^*}{\sqrt{2}}\left\{\mathbf{F}\left(1-i\eta, 1, i(kr+\boldsymbol{kr})\right)+\mathbf{F}\left(1-i\eta, 1, i(kr-\boldsymbol{kr})\right)\right\}+$$
$$+\frac{e^{-ikr}}{\sqrt{2}}4i\sin\Delta_{k,0}^{s}e^{-i\Delta_{k,0}^{s}}e^{\pi\eta/2}e^{-2i\delta_{k,0}^{c}}U\left(1-i\eta, 2, 2ikr\right). \tag{6.85}$$

Finally, one needs to calculate the modulus square of the wave function. The $[\boldsymbol{r}\to-\boldsymbol{r}]$ term within the braces in the following expression represents terms similar to the ones that stand before it, just with a mirrored $\boldsymbol{r}$:

$$\left|\Psi_{\boldsymbol{k}}^{(2)}(\boldsymbol{r})\right|^2 = \left\{\frac{|\mathcal{N}|^2}{2}\mathbf{F}\left(1+i\eta, 1, -i(kr+\boldsymbol{kr})\right)\mathbf{F}\left(1-i\eta, 1, i(kr-\boldsymbol{kr})\right)+\right.$$
$$\left.+\frac{|\mathcal{N}|^2}{2}\left|\mathbf{F}\left(1-i\eta, 1, i(kr+\boldsymbol{kr})\right)\right|^2+[\boldsymbol{r}\to-\boldsymbol{r}]\right\} + \left\{4\sin\Delta_{k,0}^{s}e^{\pi\eta/2}\times\right.$$
$$\times\Re\left[\mathcal{N}\ \mathbf{F}\left(1+i\eta, 1, -i(kr+\boldsymbol{kr})\right)ie^{-i\Delta_{k,0}^{s}}e^{-2i\delta_{k,0}^{c}}U\left(1-i\eta, 2, 2ikr\right)\right]+$$
$$\left.+[\boldsymbol{r}\to-\boldsymbol{r}]\right\} - 8\sin^2\Delta_{k,0}^{s}e^{\pi\eta}\left|U\left(1-i\eta, 2, 2ikr\right)\right|^2. \tag{6.86}$$

6.1.2 *The two-particle correlation function*

In this section I combine the previously discussed approaches, and write up the complete functional form of the correlation function by plugging in Equation (6.86) to Equation (6.63).

$$C_2(k) = 1-\lambda+\lambda\cdot\mathcal{I}^{(c,c)}(k), \text{ where} \tag{6.87}$$
$$\mathcal{I}_{(c,c)}(k) = \int d^3\boldsymbol{r}D_{(c,c)}(\boldsymbol{r})\left|\Psi_{\boldsymbol{k}}^{(2)}(\boldsymbol{r})\right|^2 =$$
$$= 2\pi\int_0^\infty dr\ r^2D_{(c,c)}(r)\int_{-1}^{1}dy\left|\Psi_{\boldsymbol{k}}^{(2)}(\boldsymbol{r})\right|^2. \tag{6.88}$$

Substituting Eq. (6.86) into Eq. (6.88) we get the following expression:

$$\mathcal{I}^{(c,c)}(k) = 2\pi\Big\{|\mathcal{N}|^2\times\mathcal{I}^{(1)}(k) + |\mathcal{N}|^2\times\mathcal{I}^{(2)}(k) - \\ - 8\sin^2\Delta^s_{k,0}e^{\pi\eta}\times\mathcal{I}^{(3)}(k) + 8\sin\Delta^s_{k,0}e^{\pi\eta/2}\times \\ \times\,\Re\Big[i\mathcal{N}e^{-i\Delta^s_{k,0}}e^{-2i\delta^c_{k,0}}\mathcal{I}^{(4)}(k)\Big]\Big\}, \tag{6.89}$$

where the following integrals were introduced:

$$\mathcal{I}^{(1)} = \int_0^\infty \mathrm{d}r\, r^2 D_{(c,c)}(r)\int_{-1}^{1}\mathrm{d}y\,\big|\mathbf{F}\big(1-i\eta,1,ikr(1+y)\big)\big|^2, \tag{6.90}$$

$$\mathcal{I}^{(2)} = \int_0^\infty \mathrm{d}r\, r^2 D_{(c,c)}(r)\int_{-1}^{1}\mathrm{d}y\,\Big\{\mathbf{F}\big(1-i\eta,1,ikr(1+y)\big)\times \\ \times\,\mathbf{F}\big(1+i\eta,1,-ikr(1-y)\big)\Big\}, \tag{6.91}$$

$$\mathcal{I}^{(3)} = 2\int_0^\infty \mathrm{d}r\, r^2 D_{(c,c)}(r)\cdot\big|U\big(1-i\eta,2,2ikr\big)\big|^2, \tag{6.92}$$

$$\mathcal{I}^{(4)} = \int_0^\infty \mathrm{d}r\, r^2 D_{(c,c)}(r)\cdot U\big(1-i\eta,2,2ikr\big)\times \\ \times\int_{-1}^{1}\mathrm{d}y\,\mathbf{F}\big(1+i\eta,1,-ikr(1+y)\big). \tag{6.93}$$

The last step is to explore the dependence of the strong phase shift $\Delta^s_{k,0}$ on k. Using the notation of Ref. [178] we can relate $\Delta^s_{k,0}$ to the full (Coulomb+strong) scattering amplitude $f_c(k)$:

$$\sin\Delta^s_{k,0}e^{i\Delta^s_{k,0}} = k|\mathcal{N}|^2 f_c(k). \tag{6.94}$$

The scattering amplitude $f_c(k)$ can be expressed as [182]

$$f_c(k) = \left(\frac{1}{K(k)} - 2k\eta\left(h(\eta) + i\frac{|\mathcal{N}|^2}{2\eta}\right)\right)^{-1}, \tag{6.95}$$

where $h(\eta)$ is related to the digamma function ψ as

$$h(\eta) = \left[\psi(i\eta) + \psi(-i\eta) - \log(\eta^2)\right]/2. \tag{6.96}$$

The k dependence of $f_c(k)$ partly comes from the function $K(k)$, which can be expressed with the $\delta^{(2)}_{k,0}$ phaseshift (where the (2) super-

script denotes the $I = 2$ isospin channel, the only allowed channel in case of identical charged pion pairs):

$$K(k) = \frac{1}{k} \tan \delta^{(2)}_{k,0}. \tag{6.97}$$

If there would be no Coulomb, only strong interaction, $\delta^{(2)}_{k,0}$ would be identical to the previously introduced $\Delta^{s}_{k,0}$ strong phase-shift. One can find different parametrizations for $\delta^{(2)}_{k,0}$ in the literature, in the following I mention some of them. A simple parametrization can be found in J. Bijnens et al. [183]:

$$K(k) = \left(\frac{m_\pi}{a^{(2)}_0} + \frac{1}{2} r^{(2)}_0 k^2 \right)^{-1}, \tag{6.98}$$

where $a^{(2)}_0$ is called the scattering length, and $r^{(2)}_0$ is called the effective range. The latter can also be connected to a $b^{(2)}_0$ slope parameter as

$$r^{(2)}_0 = \frac{1}{m_\pi a^{(2)}_0} - \frac{2 m_\pi b^{(2)}_0}{\left(a^{(2)}_0\right)^2} - \frac{2 a^{(2)}_0}{m_\pi}. \tag{6.99}$$

This effective-range parametrization is thought to be useful when the scattering length is much larger than the range of the scattering potential [184], which is not the case for identical pion scattering. Another parametrization [185] better suited for our investigations can be written up with the help of the center-of-mass energy $s = 4(m^2_\pi + k^2)$ as

$$K(k) = \frac{2}{\sqrt{s}} \frac{4m^2_\pi - s^{(2)}_0}{s - s^{(2)}_0} \left(a^{(2)}_0 + \tilde{b}^{(2)}_0 \frac{k^2}{m^2_\pi} \right), \text{ where} \tag{6.100}$$

$$\tilde{b}^{(2)}_0 = b^{(2)}_0 - \frac{4 m^2_\pi a^{(2)}_0}{s^{(2)}_0 - 4 m^2_\pi}. \tag{6.101}$$

The $s^{(2)}_0$ parameter corresponds to the value of s where the phase shift passes through 90°. It usually has a negative value, indicating that for the $I = 2$ channel the phase remains below 90°. The

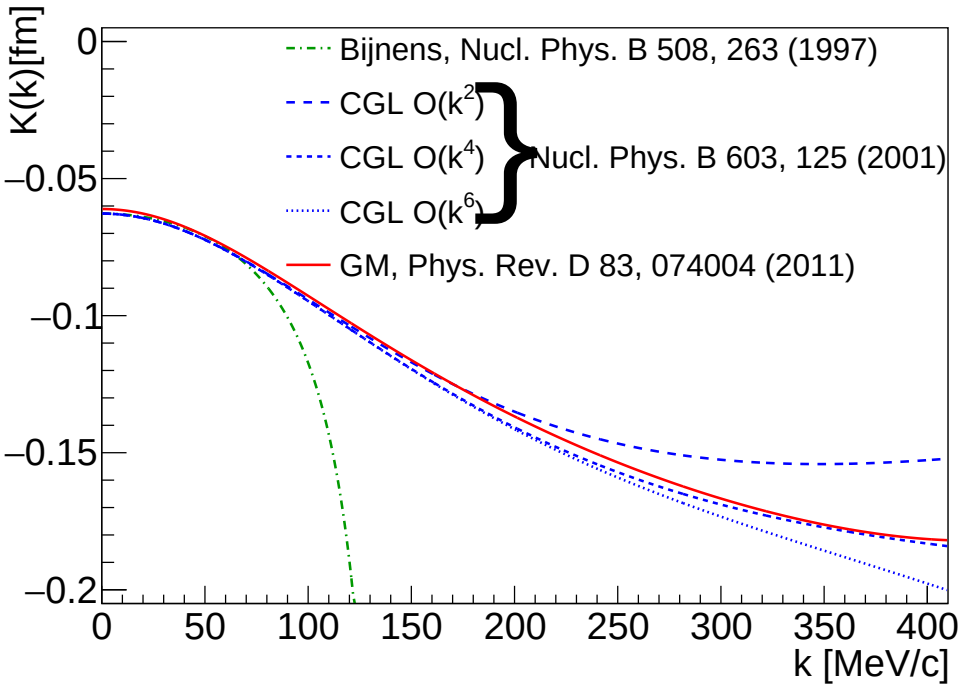

Figure 6.1: Comparison of different $K(k)$ parametrizations. See equations (6.98), (6.100), and (6.102) for Bijnens, CGL and GM, respectively.

parametrization can also be extended with higher order terms, the values of the parameters can be found e.g. in Colangelo-Gasser-Leutwyler (CGL) [186]: $a_0^{(2)} = -0.0444$, $b_0^{(2)} = -0.0803\ m_\pi^{-2}$, $s_0^{(2)} = -21.62\ m_\pi^2$.

A different parametrization can be found in a more recent paper from García-Martín et al. (GM) [187]:

$$K(s) = \frac{2}{\sqrt{s}} \frac{s - 2z_2^2}{m_\pi^2} \left(B_0 + B_1 \frac{\sqrt{s} - \sqrt{\hat{s} - s}}{\sqrt{s} + \sqrt{\hat{s} + s}} \right)^{-1}, \tag{6.102}$$

where the parameter values are the following: $z_2 = 143.5$ MeV, $B_0 = -79.4$, $B_1 = -63.0$, $\sqrt{\hat{s}} = 1050$ MeV. A comparison of the previously mentioned parametrizations can be seen on Fig.6.1. In the k range important for our investigations ($k \lesssim 100$ MeV/c) the different parametrizations give almost identical results, so in the following I utilized the most recent one from Ref. [187].

6.2 NUMERICAL RESULTS

In this section I present the results of the numerical calculation of $C_2(k)$ using a Lévy-stable source function (defined in Equation (3.30)). Using numerical integral calculations [188] I created a lookup table

for the function defined in Equation (6.89) for a wide range of values of k, R and α. This lookup table then was used to obtain the value of the function for any k, R and α by interpolation (within the available range).

If I omit the $\mathcal{I}^{(3)}$ and $\mathcal{I}^{(4)}$ terms from Eq. (6.89), I get back the pure Coulomb part. In the following, I compare the correlation function containing only the Coulomb interaction with the one containing both the Coulomb and the strong interactions, and try to give an estimate on the change in the values of the Lévy source parameters that is caused by the proper treatment of the strong interaction compared to the neglection of it.

From here on, I change the relative momentum variable to $Q = 2k$ to better compare to the notation of published experimental results.

6.2.1 *Comparison of Coulomb and strong FSI effects*

Fig. 6.2. shows the calculated correlation functions for three different Lévy-scale values at the same index of stability α and same correlation strength λ. It is clearly visible that turning on the strong interaction affects the strength of the correlation functions, however, the effect on the Lévy-scale R and the index of stability α is not so transparent at this point.

To investigate the effect of the strong interaction in more detail, I generated histograms by sampling the calculated functions containing both Coulomb and strong interactions. To make the generated correlation function resemble real data, I randomly scatter the points around the calculated function and assign a relative error proportional to $1/Q$ (which is a realistic assumption if one considers typical experimental scenarios). I then fit the generated data with the help of the ROOT Minuit2 minimizer framework, with a similar method to what is described in Ref. [9]. To check the validity of the fitting method, first I fit the generated histogram with the corresponding functional form to see if I get back the input parameter values. Fig. 6.3 shows such a fit to the generated data. The fit converged with an acceptable χ^2/NDF value, the error matrix turned out to be accurate, and for the output parameter I got back within errors the same ones as were given as input. I repeated this test for multiple different input parameter values and found that our fitting method is indeed reliable.

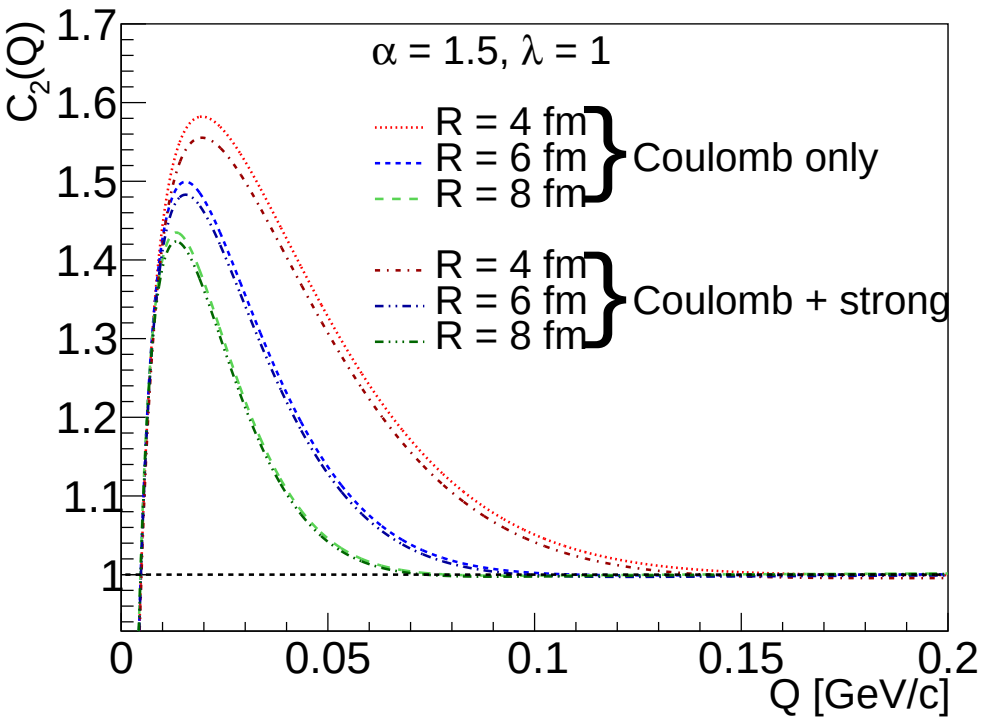

Figure 6.2: Two-pion correlation functions calculated for Lévy-stable sources. Three different Lévy-scale values are compared at the same index of stability $\alpha = 1.5$ and same correlation strength $\lambda = 1$. The functions containing only the Coulomb interaction and the ones including both the Coulomb and strong interactions are shown separately.

As a next step, I took the same generated data and fitted it with a function containing only the effect of the Coulomb interaction. Fig. 6.4 shows an example for such a fit on panel (a). The fit converged again, the error matrix again turned out to be accurate. The resulting χ^2 value becomes just slightly higher than before, nevertheless, the fit is still acceptable. Although in this case the function containing only the Coulomb interaction can provide an acceptable fit to the generated data which contains also the strong interaction, the values of the fit parameters differ from the input parameter values. It seems that in this case one underestimates the value of λ from such a fit, and overestimates α. Within this precision, it seems that the value of R is unaffected.

One can also assume that if the data is more precise, meaning that the fluctuation and the statistical uncertainty of the generated points are smaller, the fit will not provide an acceptable χ^2 anymore. To check this, I also generated such $C_2(Q)$ histrograms, and found that the Coulomb fits converged, but indeed the χ^2 values increase by a

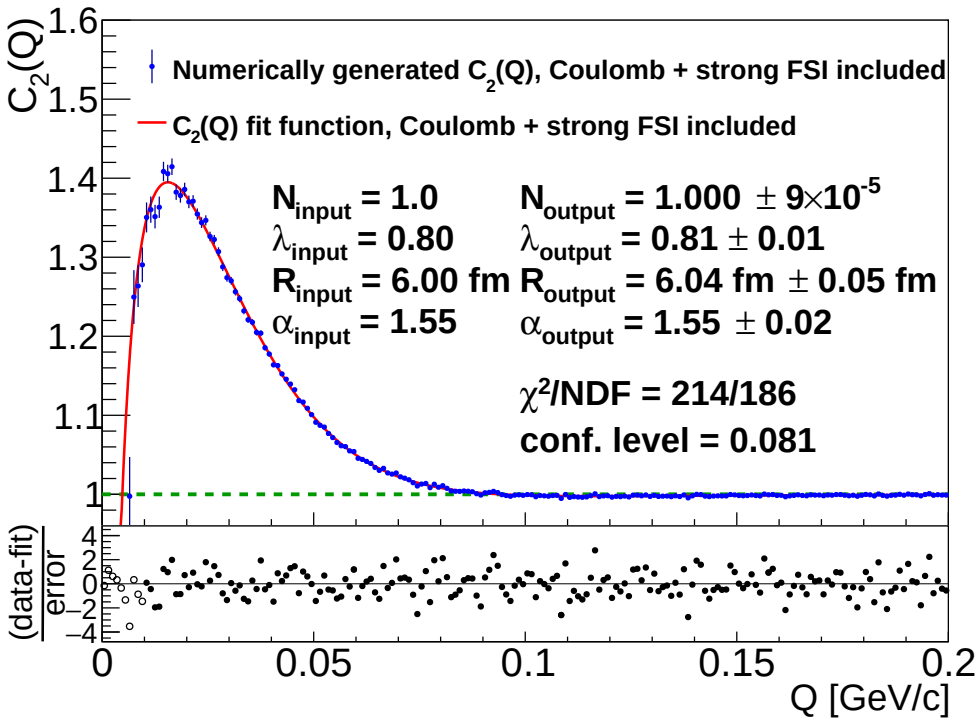

Figure 6.3: Numerically generated two-pion correlation histogram, fitted with the corresponding functional form to test the validity of the fitting method. The output parameter values are within errors the same as the input.

considerable amount resulting in statistically unacceptable fits. An example for this can be seen on panel (b) of Fig. 6.4. One can also observe that on the subplot showing the values of the difference of the fit from the data divided by the uncertainty of the datapoint, a characteristic oscillating structure appears.

6.2.2 *Quantitative estimation of the strong FSI effect*

To give a better estimation on the change in the parameter values when fitting data containing strong interaction with a function containing only the Coulomb effect, I generated and fitted histograms similar to panel (b) of Fig. 6.4, spanning a wide range in parameter space of $\lambda_{\text{input}} = 0.3 - 1.0$, R_{input} = 3 fm - 9 fm and $\alpha_{\text{input}} = 1.0 - 2.0$. For each fit parameter, I plotted the output versus the input values. The plotted output values represent a weighted average of output values coming from the same input for the given parameter but different inputs for the other two parameters. The results of this investigation can be seen on Fig. 6.5, panel (a)–(c).

Based on these results I can determine the effect of including strong interactions in correlation function fits. Note that here I consider the case of "Coulomb-only" fitting as the baseline, and investigate the change of the Lévy fit parameters when including the strong interaction as well (the effect on the calculated correlation functions is the opposite to this). I find this useful as this tells us the error stemming from not including the strong interaction. By fitting data containing the Coulomb and strong final state interactions with a functional form describing only the Coulomb part, it seems that the correlation strength λ is underestimated by about 5% on average. The effect on the Lévy-scale parameter R is negligible at small values of it, while at higher values of R (up to about 9 fm) it is also slightly underestimated, by about 1%. The Lévy exponent α is overestimated by about 1-2%.

The estimations given here for the change in parameter values are by no means universal, they also depend on other factors such as numerical precision of the integral calculations, fit limits (Q_{min} dependence), the precision of the generated data (see for example the difference between Fig. 6.4 (a) and (b)), or the parametrization of the strong phase-shift. The important conclusion from our investigations is that if the data is precise enough (which could be the case for recent measurements at RHIC or LHC), one most likely has to incorporate the strong interaction in the fits to achieve a statistically acceptable description of pion-pion correlation functions.

6.3 SUMMARY AND CONCLUSIONS

In this Chapter I presented a detailed calculation of the shape of two-pion HBT correlation functions with the assumption of Lévy stable source functions, and taking into account the Coulomb and strong final state interactions. Strong final state interactions were treated in the s-wave approximation.

A numerical calculation of the correlation function revealed that the strong final state interaction can have a non-negligible effect on the shape of pion-pion correlation function. As a first step towards the more thorough evaluation, I presented a quantitative estimation of the magnitude of this effect. As a general trend, I can ascertain that fits without the strong interaction effect typically underestimate the

strength of the correlation, λ, and the Lévy scale R, while overestimate the Lévy exponent α. The magnitudes of these deviations are generally found to be no more than a few percent.

However, typical fits to measured correlation functions can become statistically unacceptable if the strong interaction is neglected. If one aims at a high level of precision (feasible in case of precise enough data coming from today's typical heavy ion experiments), one can arrive at refined conclusions about the source function if the small deviations (caused by the strong interaction) are treated properly in the fitting procedure.

As an outlook, I note that there is some room for improvement in the methodology of the numerical calculations presented here. Such improvements might yield so precise predictions that it becomes possible to actually give constraints on like-sign pion strong interactions (i.e. scattering lengths) based on HBT correlation measurements in heavy ion collisions, a topic long thought to be interesting to investigate [189]. I look forward to a concrete experimental test of the predictions made here about the shape of the correlation function that gets influenced by strong final state interaction.

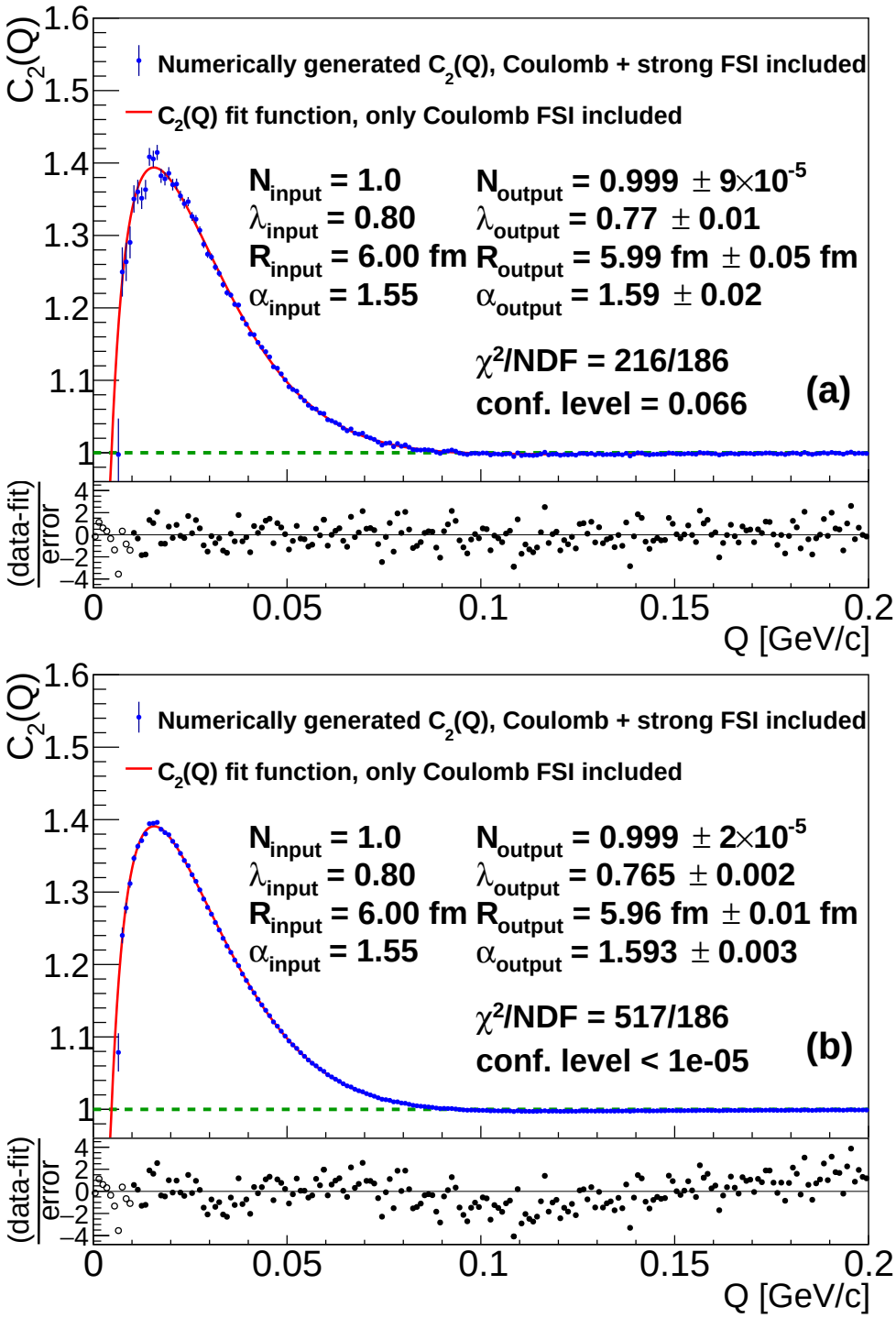

Figure 6.4: Numerically generated two-pion correlation histogram incorporating Coulomb and strong final state interactions, fitted with a functional form containing only the Coulomb effect. When the generated data is less precise (a), the fit is statistically acceptable, but the output parameter values differ from the input. The difference is even more pronounced when the generated data is more precise (b), in this example the value of λ decreased by about 4%, the value of R decreased by about 1%, and the value of α increased by about 3%. It is also important to note that in this case the χ^2/NDF value is not acceptable anymore.

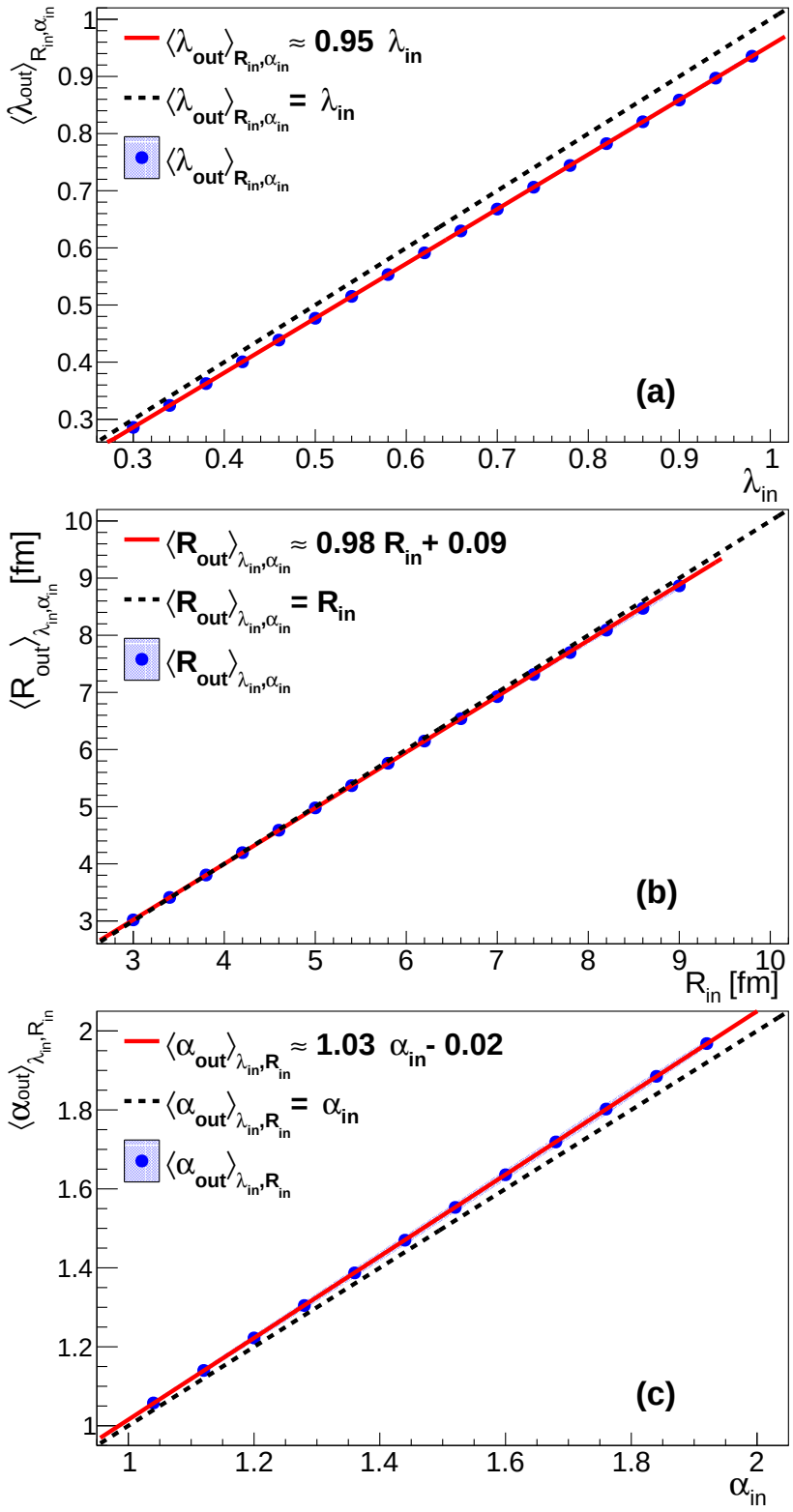

Figure 6.5: Output versus input values from fits similar to Fig. 6.4.(b). The correlation strength λ is shown on panel (a), the Lévy scale parameter R is shown on panel (b) and the Lévy exponent α is shown on panel (c). The identity line is shown with a dashed line, while a linear fit is shown with a continuous line. For a given input parameter, the weighted average of the output values are shown with markers, and the standard deviation is shown with a band.

7

EVENT-BY-EVENT INVESTIGATION OF THE TWO-PARTICLE SOURCE FUNCTION IN HEAVY-ION COLLISIONS WITH EPOS

As it was discussed before, a long-standing goal of high-energy nuclear physics has been to understand and explore the space-time geometry of the particle emitting source created in heavy-ion collisions [130]. One main observable that is of great interest is the two-particle source function, sometimes also called spatial correlation function or pair-separation distribution. Detailed investigation of this quantity is important for a multitude of reasons (connected to hydrodynamic expansion, critical behavior, etc.), however, it is not something that is easy to reconstruct experimentally. In Chapter 3 I introduced a sub-field of high-energy nuclear- and particle-physics called femtoscopy, which deals with such measurements of lengths and time intervals on the femtometer (fm) scale [107]. Since it was shown by G. Goldhaber et al. that intensity correlations of identical pions can be used to gain information about the pair-source function [119, 120], femtoscopy has propelled to the forefront of investigations, and today it is still one of the most extensively studied field of high-energy physics. Besides the ample experimental studies, phenomenological investigations also placed great emphasis on describing the shape of the source function. Hydrodynamical model calculations suggest [124, 139, 140, 190–192] that the source-shape is Gaussian, and this was adopted by many measurements as well [121, 159].

Source imaging studies [142, 160] on the other hand (as discussed in Section 3.2.3) suggest that the two-particle source function of pions has a long-range component, obeying a power-law behavior. It was also shown recently by various experimental measurements, that a generalization of the Gaussian source shape, the Lévy distribution can provide a much more suitable description of the observed sources [9, 144]. These kind of source shapes arise in many different scenarios [193] such as anomalous diffusion [143], jet fragmentation [146],

critical behavior [147], or resonance decays. It has been shown that even averaging over many events with different sizes can contribute to the appearance of a power-law component [148, 149]. In order to have a better understanding of the underlying processes behind the experimental results, more effort is needed from the phenomenology side. Among the important tools for such investigations are the event-generators that encompass different theoretical and phenomenological methods to model nuclear reactions. One of such event generators is the EPOS model [194]—the **E**nergy conserving quantum mechanical multiple scattering approach, based on **P**artons (parton ladders), **O**ff-shell remnants, and **S**plitting of parton ladders. In this chapter I present a detailed event-by-event analysis of the two-pion source distribution, in $\sqrt{s_{NN}} = 200$ GeV Au+Au collisions generated by EPOS. The event-by-event nature of the analysis helps in deciding if the role of event averaging is crucial in the apparent non-Gaussian but Lévy nature of the observed sources.

7.1 THE EPOS MODEL

EPOS, **E**nergy conserving quantum mechanical multiple scattering approach, based on **P**artons (parton ladders), **O**ff-shell remnants, and **S**aturation of parton ladders, is a phenomenological model based on Monte Carlo techniques. It opens up the possibility of investigating various phenomena and observables such as particle production, momentum distributions or flow correlations, providing a better understanding of the evolution of the system created in elementary (proton-proton) collisions and also during complex reactions involving heavy-ions. The theoretical framework included in the model provides a coherent description of the space-time expansion of matter based on a precise spectrum of studies of both elementary processes such as electron-positron annihilation or lepton-nucleon scattering and more compound collisions of protons or nuclei. The model was designed to describe processes appearing in collisions at $\mu_B \approx 0$, at very high (top RHIC or LHC) energies and for various systems, such as Au+Au, Pb+Pb or p+p.

The EPOS model consists of several phases of evolution, all of which are discussed in this Section:

- initial stage (based on the Parton Gribov–Regge theory);
- core/corona division;
- hydrodynamical evolution;
- hadronization;
- hadron rescattering;
- resonance decays.

7.1.1 *Initial Stage of the Evolution*

In the theoretical framework of the model the crucial element is the sophisticated treatment of both the hadron-hadron scattering and the initial stage of the collisions at ultra-relativistic energies. It is highly relevant in the understanding of possible parton–hadron phase transitions. In EPOS, a merged approach of the Gribov–Regge Theory (GRT) and the eikonalised parton model is utilised to provide proper treatment of the first interactions happening just after a collision. This approach satisfies conservation laws, and treats the subsequent Pomerons (interactions) equally (as opposed to other multiple interaction approaches, for example, Pythia, where the first interaction is not treated exactly the same way as the others) [195].

The formalism used for the calculation of the cross-sections is the same as the one used for calculating particle production. It is based on the Feynman diagrams of the QCD-inspired effective field theory and provides energy conservation. The nucleons are divided into a certain number of "constituents" carrying the incident momentum fraction. The fractions sum to unity in order to ensure momentum conservation. A nucleon is called a *spectator* if it is not part of the interaction region of the colliding nuclei. If a nucleon is not a spectator, then its constituents can either be *participants* taking part in the elementary interactions with constituents from the opposite side, or a *remnant*, which although part of the interaction region, does not take part in the elementary interactions. This is illustrated in Figure 7.1.

The particle production is based on the String Model approach [197, 198]. The parton ladders are recognized as a quasi-longitudinal color field (elementary flux tubes) and are treated as classical strings [194]. The intermediate gluons introduce the transverse motion into the *kinky string* evolution. The schematic picture of the flux tube with the transverse kink is shown on Figure 7.2.

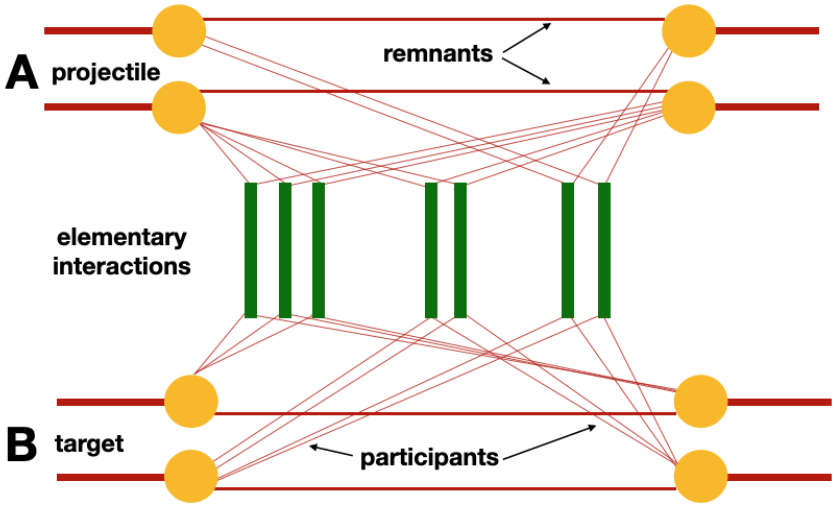

Figure 7.1: An illustration of the nucleon-nucleon rescattering with two projectiles A and two targets B. The splitting between participants and remnants shows the momentum sharing between constituents ensuring conservation of the given variable [196].

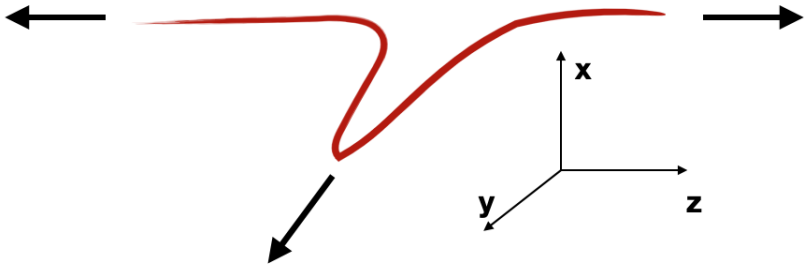

Figure 7.2: The flux tube with the kink. The flux tube is mainly longitudinal but the kink part of the string moves transversely, here in the y-direction [196].

7.1.2 *Core-Corona Approach*

If the density of the strings is very high, they cannot decay independently. This situation is characteristic for heavy-ion collisions and high-multiplicity pp collisions. Henceforth, in EPOS a dynamical process of the division of the strings segments into *core* and *corona* is introduced [194, 199, 200].

The core-corona division is based on the abilities of a given string segment to leave the "bulk matter". The transverse momentum of the element and the local string density are considered as criteria for the division. If the string segment belongs to a very dense area, it will not escape but will contribute to the *core*, which will be governed in

the next step by the hydrodynamical evolution. When the segment originates from the part of the string close to the kink, it is characterized by high transverse momenta. It escapes the bulk matter and will contribute to the *corona*. It consequently will show up as a hadron in a jet. There is also a possibility that the string segment is close to the surface of the dense part of the medium, and its momentum is high enough to leave it; then it also becomes a *corona* particle.

7.1.3 *Viscous Hydrodynamical Evolution, Event-by-Event Treatment and EoS*

In EPOS a 3D+1 viscous hydrodynamics approach is applied, called vHLLE (viscous relativistic Harten-Lax-van Leer-Einfeld Riemann solver-based algorithm). In the simulations, the separate treatment of individual events is highly important—smooth initial conditions for all events are not applied. The event-by-event approach in hydrodynamical evolution is based on the random flux tube initial conditions [194]. It has a relevant impact on the final observables such as spectra or various harmonics of flow. The viscous hydrodynamics uses Equation of State X3F ("cross-over" and "3 flavor conservation") which is compatible with lattice QCD data from Ref. [201]. It corresponds to $\mu_B = 0$ MeV, hence this feature limits the applicability of the model to describe the region of the QCD phase diagram characterized by finite baryon density [194].

7.1.4 *Hadronization and Hadronic Cascades*

The expanding medium in the processes of hydrodynamical evolution reaching the given freeze-out condition is transformed into the particle spectra. In EPOS 3, the criterion characterizing the hadronization hypersurface is that the energy density equals 0.57 GeV/fm^3. EPOS 3 furthermore utilizes the Cooper–Frye formula [202] when determining distributions. The final part of the simulation uses a so-called *hadronic afterburner*, based on UrQMD [203, 204]. The hadronic scattering has a significant impact on the final observables [205].

7.2 THE TWO-PARTICLE SOURCE FUNCTION

In this section I reiterate some of the basic definitions and properties of the two-particle source function. The pair source distribution $D(r, K)$ is defined as the auto-correlation of the single particle phase-space density $S(x, p)$, as shown in Equation 3.16. The $D(r, K)$ distribution is the quantity that can be reconstructed indirectly from femtoscopic momentum correlation measurements, and experiments usually investigate the source-parameters that describe the shape of this distribution, as discussed in Chapter 4.

It was recently shown by different experiments that for pions this pair-source exhibits a power-law behavior, and can be described with a Lévy-stable distribution [9, 144]. In case of spherical symmetry, the symmetric, centered stable distribution $\mathcal{L}(\boldsymbol{r}; \alpha, R)$ is defined in Equation 3.27. In this definition the temporal dimension is removed from the dependence, made possible by the mass-shell condition, as detailed in Section 3.3.1. The two important parameters that describe such a distribution are the Lévy-scale parameter R and the Lévy-exponent α. One can think of the latter as the parameter that is responsible for "how far" the distribution is from the Gaussian. In the $\alpha = 2$ case $\mathcal{L}(\boldsymbol{r}; \alpha, R)$ is identical to a Gaussian distribution, while in case of $\alpha < 2$ it exhibits a power-law behavior. An illustration of the shape of such distributions can be seen on Figure 3.3. Since this distribution retains the same α exponent under convolution of random variables, if the single-particle source densities have a Lévy-shape then it follows that the two-particle source will also have such a shape, only the scale-parameter will be different, as shown in Equation 3.29.

There are already multiple experimental measurements for the Lévy source parameters. Most notably the PHENIX experiment published results (discussed in Chapter 4) for 0–30% centrality, $\sqrt{s_{NN}} = 200$ GeV Au+Au collisions, in the m_T region of 0.23 GeV/c^2 to 0.87 GeV/c^2. They found the α parameter to be very slightly dependent on m_T, with an average value around 1.2. The NA61/SHINE experiment also has measured the Lévy-exponent in 150 A GeV Be+Be collisions, and obtained average α values of around 1.2 [144].

7.3 DETAILS OF THE ANALYSIS

For the analysis presented below I used $\sqrt{s_{NN}}$ = 200 GeV Au+Au events generated by EPOS359. Using like-sign pion pairs, I measured the one-dimensional pair-source distribution in the longitudinal co-moving system (LCMS). The LCMS pair-separation vector can be expressed in lab-frame single-particle coordinates as

$$\boldsymbol{r}_{LCMS} = \left(x_1 - x_2,\ y_1 - y_2,\ z_1 - z_2 - \frac{\beta(t_1 - t_2)}{\sqrt{1-\beta^2}} \right),$$
$$\text{where } \beta = \frac{p_{z,1}+p_{z,2}}{E_1+E_2}. \tag{7.103}$$

Using this variable, one can construct the spatio-temporal distance distribution
$D(\boldsymbol{r}_{LCMS}, t)$. After angle- and time-integration one can obtain the one-dimensional distance distribution as:

$$D(r_{LCMS}) = \int d\Omega_{LCMS} dt D(\boldsymbol{r}_{LCMS}, t), \tag{7.104}$$

where the K dependence indicated in Equation (3.16) is now suppressed. Note that the dependence on the lab-frame time-coordinate disappears after the time integral of Equation (7.104), since I only keep the dependence on r_{LCMS}, the final variable. In fact when analyzing the EPOS output, I only calculate the number of pairs in a given r_{LCMS} bin, hence dependence on all other coordinates is naturally integrated out. When selecting pions I used the single-particle rapidity and transverse momentum requirements of $|\eta| < 1$ and $0.2\ \text{GeV}/c < p_T < 1.0\ \text{GeV}/c$. For each individual event I constructed the $D(r_{LCMS})$ distribution for 5 different average transverse momentum k_T classes in equal bins ranging from 0.2 to 0.4 GeV/c. Note that $k_T = 0.5\sqrt{K_x^2 + K_y^2}$ is the transverse component of K used in Equation (3.16). I chose this k_T region to be around the peak of the pair k_T distribution to have adequate statistics (number of pairs) in the individual k_T bins. To investigate centrality dependence as well, I separated the measurements to the centrality classes of 0–5%, 5–10%, 10–20%, 20–30%. In total I used 63,000 EPOS events, 10,500 for the first two centrality classes and 21,000 for the rest.

As mentioned before, EPOS has different stages of evolution including hydrodynamic expansion and hadronic rescattering. In order to identify the effect of the different stages on the shape of the pair-source distribution, as well as the contribution from the resonance decay products, I separated the investigation to four different cases as follows:

(a) CORE with only primordial pions;

(b) CORE with primordial + decay pions;

(c) CORE+CORONA+UrQMD with only primordial pions;

(d) CORE+CORONA+UrQMD with primordial + decay pions,

where primordial pions include pions coming from the thermal medium, that is, primordial pions are those that are not decay products. For each single event I fitted a Lévy distribution to the constructed $D(r_{LCMS})$ distribution within the range of 2 fm to 100 fm. The fit was considered good if the confidence level calculated from the χ^2 and NDF values was greater than 0.1%. An example of such fits for the four different cases can be seen on Figure 7.3.

In case (a) I found that the events exhibit sharp cutoff features and mostly can be fitted well with a Gaussian. In case (b) the inclusion of the decay product pions results in power-law like structures, appearing at different regions in r_{LCMS}. The shape of the events can be very different depending on the number (and origin) of decay pions in the sample. Due to the increased fluctuations and different event shapes the event-by-event extraction of the source parameters could not be done in the previous two cases. The fit settings would have to be fine-tuned for each event separately for this to work, which makes it impossible to do for thousands of events. In case (c) and (d) however, distinct non-Gaussian structures (power-law tails) are present in all events, shapes can be described by Lévy distributions in a statistically acceptable manner, and the extraction of the event-by-event source parameters is feasible. Furthermore, their distribution in the event sample can also be determined.

An example for such a distribution can be seen on Figure 7.4. In this example the distribution was reconstructed from fitting 21,000 events, out of which 18,460 fits were successful for case (c) and 18,768 for case

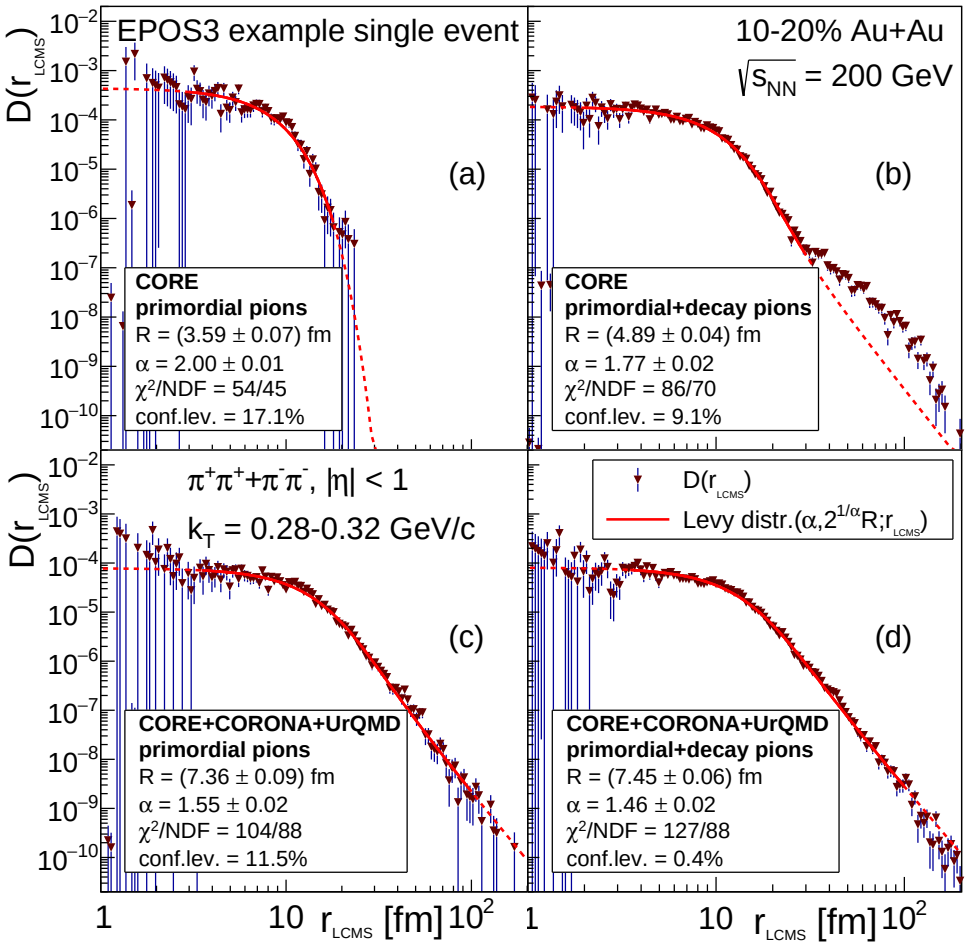

Figure 7.3: EPOS3 example single event fits for 10–20% Au+Au collisions at $\sqrt{s_{NN}} = 200$ GeV. The average transverse momentum k_T of the pion pairs is within the range of 0.28 GeV/c to 0.32 GeV/c. The measured D(r_{LCMS}) pion pair source distributions are denoted with downward-pointing triangles, and the fitted Lévy distributions are plotted with a red line (continuous in the fit region, dashed outside). The four panels from left to right, top to bottom are (**a**) CORE with only primordial pions, (**b**) CORE with primordial + decay pions, (**c**) CORE + CORONA + UrQMD with only primordial pions, and (**d**) CORE + CORONA + UrQMD with primordial + decay pions.

(d) according to the confidence level criteria. Note that the distribution of source parameters was quite the same for non-acceptable fits as well; however, those do not necessarily represent the acquired source distributions, hence they were omitted from the further calculations. As mentioned before, I measured these two-dimensional R vs. α distributions for four different centrality classes, and five different k_T regions. From these I can extract the mean and standard deviation values, and investigate their centrality and k_T dependence. There are multiple ways to determine the mean and standard deviation

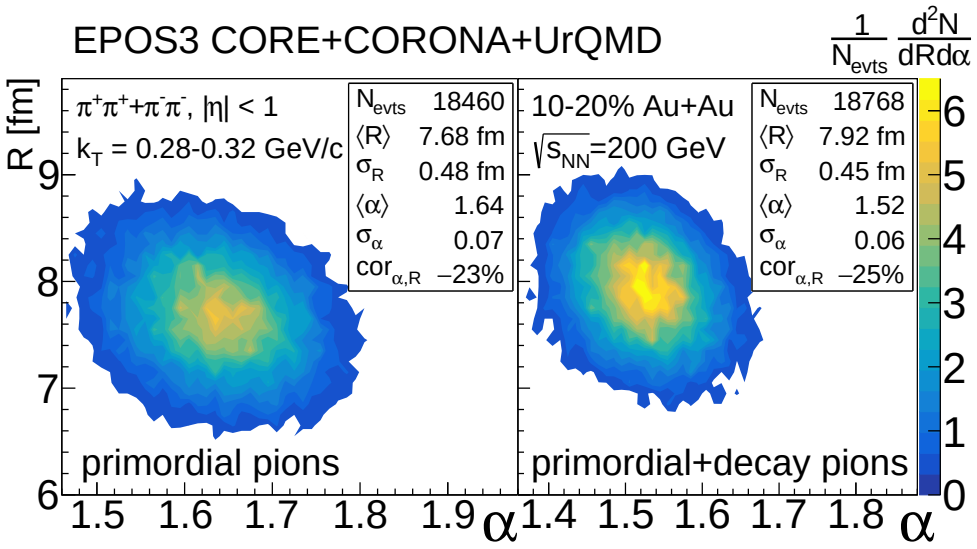

Figure 7.4: Example source parameter distributions for EPOS3 CORE+CORONA+UrQMD with only primordial pions (**left**) and with primordial and decay pions (**right**). The distribution was reconstructed from 10–20% centrality $\sqrt{s_{NN}} = 200$ GeV Au+Au events for pion pairs with an average transverse momentum k_T between 0.28 GeV/c and 0.32 GeV/c.

parameters—on one hand, one could do normal distribution fits to the obtained 2D histograms, and on the other hand, one can simply calculate the first and second momenta of the distributions. I checked both and since the results were quite similar, for the sake of simplicity I chose the latter one.

Let me reiterate the point here that I analyzed individual EPOS events, and determined the R and α parameters of the pair source distribution in those individual events. I saw Lévy-shaped distributions when I included hadronic scattering, with slightly different α parameter values when decay pions were also included (besides primordial pions).

7.4 RESULTS AND DISCUSSION

As described above, I performed fits to individual EPOS events from the final stage of EPOS (CORE+CORONA+UrQMD), and investigated averages of the resulting R and α parameters. I repeated this exercise for various centralities (0–5%, 5–10%, 10–20% and 20–30%) and k_T regions (five equal bins from 0.2 to 0.4 GeV/c). I analyzed two cases separately: first the case of using only primordial pions, and then a case where both primordial and decay pions were included in the

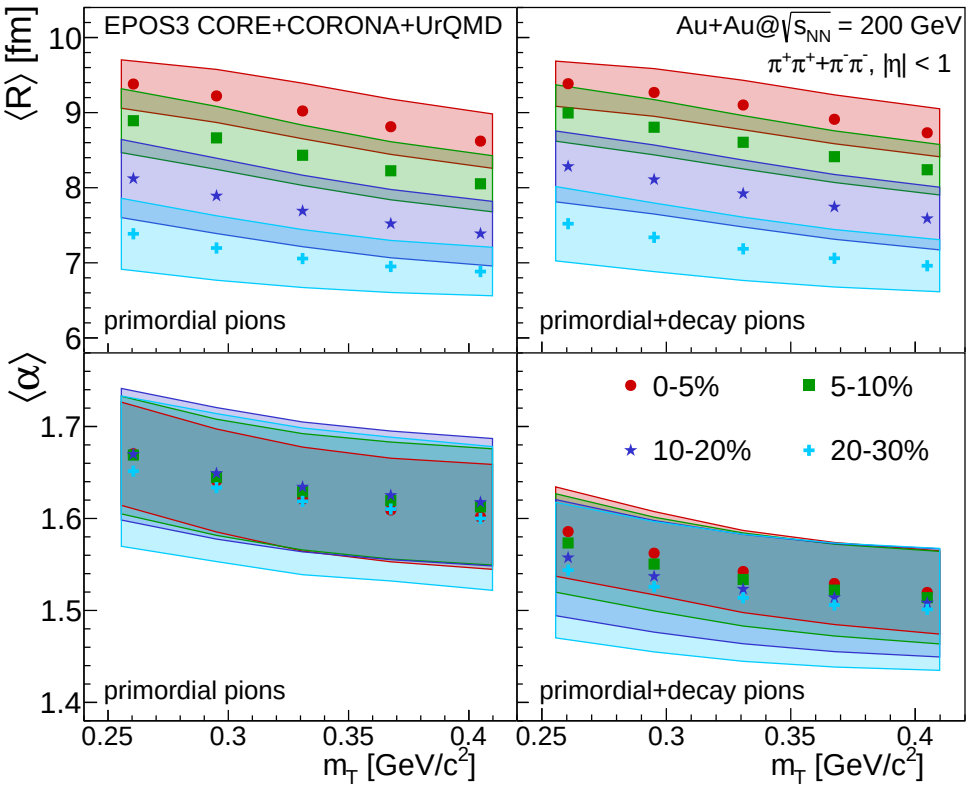

Figure 7.5: Mean R and α values vs. average transverse mass m_T for four different centrality classes (0–5%, 5–10%, 10–20%, 20–30%), in case of $\sqrt{s_{NN}} = 200$ GeV Au+Au collisions generated by EPOS3. The left column corresponds to the case of using primordial pions only, while the right column corresponds to the case of including both primordial and decay pions in the sample. The mean values are plotted with different filled markers. The corresponding colored boxes are representing the standard deviation values. The data from this Figure is listed in Tables B.1-B.4.

sample. Results for the mean R and α values versus $m_T = \sqrt{m^2 + k_T^2}$ are shown in Figure 7.5.

One can observe a clear decreasing trend in R with both m_T and centrality, for both the case of primordial pions, as well as the case where decays were also included. This trend with m_T is similar to the observed $R^2_{Gauss} \propto m_T$ trend observed universally across collision centrality, particle type, colliding energy, and colliding system size [121, 122], even though it is based on Gaussian source radii. The decrease of R with increasing centrality shows the relation of the Lévy-scale to the initial fireball size. One can also observe that R is only weakly affected by the inclusion of decay pions; the values are slightly higher in the latter case.

The Lévy-stability index α shows less prominent centrality dependence, although a small decrease for more peripheral events is visible in case I include decay pions as well. This feature, that is, the centrality dependence of α, was not yet investigated in experimental publications (with the exception of preliminary data in Ref. [171]). One may also observe a weak decrease with m_T similarly to what was observed in Ref. [9]. Furthermore it is clearly visible that when decay pions are also included, the α parameter decreases. This is expected as decay pions produce an even stronger tail, creating a smaller α value.

Concrete values of R can be compared to measured values from Ref. [9]. There R values of 7–8 fm were measured for the 0–30% centrality class and the m_T = 0.25–0.45 GeV/c^2 window. Our calculation yields similar values in the 10–20% and 20–30% centrality class. In Ref. [9], however, α values around 1.2 with a weak m_T dependent decrease were found. The trend in m_T is similar in our analysis, but the magnitude of the α values is somewhat different. The reasons for this could be multifold, they can range from the unavoidable event averaging present in the experiment to initial or final state effects not present in our simulations. The exploration of this difference is beyond the scope of present analysis.

Note that the filled bands on both plots indicate the standard deviation of the R and α distributions over the investigated event sample (let me remind the reader that I investigate and fit pair source distributions in individual events). The statistical uncertainty of these data points is basically negligible, due to the large number of events this average was performed over. This means that the trends observed in Figure 7.5 and discussed above are true features of the EPOS event sample investigated in this analysis.

7.5 SUMMARY AND CONCLUSIONS

I investigated a sample of EPOS events individually, and using identical pion pairs I reconstructed the pair source function in every individual event. In the case when only primordial pions were analyzed before hadronic scattering, a Gaussian shape was observed. However, when decay pions were also included, already power-law like structures appeared, and after the inclusion of hadronic scatterings (via UrQMD), Lévy-shaped pair distributions arose in the

individual events. It is hence clear that it is not the event averaging that creates the non-Gaussian features in the pair distributions (and the arising correlation functions in femtoscopical measurements).

Subsequently, using the final stage of EPOS events (CORE + CORONA + UrQMD), I analyzed the event sample mean of the event-by-event Lévy-scale R and Lévy-index α values for the case of using only primordial pions and the case of including both primordial and decay pions. I observed clear trends as a function of m_T and centrality for both cases. These observations show that in a realistic hydrodynamics-based simulation deviations from the Gaussian source shape appear when one includes hadronic scattering and decays. The values and trends of R are compatible with experimentally measured values, although I did not perform a detailed data comparison here. The weak decrease of α with m_T is similar to what was observed experimentally, but the values of α are somewhat larger than measured values.

In the future I plan to utilize similar techniques to explore the dependence of these results on particle species as well. Further investigations might also include expanding the analysis to multiple dimensions, different collision energies, as well as reconstructing femtoscopical correlation functions.

Finally let me note that one of the important conclusions of the analysis is that the Lévy-shaped source assumption provides an acceptable description of the pion pair-source in EPOS3.

Part IV

SUMMARY, CONCLUSIONS, AND OUTLOOK

Now, if there is any unifier to this collection of human beings we call scientists, it is the pride and reverence with which each of us adds our contribution to that intellectual edifice: our science.

— Leon M. Lederman [12]

8

SUMMARY OF EXPERIMENTAL AND PHENOMENOLOGICAL RESULTS

The goal of high-energy heavy-ion physics is to observe and investigate the properties of the Quark-Gluon-Plasma, a state of matter that was present in the first microseconds of the Universe. During my research, I investigated femtoscopic correlations, which aim to unravel the space-time structure of the particle-emitting source (the QGP) created in high-energy heavy-ion collisions. In Chapter 1 I introduced the experiments and theoretical ideas that led to the discovery of the strongly interacting Quark-Gluon-Plasma, and in Chapter 2 I discussed in detail the PHENIX and STAR detector systems. In Chapter 3 I presented and extensive review of femtoscopic correlations, with special emphasis on Lévy-type source functions. In that chapter I also discussed in detail the experimental techniques of correlation measurements.

After a comprehensive introduction, in Chapter 4 I moved on to my experimental results. I started my experimental work by measuring Bose-Einstein correlations of pion pairs on a set of Au+Au collision data recorded by the PHENIX experiment at the Relativistic Heavy Ion Collider (RHIC). In case of $\sqrt{s_{NN}} = 62$ GeV I measured the correlation functions in 8 average transverse mass (m_T), and 4 centrality classes, while for $\sqrt{s_{NN}} = 39$ GeV I used 6 m_T and 2 centrality classes. The results of my data analysis showed that the two-particle source function of pions exhibits a power-law behavior, and the Lévy distribution can provide an adequate description of the source shape in all investigated ranges of average transverse mass, centrality and center-of-mass collision energy. I measured furthermore the m_T and centrality integrated excitation function of the Lévy source parameters using 6 different center-of-mass collision energies from $\sqrt{s_{NN}} = 15$ GeV up to 200 GeV.

For each centrality class and every center of mass collision energies the correlation strength parameter shows a decrease at low average transverse mass, and a saturation at higher values of m_T. The Lévy

scale parameter shows a geometrical centrality dependence, and a decreasing trend with m_T compatible with a hydrodynamic scaling behavior. The Lévy exponent α is not constant as a function m_T but shows a weak dependence. It can be observed that its values are between 1 and 2 in all cases. Based on the preliminary results, the measured values of the Lévy exponent describing the power-law tail are thus far from both the Gaussian ($\alpha = 2$) case and the critical behavior ($\alpha \simeq 0.5$) for all of the investigated cases from $\sqrt{s_{NN}}$ = 15 GeV up to 200 GeV.

The limited statistics at lower energies raised the need to join the STAR experiment at RHIC, which provides a much more significant amount of data due to its larger acceptance. My preliminary results presented in Chapter 5 for $\sqrt{s_{NN}}$ = 200 GeV Au+Au collisions at the STAR experiment indicated that to be able to describe experimental data with such high precision, one may need to go beyond the previously utilized theoretical framework. Hence my focus shifted to phenomenological investigations.

To calculate the shape of Bose-Einstein correlation functions, one needs a proper description of the final-state interactions. Previous methods for pions only included the Coulomb interaction and assumed the contribution from the strong interaction to be negligible. My calculations presented in Chapter 6 involving both final-state interactions showed that although the inclusion of the strong interaction may only result in a few-percent difference in the source parameters, the quality of the fits to the experimentally measured correlation functions may improve significantly. This aids the interpretation of the extracted source parameters as more precise data may also be described adequately with help of this correction.

I investigated furthermore the shape of the two-particle source function in $\sqrt{s_{NN}}$ = 200 GeV Au+Au collisions simulated by the EPOS heavy-ion event generator. My event-by-event analysis introduced in Chapter 7 showed that Lévy source shapes arise in individual events when hadronic rescattering is turned on, and resonance decays also significantly contribute to the power-law behavior. Thus the reason for the appearance of such source shapes is not event-averaging. I also investigated the average-transverse mass and centrality dependence of the Lévy source parameters and found them comparable to experimental results, although for EPOS somewhat higher val-

ues of the Lévy exponent were observed. These results also indicate that the hydro-dynamical picture usually leading to Gaussian-like distributions might need some refinements as well.

New ideas and refinements on the experimental side together with the recent phenomenological developments can pave the way to an improved data analysis and the possibility to investigate the beam energy dependence of the Lévy source parameters with a much higher precision at STAR. This is outside the scope of this dissertation; Hopefully with a renewed effort on the experimental side we will find the answers to some of the still open questions.

9

FURTHER DEVELOPMENTS, OUTLOOK

The level of precision of today's data in high-energy physics makes it a daunting task to describe the observations in a statistically acceptable manner. Taking on this challenge is a step-by-step process; one can always try to improve on approximations in the theoretical description, as well as find new ways to refine the experimental data analysis process. In this "post-credit" chapter I discuss some of the most recent new developments and leave the reader with an outlook to possible future directions.

The EPOS analysis discussed in Chapter 7 suggested that even in a given average k_T and centrality bin, the event-by-event distribution of source shapes can be fairly wide, as shown on Figure 7.4. This will be even more pronounced in a wide centrality range (e.g. 0-30% used in the PHENIX and STAR analyses discussed in Part ii). It was not discussed in detail in Chapter 7, but the event average source functions are not perfectly Lévy, and although the event average fits result in quite similar parameter values, they are not statistically acceptable.

This prompted the idea of trying a similar approach as I utilized for the strong interaction analysis in Chapter 6, especially on Figure 6.4 (b). I numerically generated similar histograms, but this time for a huge parameter space, and took a weighted average of them. I used 1000 points in the $R \in [3\text{ fm}, 13\text{ fm}]$ range, and 1000 points in the $\alpha \in [1, 2]$ range. I defined a two-dimensional Gaussian similar to Figure 7.4, with mean and standard deviation parameters of $\langle R \rangle = 6$ fm, $\sigma_R = 1$ fm, $\langle \alpha \rangle = 1.5, \sigma_\alpha = 0.1$, and a correlation coefficient of $\text{cor}_{\alpha,R} = -25\%$. The values of this Gaussian were then used as weights when averaging the correlation functions in the 1000×1000 parameter space. I found that fits to these kind of weighted-average correlation functions are statistically not acceptable, and a very similar oscillating structure can be observed as in Figures 5.6 (b) and 6.4 (b).

To take this idea one step further, I combined three approaches. In the numerical calculation of the sample histogram I used the

previous weighted average method (with the same mean, standard deviation and correlation coefficient parameters), I turned on the effect of the strong interaction, and applied the PCMS correction as well (at $m_T = 0.395\ \mathrm{GeV}/c^2$) described in Equation 3.49. I then fitted the generated correlation function with the simple Coulomb and LCMS framework described in Equation 3.44. The fit is shown on Figure 9.1.

Even individually, all three of these approaches generate some kind of oscillating pattern in the (data-fit)/error auxiliary graph. What is quite remarkable and promising, however, is that the combination of these, shown in Figure 9.1, can quantitatively reproduce the pattern of Figure 5.6 (b). When choosing such an initial configuration for the numerical calculation that results in similar output parameters as the example fit of Figure 5.6 (b), the peaks and valleys of the auxiliary plots coincide with each other. This suggests, that using a fit function that contains the strong interaction and the PCMS correction described in Equation 3.49, furthermore using a finer centrality selection instead of a wide range might solve the previously encountered difficulties in the experimental fitting process.

With this promising outlook I conclude the present dissertation. The journey does not stop here; in the future I plan to reinvigorate the experimental data analysis at STAR, and continue research on the phenomenology side as well.

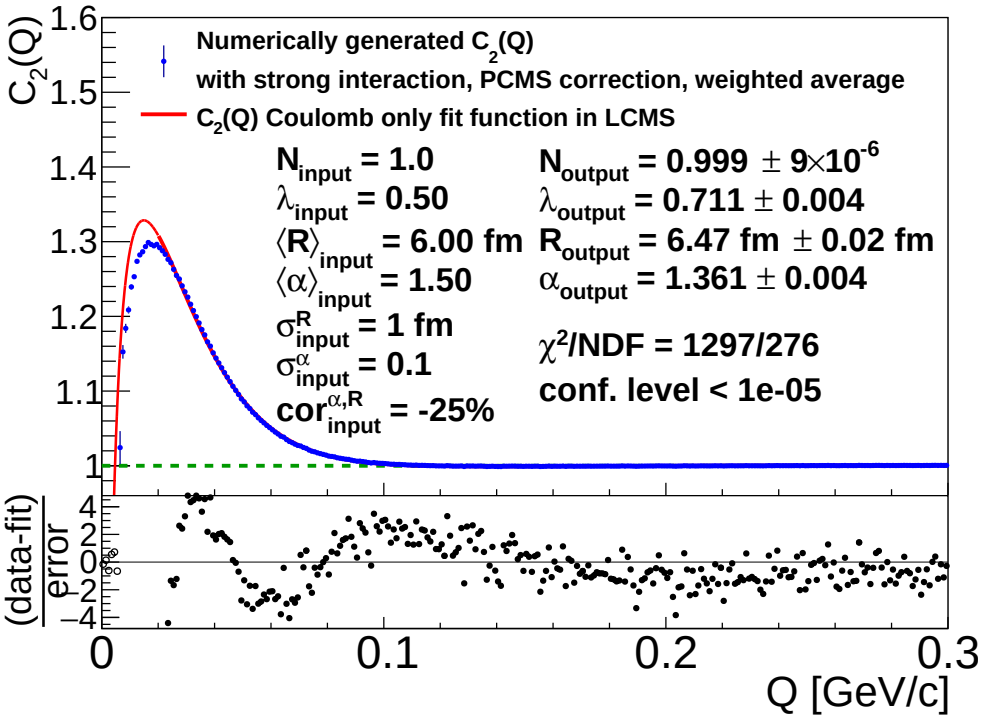

Figure 9.1: An average of numerically generated two-pion correlation histograms incorporating Coulomb and strong final state interactions and an approximate correction for the translation between PCMS and LCMS frames, weighted with a Gaussian distribution in the (α, R) parameter space. The fit to this weighted average was done in the relative momentum range of $Q \in [0.02, 0.3]$ GeV/c with a functional form containing only the Coulomb effect and no PCMS correction.

Part V

APPENDIX

Actually, doing science is a great deal of pleasure. Science is a tremendous career to follow. You have fun all the time, some blood, sweat and tears too, but it is ultimately rewarding.

— Leon M. Lederman

A

APPENDIX - ASSORTED SPECIAL FUNCTIONS

The following definitions, formulas and the explanation of the special functions that come by can be found in any standard textbook on quantum mechanical scattering theory (such as Ref. [182]), nevertheless I write them up to make the dissertation as self-contained as possible.

In the treatment of the quantum mechanical Coulomb problem, one encounters the *confluent hypergeometric equation*, a second order linear differential equation for the unknown $f(z)$ function, written as

$$zf''(z) + (b-z)f'(z) - af(z) = 0, \tag{A.105}$$

where a and b are two arbitrary parameters. A commonly used pair of linearly independent solutions are provided by the (renormalized) *confluent hypergeometric function* or Kummer's function:

$$\mathbf{F}(a,b,z) := \frac{F(a,b,z)}{\Gamma(b)}, \tag{A.106}$$

$$F(a,b,z) := \sum_{n=0}^{\infty} \frac{\Gamma(a+n)\Gamma(b)}{\Gamma(a)\Gamma(b+n)} \frac{z^n}{n!}, \tag{A.107}$$

which has the convenient property that it is analytic everywhere, especially at $z=0$; and the other solution is the so-called Tricomi's function, defined as

$$U(a,b,z) = \frac{\pi}{\sin(\pi b)} \left\{ \frac{\mathbf{F}(a,b,z)}{\Gamma(a+1-b)} - z^{1-b} \frac{\mathbf{F}(a+1-b,2-b,z)}{\Gamma(a)} \right\} \tag{A.108}$$

if b is not an integer, and as a limit $b \to n$ in the $b = n \in \mathbb{Z}$ integer case. The $U(a,b,z)$ function has a branch point at $z=0$, with the form written up having a branch cut along the $z \in \mathbb{R}^-$ negative real line.

However, it has the convenient property that it behaves asymptotically as

$$U(a,b,z) \sim z^{-a}, \tag{A.109}$$

and this is a property that is unique to it among the solutions of the confluent hypergeometric equation.

A „dual" pair of useful properties of the functions introduced is

$$\mathbf{F}(a,b,z) = e^z \mathbf{F}(b-a,b,-z), \tag{A.110}$$

$$U(a,b,z) = z^{1-b} U(a+1-b,2-b,z), \tag{A.111}$$

the former of which is verified by noting that both sides are analytic and fulfill the very same differential equation; the latter is a simple consequence of the definition. As seen above, $U(a,b,z)$ can be expressed from $\mathbf{F}(a,b,z)$; one can also derive the „inverse" formula:

$$\mathbf{F}(a,b,z) = \frac{e^{i\Pi_z a}}{\Gamma(b-a)} U(a,b,z) + \frac{e^{i\Pi_z (a-b)}}{\Gamma(a)} e^z U(b-a,b,-z), \tag{A.112}$$

with the Π_z notation introduced here as being π or $-\pi$, if $\arg z > 0$ or $\arg z < 0$, respectively.

Using l'Hospital's rule, the power series expression of the $U(a,b,z)$ function for integer b turns out to be

$$\begin{aligned} U(a,m+1,z) = \frac{(-1)^m}{\Gamma(a-m)} \Bigg\{ & -\log z \cdot \mathbf{F}(a,m+1,z) + \\ & + \sum_{s=1}^{m} \frac{(-1)^s}{z^s} \frac{(s-1)!}{(m-s)!} \frac{\Gamma(a-s)}{\Gamma(a)} + \sum_{s=0}^{\infty} \frac{z^s}{s!} \frac{1}{(m+s)!} \frac{\Gamma(a+s)}{\Gamma(a)} \times \\ & \times \left[\psi(s+1) - \psi(a+s) + \psi(s+m+1) \right] \Bigg\}, \qquad m \in \mathbb{N}_0^+. \end{aligned} \tag{A.113}$$

Here $\psi(s)$ is the digamma function defined as

$$\psi(s) \equiv \frac{\Gamma'(s)}{\Gamma(s)}. \tag{A.114}$$

Some convenient properties of it are:

$$\psi(a+n) = \psi(a) + \sum_{k=1}^{n} \frac{1}{a+k}, \tag{A.115}$$

$$\Rightarrow \qquad \psi(n+1) = -\gamma + \sum_{k=1}^{n} \frac{1}{k}, \tag{A.116}$$

where γ is the Euler constant:

$$\gamma = \lim_{n\to\infty} \left(\sum_{k=1}^{n} \frac{1}{k} - \ln n \right) = 0.577\ldots \tag{A.117}$$

A side note to the calculation of the $\mathbf{F}(a,b,z)$ and $U(a,b,z)$ functions: for the typical parameter values encountered in the work discussed in Chapter 6. (i.e. a and b on the order of unity), the power series in z can be used in a numerically satisfactory way only up to $|z| \approx 30$. For higher $|z|$ values, one rather uses the asymptotic expansion of $U(a,b,z)$:

$$U(a,a+1-\beta,z) = z^{-a}\left\{1 - \frac{a\beta}{1!z} + \frac{a(a+1)\,\beta(\beta+1)}{2!z^2} - \right.$$
$$\left. - \frac{a(a+1)(a+2)\,\beta(\beta+1)(\beta+2)}{3!z^3} + \ldots \right\}, \tag{A.118}$$

and for $\mathbf{F}(a,b,z)$, the expression of it that uses $U(a,b,z)$, see Eq. (A.112) above.

Regrettably, most numerical packages that are used for the computation of special functions do not have built-in methods for the calculation of the gamma function and the digamma function, $\Gamma(z)$ and $\psi(z)$ for arbitrary complex arguments, which was very much needed for the objectives discussed in Chapter 6. In my calculations, I used the Lanczos approximation [206] for both $\Gamma(z)$ and $\psi(z)$ when it was necessary. Usually, the Lanczos approximation is written up only for $\Gamma(z)$, however, it is easy to verify that the approximative formula is a well-behaved smooth function of z, so it can safely be used for the calculation of $\psi(z)$ as well, by taking the logarithmic derivative of it.

B

APPENDIX - DATA FROM THE EPOS ANALYSIS

The data from Figure 7.5. is listed in Tables B.1-B.4.

Table B.1: Mean and standard deviation values extracted from the source parameter distributions measured in EPOS3 Au+Au collisions at $\sqrt{s_{NN}} = 200$ GeV, in case of including only primordial pions. For the average transverse momentum k_T the range is indicated, while for the average transverse mass m_T the central value is given.

PRIMORDIAL PIONS						
Centr.	k_T **[GeV/c]**	m_T **[GeV/c^2]**	$\langle R \rangle$ **[fm]**	σ_R **[fm]**	$\langle \alpha \rangle$	σ_α
0–5%	0.20–0.24	0.261	9.381	0.322	1.670	0.056
	0.24–0.28	0.295	9.222	0.353	1.641	0.056
	0.28–0.32	0.331	9.021	0.370	1.621	0.056
	0.32–0.36	0.368	8.811	0.368	1.610	0.056
	0.36–0.40	0.405	8.619	0.361	1.603	0.056
5–10%	0.20–0.24	0.261	8.892	0.425	1.669	0.064
	0.24–0.28	0.295	8.663	0.419	1.645	0.063
	0.28–0.32	0.331	8.431	0.401	1.630	0.062
	0.32–0.36	0.368	8.223	0.385	1.621	0.062
	0.36–0.40	0.405	8.049	0.372	1.614	0.061
10–20%	0.20-0.24	0.261	8.121	0.521	1.671	0.071
	0.24–0.28	0.295	7.888	0.504	1.650	0.070
	0.28–0.32	0.331	7.683	0.480	1.636	0.068
	0.32–0.36	0.368	7.510	0.463	1.627	0.067
	0.36–0.40	0.405	7.370	0.444	1.620	0.066
20–30%	0.20-0.24	0.261	7.350	0.502	1.655	0.078
	0.24–0.28	0.295	7.135	0.471	1.639	0.076
	0.28–0.32	0.331	6.971	0.438	1.627	0.073
	0.32–0.36	0.368	6.844	0.407	1.619	0.072
	0.36–0.40	0.405	6.749	0.390	1.610	0.071

Table B.2: Mean and standard deviation values extracted from the source parameter distributions measured in EPOS3 Au+Au collisions at $\sqrt{s_{NN}} =$ 200 GeV, in case of including both primordial and decay pions. For the average transverse momentum k_T the range is indicated, while for the average transverse mass m_T the central value is given.

PRIMORDIAL + DECAY PIONS						
Centr.	k_T **[GeV/c]**	m_T **[GeV/c^2]**	$\langle R \rangle$ **[fm]**	σ_R **[fm]**	$\langle \alpha \rangle$	σ_α
0–5%	0.20–0.24	0.261	9.385	0.301	1.586	0.049
	0.24–0.28	0.295	9.269	0.318	1.562	0.045
	0.28–0.32	0.331	9.101	0.329	1.542	0.045
	0.32–0.36	0.368	8.911	0.326	1.529	0.045
	0.36–0.40	0.405	8.732	0.320	1.520	0.045
5–10%	0.20–0.24	0.261	8.995	0.375	1.573	0.054
	0.24–0.28	0.295	8.805	0.368	1.550	0.051
	0.28–0.32	0.331	8.605	0.355	1.534	0.051
	0.32–0.36	0.368	8.413	0.344	1.522	0.050
	0.36–0.40	0.405	8.240	0.336	1.514	0.050
10–20%	0.20–0.24	0.261	8.284	0.472	1.557	0.063
	0.24–0.28	0.295	8.109	0.460	1.537	0.061
	0.28–0.32	0.331	7.922	0.446	1.523	0.059
	0.32–0.36	0.368	7.744	0.433	1.514	0.059
	0.36–0.40	0.405	7.586	0.421	1.508	0.059
20–30%	0.20–0.24	0.261	7.500	0.517	1.544	0.074
	0.24–0.28	0.295	7.305	0.489	1.527	0.071
	0.28–0.32	0.331	7.132	0.465	1.516	0.070
	0.32–0.36	0.368	6.982	0.437	1.509	0.068
	0.36–0.40	0.405	6.856	0.411	1.505	0.067

Table B.3: Correlation coefficients and covariance values extracted from the source parameter distributions measured in EPOS3 Au+Au collisions at $\sqrt{s_{NN}} = 200$ GeV, in case of including only primordial pions. For the average transverse momentum k_T the range is indicated, while for the average transverse mass m_T the central value is given.

PRIMORDIAL PIONS				
Centrality	k_T **[GeV/c]**	m_T **[GeV/c^2]**	**cor(R, α)**	**cov(R, α) [fm]**
0–5%	0.20–0.24	0.261	−0.225	−0.004
	0.24–0.28	0.295	−0.273	−0.005
	0.28–0.32	0.331	−0.305	−0.006
	0.32–0.36	0.368	−0.319	−0.007
	0.36–0.40	0.405	−0.324	−0.007
5–10%	0.20–0.24	0.261	−0.328	−0.009
	0.24–0.28	0.295	−0.326	−0.009
	0.28–0.32	0.331	−0.329	−0.008
	0.32–0.36	0.368	−0.332	−0.008
	0.36–0.40	0.405	−0.316	−0.007
10–20%	0.20-0.24	0.261	−0.229	−0.008
	0.24–0.28	0.295	−0.235	−0.008
	0.28–0.32	0.331	−0.230	−0.008
	0.32–0.36	0.368	−0.224	−0.007
	0.36–0.40	0.405	−0.208	−0.006
20–30%	0.20-0.24	0.261	−0.142	−0.006
	0.24–0.28	0.295	−0.128	−0.005
	0.28–0.32	0.331	−0.137	−0.004
	0.32–0.36	0.368	−0.119	−0.003
	0.36–0.40	0.405	−0.114	−0.003

Table B.4: Correlation coefficients and covariance values extracted from the source parameter distributions measured in EPOS3 Au+Au collisions at $\sqrt{s_{NN}} = 200$ GeV, in case of including both primordial and decay pions. For the average transverse momentum k_T the range is indicated, while for the average transverse mass m_T the central value is given.

PRIMORDIAL + DECAY PIONS				
Centrality	k_T **[GeV/c]**	m_T **[GeV/c^2]**	**cor(R, α)**	**cov(R, α) [fm]**
0–5%	0.20–0.24	0.261	−0.287	−0.004
	0.24–0.28	0.295	−0.224	−0.003
	0.28–0.32	0.331	−0.265	−0.004
	0.32–0.36	0.368	−0.277	−0.004
	0.36–0.40	0.405	−0.309	−0.004
5–10%	0.20–0.24	0.261	−0.311	−0.006
	0.24–0.28	0.295	−0.292	−0.005
	0.28–0.32	0.331	−0.305	−0.005
	0.32–0.36	0.368	−0.309	−0.005
	0.36–0.40	0.405	−0.313	−0.005
10–20%	0.20–0.24	0.261	−0.236	−0.007
	0.24–0.28	0.295	−0.237	−0.007
	0.28–0.32	0.331	−0.250	−0.007
	0.32–0.36	0.368	−0.253	−0.006
	0.36–0.40	0.405	−0.263	−0.007
20–30%	0.20–0.24	0.261	−0.252	−0.010
	0.24–0.28	0.295	−0.256	−0.009
	0.28–0.32	0.331	−0.261	−0.008
	0.32–0.36	0.368	−0.256	−0.008
	0.36–0.40	0.405	−0.242	−0.007

BIBLIOGRAPHY

[1] Dániel Kincses. "Lévy analysis of HBT correlation functions in $\sqrt{s_{NN}} = 62$ GeV and 39 GeV Au+Au collisions at PHENIX." In: *Universe* 4.1 (2018), p. 11. DOI: 10.3390/universe4010011. arXiv: 1711.06891 [nucl-ex].

[2] Dániel Kincses, Márton I. Nagy, and Máté Csanád. "Coulomb and strong interactions in the final state of Hanbury-Brown–Twiss correlations for Lévy-type source functions." In: *Phys. Rev. C* 102.6 (2020), p. 064912. DOI: 10.1103/PhysRevC.102.064912. arXiv: 1912.01381 [hep-ph].

[3] Dániel Kincses, Maria Stefaniak, and Máté Csanád. "Event-by-event investigation of the two-particle source function in heavy-ion collisions with EPOS." In: *Entropy* 24 (2022), p. 308. DOI: 10.3390/e24030308. arXiv: 2201.07962 [hep-ph].

[4] Maria Stefaniak and Dániel Kincses. "Investigating the pion source function in heavy-ion collisions with the EPOS model." In: *Proc. SPIE Int. Soc. Opt. Eng.* 11581 (2020), p. 1158112. DOI: 10.1117/12.2580570. arXiv: 2008.03139 [hep-ph].

[5] Dániel Kincses. "Shape Analysis of HBT Correlations at STAR." In: *Phys. Part. Nucl.* 51.3 (2020), pp. 267–269. DOI: 10.1134/S106377962003017X. arXiv: 1911.05352 [nucl-ex].

[6] Dániel Kincses. "PHENIX results on collision energy dependent Levy HBT correlations from $\sqrt{s_{NN}}$ = 15 to 200 GeV." In: *Acta Phys. Polon. Supp.* 12 (2019), p. 445. DOI: 10.5506/APhysPolBSupp.12.445. arXiv: 1811.08311 [nucl-ex].

[7] Dániel Kincses. "PHENIX results on Lévy analysis of Bose-Einstein correlation functions." In: *Acta Phys. Polon. Supp.* 10 (2017), pp. 627–631. DOI: 10.5506/APhysPolBSupp.10.627. arXiv: 1610.05025 [nucl-ex].

[8] Dániel Kincses. "PHENIX results on Bose-Einstein correlation functions." In: *Acta Phys. Polon. Supp.* 9 (2016), p. 243. DOI: 10.5506/APhysPolBSupp.9.243. arXiv: 1602.04578 [nucl-ex].

[9] Andrew Adare et al., PHENIX Coll. "Lévy-stable two-pion Bose-Einstein correlations in $\sqrt{s_{NN}} = 200$ GeV Au+Au collisions." In: *Phys. Rev. C* 97.6 (2018), p. 064911. DOI: 10.1103/PhysRevC.97.064911. arXiv: 1709.05649 [nucl-ex].

[10] Steven G. Rogers. In: *Captain America: The Winter Soldier* (2014).

[11] Steven Weinberg. *The First Three Minutes*. Basic Books, 1977.

[12] L.M. Lederman and D. Teresi. *The God Particle: If the Universe is the Answer, what is the Question?* Mariner books. Houghton Mifflin, 2006. ISBN: 9780618711680. URL: https://books.google.hu/books?id=-v84Bp-LNNIC.

[13] H. Fritzsch, M. Gell-Mann, and H. Leutwyler. "Advantages of the Color Octet Gluon Picture." In: *Phys. Lett. B* 47 (1973), pp. 365–368. DOI: 10.1016/0370-2693(73)90625-4.

[14] Jeff Greensite. *An Introduction to the Confinement Problem*. Vol. 821. 2011. DOI: 10.1007/978-3-642-14382-3.

[15] David J. Gross and Frank Wilczek. "Ultraviolet Behavior of Nonabelian Gauge Theories." In: *Phys. Rev. Lett.* 30 (1973). Ed. by J. C. Taylor, pp. 1343–1346. DOI: 10.1103/PhysRevLett.30.1343.

[16] H. David Politzer. "Reliable Perturbative Results for Strong Interactions?" In: *Phys. Rev. Lett.* 30 (1973). Ed. by J. C. Taylor, pp. 1346–1349. DOI: 10.1103/PhysRevLett.30.1346.

[17] J. C. Collins and M. J. Perry. "Superdense Matter: Neutrons Or Asymptotically Free Quarks?" In: *Phys. Rev. Lett.* 34 (1975), p. 1353. DOI: 10.1103/PhysRevLett.34.1353.

[18] N. Cabibbo and G. Parisi. "Exponential Hadronic Spectrum and Quark Liberation." In: *Phys. Lett. B* 59 (1975), pp. 67–69. DOI: 10.1016/0370-2693(75)90158-6.

[19] Edward V. Shuryak. "Theory of Hadronic Plasma." In: *Sov. Phys. JETP* 47 (1978), pp. 212–219.

[20] Edward V. Shuryak. "Quark-Gluon Plasma and Hadronic Production of Leptons, Photons and Psions." In: *Phys. Lett. B* 78 (1978), p. 150. DOI: 10.1016/0370-2693(78)90370-2.

[21] Barry A. Freedman and Larry D. McLerran. "Fermions and Gauge Vector Mesons at Finite Temperature and Density. 3. The Ground State Energy of a Relativistic Quark Gas." In: *Phys. Rev. D* 16 (1977), p. 1169. DOI: 10.1103/PhysRevD.16.1169.

[22] Joseph I. Kapusta. "Quantum Chromodynamics at High Temperature." In: *Nucl. Phys. B* 148 (1979), pp. 461–498. DOI: 10.1016/0550-3213(79)90146-9.

[23] T. D. Lee. "Abnormal Nuclear States and Vacuum Excitations." In: *Rev. Mod. Phys.* 47 (1975). Ed. by G. Feinberg, pp. 267–275. DOI: 10.1103/RevModPhys.47.267.

[24] S. A. Chin. "Transition to Hot Quark Matter in Relativistic Heavy Ion Collision." In: *Phys. Lett. B* 78 (1978), pp. 552–555. DOI: 10.1016/0370-2693(78)90637-8.

[25] L. S. Schroeder. "High Energy Heavy Ion Collisions—A Possible Testing Ground for High Energy Interaction Models." In: *AIP Conf. Proc.* 23 (1975). Ed. by Hugh C. Carl E. Wolfe Carlson, pp. 301–313. DOI: 10.1063/1.2947435.

[26] J.B. Adams. *The alternating gradient proton sychrotron*. Tech. rep. Geneva: CERN, 1955. URL: https://cds.cern.ch/record/2262360.

[27] H. Hahn et al. "The RHIC design overview." In: *Nucl. Instrum. Meth. A* 499 (2003), pp. 245–263. DOI: 10.1016/S0168-9002(02)01938-1.

[28] M. Harrison, Stephen G. Peggs, and T. Roser. "The RHIC accelerator." In: *Ann. Rev. Nucl. Part. Sci.* 52 (2002), pp. 425–469. DOI: 10.1146/annurev.nucl.52.050102.090650.

[29] N. Angert et al. "CERN heavy ion facility design report." In: (Apr. 1993). DOI: 10.5170/CERN-1993-001.

[30] K. Adcox et al., PHENIX Coll. In: *Nucl.Phys.* A757 (2005), pp. 184–283. DOI: 10.1016/j.nuclphysa.2005.03.086. arXiv: nucl-ex/0410003 [nucl-ex].

[31] John Adams et al., STAR Coll. "Experimental and theoretical challenges in the search for the quark gluon plasma: The STAR Collaboration's critical assessment of the evidence from RHIC collisions." In: *Nucl. Phys. A* 757 (2005), pp. 102–183. DOI: 10.1016/j.nuclphysa.2005.03.085. arXiv: nucl-ex/0501009.

[32] I. Arsene et al., BRAHMS Coll. "Quark gluon plasma and color glass condensate at RHIC? The Perspective from the BRAHMS experiment." In: *Nucl. Phys. A* 757 (2005), pp. 1–27. DOI: 10.1016/j.nuclphysa.2005.02.130. arXiv: nucl-ex/0410020.

[33] B. B. Back et al., PHOBOS Coll. "The PHOBOS perspective on discoveries at RHIC." In: *Nucl. Phys. A* 757 (2005), pp. 28–101. DOI: 10.1016/j.nuclphysa.2005.03.084. arXiv: nucl-ex/0410022.

[34] K Aamodt et al., ALICE Coll. "Elliptic flow of charged particles in Pb-Pb collisions at 2.76 TeV." In: *Phys. Rev. Lett.* 105 (2010), p. 252302. DOI: 10.1103/PhysRevLett.105.252302. arXiv: 1011.3914 [nucl-ex].

[35] Georges Aad et al., ATLAS Coll. "Observation of a Centrality-Dependent Dijet Asymmetry in Lead-Lead Collisions at $\sqrt{s_{NN}} =$ 2.77 TeV with the ATLAS Detector at the LHC." In: *Phys. Rev. Lett.* 105 (2010), p. 252303. DOI: 10.1103/PhysRevLett.105.252303. arXiv: 1011.6182 [hep-ex].

[36] K Aamodt et al., ALICE Coll. "Charged-particle multiplicity density at mid-rapidity in central Pb-Pb collisions at $\sqrt{s_{NN}} =$ 2.76 TeV." In: *Phys. Rev. Lett.* 105 (2010), p. 252301. DOI: 10.1103/PhysRevLett.105.252301. arXiv: 1011.3916 [nucl-ex].

[37] Peter Braun-Munzinger, Volker Koch, Thomas Schäfer, and Johanna Stachel. "Properties of hot and dense matter from relativistic heavy ion collisions." In: *Phys. Rept.* 621 (2016), pp. 76–126. DOI: 10.1016/j.physrep.2015.12.003. arXiv: 1510.00442 [nucl-th].

[38] Michael L. Miller, Klaus Reygers, Stephen J. Sanders, and Peter Steinberg. "Glauber modeling in high energy nuclear collisions." In: *Ann. Rev. Nucl. Part. Sci.* 57 (2007), pp. 205–243. DOI: 10.1146/annurev.nucl.57.090506.123020. arXiv: nucl-ex/0701025.

[39] S. S. Adler et al., PHENIX Coll. "Centrality dependence of direct photon production in $\sqrt{s_{NN}}$ = 200 GeV Au+Au collisions." In: *Phys. Rev. Lett.* 94 (2005), p. 232301. DOI: 10.1103/PhysRevLett.94.232301. arXiv: nucl-ex/0503003.

[40] A. Adare et al., PHENIX Coll. "Evolution of π^0 suppression in Au+Au collisions from $\sqrt{s_{NN}} = 39$ to 200 GeV." In: *Phys. Rev. Lett.* 109 (2012). [Erratum: Phys.Rev.Lett. 125, 049901 (2020)], p. 152301. DOI: 10.1103/PhysRevLett.109.152301. arXiv: 1204.1526 [nucl-ex].

[41] T. Csörgő, S. V. Akkelin, Yogiro Hama, B. Lukács, and Yu. M. Sinyukov. "Observables and initial conditions for selfsimilar ellipsoidal flows." In: *Phys. Rev. C* 67 (2003), p. 034904. DOI: 10.1103/PhysRevC.67.034904. arXiv: hep-ph/0108067.

[42] S. S. Adler et al., PHENIX Coll. "Identified charged particle spectra and yields in Au+Au collisions at $\sqrt{s_{NN}}$ = 200 GeV." In: *Phys. Rev. C* 69 (2004), p. 034909. DOI: 10.1103/PhysRevC.69.034909. arXiv: nucl-ex/0307022.

[43] R. Hagedorn. "Statistical thermodynamics of strong interactions at high-energies." In: *Nuovo Cim. Suppl.* 3 (1965), pp. 147–186.

[44] Larry D. McLerran and Benjamin Svetitsky. "A Monte Carlo Study of SU(2) Yang-Mills Theory at Finite Temperature." In: *Phys. Lett. B* 98 (1981). Ed. by J. Julve and M. Ramón-Medrano, p. 195. DOI: 10.1016/0370-2693(81)90986-2.

[45] Y. Aoki, Z. Fodor, S. D. Katz, and K. K. Szabó. "The QCD transition temperature: Results with physical masses in the continuum limit." In: *Phys. Lett. B* 643 (2006), pp. 46–54. DOI: 10.1016/j.physletb.2006.10.021. arXiv: hep-lat/0609068.

[46] L. Adamczyk et al., STAR Coll. "Bulk Properties of the Medium Produced in Relativistic Heavy-Ion Collisions from the Beam Energy Scan Program." In: *Phys. Rev. C* 96.4 (2017), p. 044904. DOI: 10.1103/PhysRevC.96.044904. arXiv: 1701.07065 [nucl-ex].

[47] A. Adare et al., PHENIX Coll. "Enhanced production of direct photons in Au+Au collisions at $\sqrt{s_{NN}} = 200$ GeV and implications for the initial temperature." In: *Phys. Rev. Lett.* 104 (2010), p. 132301. DOI: 10.1103/PhysRevLett.104.132301. arXiv: 0804.4168 [nucl-ex].

[48] Hannah Petersen, Rolando La Placa, and Steffen A. Bass. "A systematic study of the sensitivity of triangular flow to the initial state fluctuations in relativistic heavy-ion collisions." In: *J. Phys. G* 39 (2012), p. 055102. DOI: 10.1088/0954-3899/39/5/055102. arXiv: 1201.1881 [nucl-th].

[49] S. S. Adler et al., PHENIX Coll. "Elliptic flow of identified hadrons in Au+Au collisions at $\sqrt{s_{NN}}$ = 200 GeV." In: *Phys. Rev. Lett.* 91 (2003), p. 182301. DOI: 10.1103/PhysRevLett.91.182301. arXiv: nucl-ex/0305013.

[50] B. I. Abelev et al., STAR Coll. "Centrality dependence of charged hadron and strange hadron elliptic flow from $\sqrt{s_{NN}}$ = 200 GeV Au+Au collisions." In: *Phys. Rev. C* 77 (2008), p. 054901. DOI: 10.1103/PhysRevC.77.054901. arXiv: 0801.3466 [nucl-ex].

[51] A. Adare et al., PHENIX Coll. "Observation of direct-photon collective flow in $\sqrt{s_{NN}} = 200$ GeV Au+Au collisions." In: *Phys. Rev. Lett.* 109 (2012), p. 122302. DOI: 10.1103/PhysRevLett.109.122302. arXiv: 1105.4126 [nucl-ex].

[52] A. Adare et al., PHENIX Coll. "Heavy Quark Production in $p + p$ and Energy Loss and Flow of Heavy Quarks in Au+Au Collisions at $\sqrt{s_{NN}} = 200$ GeV." In: *Phys. Rev. C* 84 (2011), p. 044905. DOI: 10.1103/PhysRevC.84.044905. arXiv: 1005.1627 [nucl-ex].

[53] L. Adamczyk et al., STAR Coll. "Inclusive charged hadron elliptic flow in Au+Au collisions at $\sqrt{s_{NN}}$ = 7.7 - 39 GeV." In: *Phys. Rev. C* 86 (2012), p. 054908. DOI: 10.1103/PhysRevC.86.054908. arXiv: 1206.5528 [nucl-ex].

[54] L. Adamczyk et al., STAR Coll. "Elliptic flow of identified hadrons in Au+Au collisions at $\sqrt{s_{NN}} = 7.7$-62.4 GeV." In: *Phys. Rev. C* 88 (2013), p. 014902. DOI: 10.1103/PhysRevC.88.014902. arXiv: 1301.2348 [nucl-ex].

[55] A. Adare et al., PHENIX Coll. "Elliptic and hexadecapole flow of charged hadrons in Au+Au collisions at $\sqrt{s_{NN}} = 200$ GeV." In: *Phys. Rev. Lett.* 105 (2010), p. 062301. DOI: 10.1103/PhysRevLett.105.062301. arXiv: 1003.5586 [nucl-ex].

[56] A. Adare et al., PHENIX Coll. "Energy Loss and Flow of Heavy Quarks in Au+Au Collisions at $\sqrt{s_{NN}}$ = 200 GeV." In: *Phys. Rev. Lett.* 98 (2007), p. 172301. DOI: 10.1103/PhysRevLett.98.172301. arXiv: nucl-ex/0611018.

[57] Ulrich Heinz, Chun Shen, and Huichao Song. "The viscosity of quark-gluon plasma at RHIC and the LHC." In: *AIP Conf. Proc.* 1441.1 (2012). Ed. by Stephen G. Steadman and George S. F. Stephans, pp. 766–770. DOI: 10.1063/1.3700674. arXiv: 1108.5323 [nucl-th].

[58] Dénes Molnár and Sergei A. Voloshin. "Elliptic flow at large transverse momenta from quark coalescence." In: *Phys. Rev. Lett.* 91 (2003), p. 092301. DOI: 10.1103/PhysRevLett.91.092301. arXiv: nucl-th/0302014.

[59] Alexei Bazavov and Bernd A. Berg. "Deconfining Phase Transition on Lattices with Boundaries at Low Temperature." In: *Phys. Rev. D* 76 (2007), p. 014502. DOI: 10.1103/PhysRevD.76.014502. arXiv: hep-lat/0701007.

[60] Y. Aoki, G. Endrődi, Z. Fodor, S. D. Katz, and K. K. Szabó. "The order of the quantum chromodynamics transition predicted by the standard model of particle physics." In: *Nature* 443 (2006), pp. 675–678.

[61] M. Cheng et al. "The QCD equation of state with almost physical quark masses." In: *Phys. Rev. D* 77 (2008), p. 014511. DOI: 10.1103/PhysRevD.77.014511. arXiv: 0710.0354 [hep-lat].

[62] Y. Aoki, Szabolcs Borsányi, Stephan Durr, Zoltán Fodor, Sándor D. Katz, Stefan Krieg, and Kálmán K. Szabó. "The QCD transition temperature: results with physical masses in the continuum limit II." In: *JHEP* 06 (2009), p. 088. DOI: 10.1088/1126-6708/2009/06/088. arXiv: 0903.4155 [hep-lat].

[63] A. Bazavov et al. "The chiral and deconfinement aspects of the QCD transition." In: *Phys. Rev. D* 85 (2012), p. 054503. DOI: 10.1103/PhysRevD.85.054503. arXiv: 1111.1710 [hep-lat].

[64] A. Bazavov et al., HotQCD Coll. "Equation of state in (2+1)-flavor QCD." In: *Phys. Rev. D* 90 (2014), p. 094503. DOI: 10.1103/PhysRevD.90.094503. arXiv: 1407.6387 [hep-lat].

[65] Shinji Ejiri. "Canonical partition function and finite density phase transition in lattice QCD." In: *Phys. Rev. D* 78 (2008), p. 074507. DOI: 10.1103/PhysRevD.78.074507. arXiv: 0804.3227 [hep-lat].

[66] M. Asakawa and K. Yazaki. "Chiral Restoration at Finite Density and Temperature." In: *Nucl. Phys. A* 504 (1989), pp. 668–684. DOI: 10.1016/0375-9474(89)90002-X.

[67] A. Barducci, R. Casalbuoni, S. De Curtis, Raoul Gatto, and Giulio Pettini. "Chiral Symmetry Breaking in QCD at Finite Temperature and Density." In: *Phys. Lett. B* 231 (1989), pp. 463–470. DOI: 10.1016/0370-2693(89)90695-3.

[68] A. Barducci, R. Casalbuoni, S. De Curtis, Raoul Gatto, and Giulio Pettini. "Chiral Phase Transitions in QCD for Finite Temperature and Density." In: *Phys. Rev. D* 41 (1990), p. 1610. DOI: 10.1103/PhysRevD.41.1610.

[69] Mikhail A. Stephanov. "QCD phase diagram and the critical point." In: *Prog. Theor. Phys. Suppl.* 153 (2004). Ed. by Berndt Muller and C. I. Tan, pp. 139–156. DOI: 10.1142/S0217751X05027965. arXiv: hep-ph/0402115.

[70] Jaroslav Adam et al., STAR Coll. "Flow and interferometry results from Au+Au collisions at $\sqrt{s_{NN}} = 4.5$ GeV." In: *Phys. Rev. C* 103.3 (2021), p. 034908. DOI: 10.1103/PhysRevC.103.034908. arXiv: 2007.14005 [nucl-ex].

[71] Anton Andronic. "An overview of the experimental study of quark-gluon matter in high-energy nucleus-nucleus collisions." In: *Int. J. Mod. Phys. A* 29 (2014), p. 1430047. DOI: 10.1142/S0217751X14300476. arXiv: 1407.5003 [nucl-ex].

[72] Grazyna Odyniec. "Beam Energy Scan Program at RHIC (BES I and BES II) – Probing QCD Phase Diagram with Heavy-Ion Collisions." In: *PoS* CORFU2018 (2019). Ed. by Konstantinos Anagnostopoulos et al., p. 151. DOI: 10.22323/1.347.0151.

[73] Yang Wu. "Recent results for STAR $\sqrt{s_{NN}} = 4.9$ GeV Al+Au and $\sqrt{s_{NN}} = 4.5$ GeV Au+Au Fixed-Target Collisions." In: *Nucl. Phys. A* 982 (2019). Ed. by Federico Antinori, Andrea Dainese, Paolo Giubellino, Vincenzo Greco, Maria Paola Lombardo, and Enrico Scomparin, pp. 899–902. DOI: 10.1016/j.nuclphysa.2018.10.051. arXiv: 1807.06738 [nucl-ex].

[74] M. S. Abdallah et al., STAR Coll. "Measurements of Proton High Order Cumulants in $\sqrt{s_{\mathrm{NN}}} = 3$ GeV Au+Au Collisions and Implications for the QCD Critical Point." In: *Phys. Rev. Lett.* 128.20 (2022), p. 202303. DOI: 10.1103/PhysRevLett.128.202303. arXiv: 2112.00240 [nucl-ex].

[75] Marek Gazdzicki. "NA49/NA61: results and plans on beam energy and system size scan at the CERN SPS." In: *J. Phys. G* 38 (2011). Ed. by Yves Schutz and Urs Achim Wiedemann, p. 124024. DOI: 10.1088/0954-3899/38/12/124024. arXiv: 1107.2345 [nucl-ex].

[76] J. Friese. "Studying in-medium hadron properties with HADES." In: *Prog. Part. Nucl. Phys.* 42 (1999). Ed. by A. Faessler, pp. 235–245. DOI: 10.1016/S0146-6410(99)00079-4.

[77] T. Ablyazimov et al., CBM Coll. "Challenges in QCD matter physics –The scientific programme of the Compressed Baryonic Matter experiment at FAIR." In: *Eur. Phys. J. A* 53.3 (2017), p. 60. DOI: 10.1140/epja/i2017-12248-y. arXiv: 1607.01487 [nucl-ex].

[78] V. Abgaryan et al., MPD Coll. "Status and initial physics performance studies of the MPD experiment at NICA." In: (Feb. 2022). arXiv: 2202.08970 [physics.ins-det].

[79] Takao Sakaguchi. "High density matter physics at J-PARC-HI." In: *PoS* CORFU2018 (2019). Ed. by Konstantinos Anagnostopoulos et al., p. 189. DOI: 10.22323/1.347.0189. arXiv: 1904.12821 [nucl-ex].

[80] Adam Bzdak, Shinichi Esumi, Volker Koch, Jinfeng Liao, Mikhail Stephanov, and Nu Xu. "Mapping the Phases of Quantum Chromodynamics with Beam Energy Scan." In: *Phys. Rept.* 853 (2020), pp. 1–87. DOI: 10.1016/j.physrep.2020.01.005. arXiv: 1906.00936 [nucl-th].

[81] Achim Franz. "Five years of tracking heavy ion collisions at RHIC." In: *Nuclear Instruments and Methods in Physics Research Section A: Accelerators, Spectrometers, Detectors and Associated Equipment* 566.1 (2006). TIME 2005, pp. 54–61. ISSN: 0168-9002. DOI: https://doi.org/10.1016/j.nima.2006.05.050. URL: https://www.sciencedirect.com/science/article/pii/S0168900206008096.

[82] K. Adcox et al., PHENIX Coll. "PHENIX detector overview." In: *Nucl. Instrum. Meth.* A499 (2003), pp. 469–479. DOI: 10.1016/S0168-9002(02)01950-2.

[83] K. H. Ackermann et al., STAR Coll. "STAR detector overview." In: *Nucl. Instrum. Meth. A* 499 (2003), pp. 624–632. DOI: 10.1016/S0168-9002(02)01960-5.

[84] M Adamczyk et al. "The BRAHMS experiment at RHIC." In: *Nuclear Instruments and Methods in Physics Research Section A: Accelerators, Spectrometers, Detectors and Associated Equipment* 499.2 (2003). The Relativistic Heavy Ion Collider Project: RHIC and its Detectors, pp. 437–468. ISSN: 0168-9002. DOI: https://doi.org/10.1016/S0168-9002(02)01949-6. URL: https://www.sciencedirect.com/science/article/pii/S0168900202019496.

[85] B.B Back et al. "The PHOBOS detector at RHIC." In: *Nuclear Instruments and Methods in Physics Research Section A: Accelerators, Spectrometers, Detectors and Associated Equipment* 499.2 (2003). The Relativistic Heavy Ion Collider Project: RHIC and its Detectors, pp. 603–623. ISSN: 0168-9002. DOI: https://doi.org/10.1016/S0168-9002(02)01959-9. URL: https://www.sciencedirect.com/science/article/pii/S0168900202019599.

[86] I Alekseev et al. "Polarized proton collider at RHIC." In: *Nucl. Instrum. Meth. A* 499 (2003), pp. 392–414. DOI: 10.1016/S0168-9002(02)01946-0.

[87] Lokesh Kumar. "STAR Results from the RHIC Beam Energy Scan-I." In: *Nucl. Phys. A* 904-905 (2013). Ed. by Thomas Ullrich, Bolek Wyslouch, and John W. Harris, pp. 256c–263c. DOI: 10.1016/j.nuclphysa.2013.01.070. arXiv: 1211.1350 [nucl-ex].

[88] L. Adamczyk et al., STAR Coll. "Beam-Energy Dependence of the Directed Flow of Protons, Antiprotons, and Pions in Au+Au Collisions." In: *Phys. Rev. Lett.* 112.16 (2014), p. 162301. DOI: 10.1103/PhysRevLett.112.162301. arXiv: 1401.3043 [nucl-ex].

[89] L. Adamczyk et al., STAR Coll. "Energy Dependence of Moments of Net-proton Multiplicity Distributions at RHIC." In: *Phys. Rev. Lett.* 112 (2014), p. 032302. DOI: 10.1103/PhysRevLett.112.032302. arXiv: 1309.5681 [nucl-ex].

[90] L. Adamczyk et al., STAR Coll. "Energy dependence of acceptance-corrected dielectron excess mass spectrum at mid-rapidity in Au+Au collisions at $\sqrt{s_{NN}} = 19.6$ and 200 GeV." In: *Phys. Lett. B* 750 (2015), pp. 64–71. DOI: 10.1016/j.physletb.2015.08.044. arXiv: 1501.05341 [hep-ex].

[91] Yi Yang. "The STAR detector upgrades for the BES II and beyond physics program." In: *Nucl. Phys. A* 1005 (2021). Ed. by Feng Liu, Enke Wang, Xin-Nian Wang, Nu Xu, and Ben-Wei Zhang, p. 121758. DOI: 10.1016/j.nuclphysa.2020.121758.

[92] Kathryn C. Meehan. "Fixed Target Collisions at STAR." In: *Nucl. Phys. A* 956 (2016). Ed. by Y. Akiba, S. Esumi, K. Fukushima, H. Hamagaki, T. Hatsuda, T. Hirano, and K. Shigaki, pp. 878–881. DOI: 10.1016/j.nuclphysa.2016.04.016.

[93] Jaroslav Adam et al., STAR Coll. "Polarization of Λ ($\bar{\Lambda}$) hyperons along the beam direction in Au+Au collisions at $\sqrt{s_{NN}}$ = 200 GeV." In: *Phys. Rev. Lett.* 123.13 (2019), p. 132301. DOI: 10.1103/PhysRevLett.123.132301. arXiv: 1905.11917 [nucl-ex].

[94] Mohamed Abdallah et al., STAR Coll. "Search for the chiral magnetic effect with isobar collisions at $\sqrt{s_{NN}}$=200 GeV by the STAR Collaboration at the BNL Relativistic Heavy Ion Collider." In: *Phys. Rev. C* 105.1 (2022), p. 014901. DOI: 10.1103/PhysRevC.105.014901. arXiv: 2109.00131 [nucl-ex].

[95] Mohamed Abdallah et al., STAR Coll. "Longitudinal double-spin asymmetry for inclusive jet and dijet production in polarized proton collisions at $\sqrt{s}$ = 200 GeV." In: *Phys. Rev. D* 103.9 (2021), p. L091103. DOI: 10.1103/PhysRevD.103.L091103. arXiv: 2103.05571 [hep-ex].

[96] Fuwang Shen, Shuai Wang, Fangang Kong, Shiwei Bai, Changyu Li, Flemming Videbæk, Zhangbu Xu, Chengguang Zhu, Qinghua Xu, and Chi Yang. "MWPC prototyping and performance test for the STAR inner TPC upgrade." In: *Nucl. Instrum. Meth. A* 896 (2018), pp. 90–95. DOI: 10.1016/j.nima.2018.04.019. arXiv: 1805.03938 [physics.ins-det].

[97] CBM eTOF Group STAR. "Physics Program for the STAR/CBM eTOF Upgrade." In: (Sept. 2016). arXiv: 1609.05102 [nucl-ex].

[98] Joseph Adams et al. "The STAR Event Plane Detector." In: *Nucl. Instrum. Meth. A* 968 (2020), p. 163970. DOI: 10.1016/j.nima.2020.163970. arXiv: 1912.05243 [physics.ins-det].

[99] W.J. Llope et al. "The STAR Vertex Position Detector." In: *Nuclear Instruments and Methods in Physics Research Section A: Accelerators, Spectrometers, Detectors and Associated Equipment* 759 (2014), pp. 23–28. ISSN: 0168-9002. DOI: https://doi.org/10.1016/j.nima.2014.04.080. URL: https://www.sciencedirect.com/science/article/pii/S0168900214004938.

[100] C. A. Whitten. "The beam-beam counter: A local polarimeter at STAR." In: *AIP Conf. Proc.* 980.1 (2008). Ed. by Ahovi Kponou, Yousef Makdisi, and Anatoli Zelenski, pp. 390–396. DOI: 10.1063/1.2888113.

[101] Prashanth Shanmuganathan. "An Improved Event Plane Detector for the STAR Experiment." In: *PoS* CPOD2017 (2018), p. 066. DOI: 10.22323/1.311.0066.

[102] M. Anderson et al. "The Star time projection chamber: A Unique tool for studying high multiplicity events at RHIC." In: *Nucl. Instrum. Meth. A* 499 (2003), pp. 659–678. DOI: 10.1016/S0168-9002(02)01964-2. arXiv: nucl-ex/0301015.

[103] M. Shao, Olga Yu. Barannikova, X. Dong, Y. Fisyak, L. Ruan, P. Sorensen, and Z. Xu. "Extensive particle identification with TPC and TOF at the STAR experiment." In: *Nucl. Instrum. Meth. A* 558 (2006), pp. 419–429. DOI: 10.1016/j.nima.2005.11.251. arXiv: nucl-ex/0505026.

[104] J. Wu and M. Xu. "A barrel TOF for STAR at RHIC." In: *J. Phys. G* 34 (2007). Ed. by Yu-Gang Ma, Zhi-Yuan Zhu, En-Ke Wang, Xu Cai, Huan-Zhong Huang, and Xin-Nian Wang, S729–S732. DOI: 10.1088/0954-3899/34/8/S83.

[105] W. J. Llope. "Large-Area Fast-Timing Systems In STAR." In: *AIP Conf. Proc.* 1336 (2011). Ed. by Floyd D. McDaniel and Barney L. Doyle, p. 569. DOI: 10.1063/1.3586165.

[106] M. Beddo et al., STAR Coll. "The STAR barrel electromagnetic calorimeter." In: *Nucl. Instrum. Meth. A* 499 (2003), pp. 725–739. DOI: 10.1016/S0168-9002(02)01970-8.

[107] R. Lednicky. "Femtoscopy with unlike particles." In: *International Workshop on the Physics of the Quark Gluon Plasma*. Dec. 2001. arXiv: nucl-th/0112011.

[108] R. Hanbury Brown and R. Q. Twiss. "A New type of interferometer for use in radio astronomy." In: *Phil. Mag.* 45 (1954), pp. 663–682.

[109] R. Hanbury Brown and R. Q. Twiss. "A Test of a new type of stellar interferometer on Sirius." In: *Nature* 178 (1956), pp. 1046–1048. DOI: 10.1038/1781046a0.

[110] R. Hanbury Brown and R. Q. Twiss. "Correlation between Photons in two Coherent Beams of Light." In: *Nature* 177 (1956), pp. 27–29. DOI: 10.1038/177027a0.

[111] R. Q. Twiss, A. G. Little, and R. Hanbury Brown. "Correlation Between Photons, in Coherent Beams of Light, Detected by a Coincidence Counting Technique." In: *Nature* 180.4581 (1957), pp. 324–326. ISSN: 1476-4687. DOI: 10.1038/180324a0. URL: https://doi.org/10.1038/180324a0.

[112] Roy J. Glauber. "Photon correlations." In: *Phys. Rev. Lett.* 10 (1963), pp. 84–86. DOI: 10.1103/PhysRevLett.10.84.

[113] Roy J. Glauber. "Nobel Lecture: One hundred years of light quanta." In: *Rev. Mod. Phys.* 78 (2006), pp. 1267–1278. DOI: 10.1103/RevModPhys.78.1267.

[114] Roy J. Glauber. "Quantum Optics and Heavy Ion Physics." In: *Nucl. Phys.* A774 (2006), pp. 3–13. DOI: 10.1016/j.nuclphysa.2006.06.009. arXiv: nucl-th/0604021 [nucl-th].

[115] R. Hanbury Brown. "The stellar interferometer at Narrabri, Australia." In: *Philips Technical Review* 27 (1966), p. 141.

[116] R. Hanbury Brown, J. Davis, and L. R. Allen. "The Angular Diameters of 32 Stars." In: *Monthly Notices of the Royal Astronomical Society* 167.1 (Apr. 1974), pp. 121–136. ISSN: 0035-8711. DOI: 10.1093/mnras/167.1.121. eprint: https://academic.oup.com/mnras/article-pdf/167/1/121/8079851/mnras167-0121.pdf. URL: https://doi.org/10.1093/mnras/167.1.121.

[117] A. D. Code, J. Davis, R. C. Bless, and R. H. Brown. "Empirical effective temperatures and bolometric corrections for early-type stars." In: *The Astrophysical Journal* 203 (Jan. 1976), pp. 417–434. DOI: 10.1086/154093.

[118] Gordon Baym. "The Physics of Hanbury Brown-Twiss intensity interferometry: From stars to nuclear collisions." In: *Acta Phys. Polon. B* 29 (1998). Ed. by A. Bialas, pp. 1839–1884. arXiv: nucl-th/9804026.

[119] Gerson Goldhaber, William B. Fowler, Sulamith Goldhaber, and T. F. Hoang. "Pion-pion correlations in antiproton annihilation events." In: *Phys. Rev. Lett.* 3 (1959), pp. 181–183. DOI: 10.1103/PhysRevLett.3.181.

[120] Gerson Goldhaber, Sulamith Goldhaber, Won-Yong Lee, and Abraham Pais. "Influence of Bose-Einstein statistics on the antiproton proton annihilation process." In: *Phys. Rev.* 120 (1960). Ed. by R. M. Weiner, pp. 300–312. DOI: 10.1103/PhysRev.120.300.

[121] S. S. Adler et al., PHENIX Coll. "Bose-Einstein correlations of charged pion pairs in Au + Au collisions at $\sqrt{s_{NN}}$ = 200 GeV." In: *Phys. Rev. Lett.* 93 (2004), p. 152302. DOI: 10.1103/PhysRevLett.93.152302. arXiv: nucl-ex/0401003.

[122] S. Afanasiev et al., PHENIX Coll. "Kaon interferometric probes of space-time evolution in Au+Au collisions at $\sqrt{s_{NN}}$ = 200 GeV." In: *Phys. Rev. Lett.* 103 (2009), p. 142301. DOI: 10.1103/PhysRevLett.103.142301. arXiv: 0903.4863 [nucl-ex].

[123] A. N. Makhlin and Yu. M. Sinyukov. "Hydrodynamics of Hadron Matter Under Pion Interferometric Microscope." In: *Z. Phys.* C39 (1988), p. 69. DOI: 10.1007/BF01560393.

[124] T. Csörgő and B. Lorstad. "Bose-Einstein correlations for three-dimensionally expanding, cylindrically symmetric, finite systems." In: *Phys. Rev. C* 54 (1996), pp. 1390–1403. DOI: 10.1103/PhysRevC.54.1390. arXiv: hep-ph/9509213.

[125] D. H. Boal, C. K. Gelbke, and B. K. Jennings. "Intensity interferometry in subatomic physics." In: *Rev. Mod. Phys.* 62 (1990), pp. 553–602. DOI: 10.1103/RevModPhys.62.553.

[126] R. M. Weiner. "Boson interferometry in high-energy physics." In: *Phys. Rept.* 327 (2000), pp. 249–346. DOI: 10.1016/S0370-1573(99)00114-3. arXiv: hep-ph/9904389 [hep-ph].

[127] Urs Achim Wiedemann and Ulrich W. Heinz. "Particle interferometry for relativistic heavy ion collisions." In: *Phys. Rept.* 319 (1999), pp. 145–230. DOI: 10.1016/S0370-1573(99)00032-0. arXiv: nucl-th/9901094 [nucl-th].

[128] Csörgő, T. "Particle interferometry from 40-MeV to 40-TeV." In: *Heavy Ion Phys.* 15 (2002), pp. 1–80. DOI: 10.1556/APH.15.2002.1-2.1. arXiv: hep-ph/0001233 [hep-ph].

[129] Adam Kisiel. "Overview of the femtoscopy studies in Pb Pb and p p collisions at the LHC by the ALICE experiment." In: *PoS* WPCF2011 (2011), p. 003.

[130] Michael Annan Lisa, Scott Pratt, Ron Soltz, and Urs Wiedemann. "Femtoscopy in relativistic heavy ion collisions." In: *Ann. Rev. Nucl. Part. Sci.* 55 (2005), pp. 357–402. DOI: 10.1146/annurev.nucl.55.090704.151533. arXiv: nucl-ex/0505014.

[131] J. Bolz et al. "Resonance decays and partial coherence in Bose-Einstein correlations." In: *Phys. Rev.* D47 (1993), pp. 3860–3870. DOI: 10.1103/PhysRevD.47.3860.

[132] Csörgő, T. and Lörstad, B. and Zimányi, J. "Bose-Einstein correlations for systems with large halo." In: *Z. Phys.* C71 (1996), pp. 491–497. DOI: 10.1007/BF02907008, 10.1007/s002880050195. arXiv: hep-ph/9411307 [hep-ph].

[133] M. G. Bowler. "Coulomb corrections to Bose-Einstein correlations have been greatly exaggerated." In: *Phys. Lett. B* 270 (1991), pp. 69–74. DOI: 10.1016/0370-2693(91)91541-3.

[134] Yu. Sinyukov et al. "Coulomb corrections for interferometry analysis of expanding hadron systems." In: *Phys. Lett.* B432 (1998), pp. 248–257. DOI: 10.1016/S0370-2693(98)00653-4.

[135] J. I. Kapusta, D. Kharzeev, and L. D. McLerran. "The Return of the prodigal Goldstone boson." In: *Phys. Rev.* D53 (1996), pp. 5028–5033.

[136] S. E. Vance, T. Csörgő, and D. Kharzeev. "Partial U(A)(1) restoration from Bose-Einstein correlations." In: *Phys. Rev. Lett.* 81 (1998), pp. 2205–2208.

[137] Csörgő, T. and Vértesi, R. and Sziklai, J. "Indirect observation of an in-medium η ' mass reduction in $\sqrt{s_{NN}} = 200$ GeV Au+Au collisions." In: *Phys. Rev. Lett.* 105 (2010), p. 182301. DOI: 10.1103/PhysRevLett.105.182301.

[138] R. Vértesi, T. Csörgő, and J. Sziklai. "Significant in-medium η ' mass reduction in $\sqrt{s_{NN}} = 200$ GeV Au+Au collisions at the BNL Relativistic Heavy Ion Collider." In: *Phys. Rev. C* 83 (2011), p. 054903. DOI: 10.1103/PhysRevC.83.054903. arXiv: 0912.0258 [nucl-ex].

[139] T. Csörgő, B. Lorstad, and J. Zimanyi. "Quantum statistical correlations for slowly expanding systems." In: *Phys. Lett. B* 338 (1994), pp. 134–140. DOI: 10.1016/0370-2693(94)91356-0. arXiv: nucl-th/9408022.

[140] S. V. Akkelin and Yu. M. Sinyukov. "The HBT interferometry of expanding sources." In: *Phys. Lett. B* 356 (1995), pp. 525–530. DOI: 10.1016/0370-2693(95)00765-D.

[141] David A. Brown and Pawel Danielewicz. "Imaging of sources in heavy ion reactions." In: *Phys. Lett. B* 398 (1997), pp. 252–258. DOI: 10.1016/S0370-2693(97)00251-7. arXiv: nucl-th/9701010.

[142] S. S. Adler et al., PHENIX Coll. "Evidence for a long-range component in the pion emission source in Au + Au collisions at $\sqrt{s_{NN}}$ = 200 GeV." In: *Phys. Rev. Lett.* 98 (2007), p. 132301. DOI: 10.1103/PhysRevLett.98.132301. arXiv: nucl-ex/0605032.

[143] M. Csanád, T. Csörgő, and M. Nagy. "Anomalous diffusion of pions at RHIC." In: *Braz. J. Phys.* 37 (2007). Ed. by Sandra S. Padula and Scott Pratt, pp. 1002–1013. DOI: 10.1590/S0103-97332007000600018. arXiv: hep-ph/0702032.

[144] Barnabás Pórfy. "Lévy HBT Results at NA61/SHINE." In: *Universe* 5.6 (2019), p. 154. DOI: 10.3390/universe5060154. arXiv: 1906.06065 [nucl-ex].

[145] CMS Collaboration. *Measurement of two-particle Bose-Einstein momentum correlations and their Levy parameters at* $\sqrt{s_{\mathrm{NN}}} = 5.02$ *TeV PbPb collisions*. Tech. rep. Geneva: CERN, 2022. URL: https://cds.cern.ch/record/2806150.

[146] T. Csörgő, S. Hegyi, T. Novak, and W. A. Zajc. "Bose-Einstein or HBT correlations and the anomalous dimension of QCD." In: *Acta Phys. Polon. B* 36 (2005). Ed. by B. Gary, pp. 329–337. arXiv: hep-ph/0412243.

[147] T. Csörgő, S. Hegyi, T. Novák, and W. A. Zajc. "Bose-Einstein or HBT correlation signature of a second order QCD phase transition." In: *AIP Conf. Proc.* 828.1 (2006). Ed. by Vladislav Simak, Michal Sumbera, Sarka Todorova-Nova, and Boris Tomasik, pp. 525–532. DOI: 10.1063/1.2197465. arXiv: nucl-th/0512060.

[148] Jakub Cimermaň, Christopher Plumberg, and Boris Tomášik. "The Shape of the Correlation Function." In: *Phys. Part. Nucl.* 51.3 (2020), pp. 282–287. arXiv: 1909.07998 [nucl-th].

[149] Jakub Cimerman, Chrisopher Plumberg, and Boris Tomášik. "The Shape of the Correlation Function." In: *PoS* ICHEP2020 (2021), p. 538. DOI: 10.22323/1.390.0538. arXiv: 2012.04412 [nucl-th].

[150] V. V. Uchaikin and G. G. Gusarov. In: *Journal of Mathematical Sciences* 93 no. 4 (1999), p. 591.

[151] Roy A. Lacey. "Indications for a critical point in the phase diagram for hot and dense nuclear matter." In: *Nucl. Phys.* A956 (2016), pp. 348–351. DOI: 10.1016/j.nuclphysa.2016.01.032. arXiv: 1512.09152 [nucl-ex].

[152] Roy A. Lacey, Peifeng Liu, Niseem Magdy, B. Schweid, and N. N. Ajitanand. "Finite-Size Scaling of Non-Gaussian Fluctuations Near the QCD Critical Point." In: (2016). arXiv: 1606.08071 [nucl-ex].

[153] A. M. Halasz et al. "On the phase diagram of QCD." In: *Phys. Rev.* D58 (1998), p. 096007. DOI: 10.1103/PhysRevD.58.096007. arXiv: hep-ph/9804290 [hep-ph].

[154] Misha A. Stephanov, K. Rajagopal, and Edward V. Shuryak. "Signatures of the tricritical point in QCD." In: *Phys. Rev. Lett.* 81 (1998), pp. 4816–4819. DOI: 10.1103/PhysRevLett.81.4816.

[155] Sheer El-Showk, Miguel F. Paulos, David Poland, Slava Rychkov, David Simmons-Duffin, and Alessandro Vichi. "Solving the 3d Ising Model with the Conformal Bootstrap II. c-Minimization and Precise Critical Exponents." In: *J. Stat. Phys.* 157 (2014), p. 869. DOI: 10.1007/s10955-014-1042-7. arXiv: 1403.4545 [hep-th].

[156] Heiko Rieger. "Critical behavior of the three-dimensional random-field Ising model: Two-exponent scaling and discontinuous transition." In: *Phys. Rev. B* 52 (9 1995), pp. 6659–6667. DOI: 10.1103/PhysRevB.52.6659. URL: http://link.aps.org/doi/10.1103/PhysRevB.52.6659.

[157] G. Bertsch, M. Gong, and M. Tohyama. "Pion Interferometry in Ultrarelativistic Heavy Ion Collisions." In: *Phys. Rev.* C37 (1988), pp. 1896–1900. DOI: 10.1103/PhysRevC.37.1896.

[158] S. Pratt. "Coherence and Coulomb Effects on Pion Interferometry." In: *Phys. Rev.* D33 (1986), pp. 72–79. DOI: 10.1103/PhysRevD.33.72.

[159] J. Adams et al., STAR Coll. "Pion interferometry in Au+Au collisions at $\sqrt{s_{NN}}$ = 200 GeV." In: *Phys. Rev. C* 71 (2005), p. 044906. DOI: 10.1103/PhysRevC.71.044906. arXiv: nucl-ex/0411036.

[160] S. Afanasiev et al., PHENIX Coll. "Source breakup dynamics in Au+Au Collisions at $\sqrt{s_{NN}}$ = 200 GeV via three-dimensional two-pion source imaging." In: *Phys. Rev. Lett.* 100 (2008), p. 232301. DOI: 10.1103/PhysRevLett.100.232301. arXiv: 0712.4372 [nucl-ex].

[161] Tamás Novák. "Bose-Einstein correlations in e^+e^- annihilation." 2008. URL: http://cds.cern.ch/record/1169637.

[162] Máté Csanád. *2D Bose-Einstein correlation function in LCMS*. 2019. URL: https://drupal.star.bnl.gov/STAR/blog/mcsanad/2d-bose-einstein-correlation-function-lcms (visited on 07/19/2022).

[163] P. Achard et al., L3 Coll. "Test of the τ-Model of Bose-Einstein Correlations and Reconstruction of the Source Function in Hadronic Z-boson Decay at LEP." In: *Eur. Phys. J. C* 71 (2011), p. 1648. DOI: 10.1140/epjc/s10052-011-1648-8. arXiv: 1105.4788 [hep-ex].

[164] T. Csörgő and J. Zimányi. "Pion interferometry for strongly correlated space-time and momentum space." In: *Nucl. Phys. A* 517 (1990), pp. 588–598. DOI: 10.1016/0375-9474(90)90220-G.

[165] Bálint Kurgyis. "Coulomb interaction for Lévy sources." In: July 2020. arXiv: 2007.10173 [nucl-th].

[166] Richard P Feynman and Matthew Sands. *The Feynman Lectures on Physics, boxed set*. London, England: Basic Books, Jan. 2011.

[167] F. James and M. Roos. "Minuit - a system for function minimization and analysis of the parameter errors and correlations." In: *Computer Physics Communications* 10.6 (1975), pp. 343–367. ISSN: 0010-4655. DOI: http://dx.doi.org/10.1016/0010-4655(75)90039-9. URL: http://www.sciencedirect.com/science/article/pii/0010465575900399.

[168] Tamás Csörgő. "Correlation Probes of a QCD Critical Point." In: *PoS* HIGH-PTLHC08 (2008), p. 027. arXiv: 0903.0669 [nucl-th].

[169] Bálint Kurgyis. "Three particle Lévy HBT from PHENIX." In: *Phys. Part. Nucl.* 51.3 (2020), pp. 263–266. DOI: 10.1134/S1063779620030181. arXiv: 1910.05019 [nucl-ex].

[170] Bálint Kurgyis. "Three dimensional Lévy HBT results from PHENIX." In: *13th Workshop on Particle Correlations and Femtoscopy*. Sept. 2018. DOI: 10.5506/APhysPolBSupp.12.477. arXiv: 1809.09392 [nucl-ex].

[171] Sándor Lökös. "Centrality dependent Lévy-stable two-pion Bose-Einstein correlations in $\sqrt{s_{NN}} = 200$GeV Au+Au collisions at the PHENIX experiment." In: *Universe* 4.2 (2018). Ed. by Máté Csanád, Tamás Csörgő, and Tamás Novák, p. 31. DOI: 10.3390/universe4020031. arXiv: 1801.08827 [nucl-ex].

[172] H. Bichsel. "A method to improve tracking and particle identification in TPCs and silicon detectors." In: *Nucl. Instrum. Meth. A* 562 (2006), pp. 154–197. DOI: 10.1016/j.nima.2006.03.009.

[173] J. Adams et al., STAR Coll. "Pion interferometry in Au+Au collisions at $\sqrt{s_{NN}} = 200$ GeV." In: *Phys. Rev. C* 71 (2005), p. 044906. DOI: 10.1103/PhysRevC.71.044906. arXiv: nucl-ex/0411036.

[174] Akitomo Enokizono. "Space-time evolution of hot and dense matter probed by Bose-Einstein correlation in $Au + Au$ collisions at $\sqrt{s_{NN}} = 200$ GeV." PhD thesis. Hiroshima U., 2004. URL: https://inspirehep.net/literature/673843.

[175] L. Adamczyk et al., STAR Coll. "Beam-energy-dependent two-pion interferometry and the freeze-out eccentricity of pions measured in heavy ion collisions at the STAR detector." In: *Phys. Rev. C* 92.1 (2015), p. 014904. DOI: 10.1103/PhysRevC.92.014904. arXiv: 1403.4972 [nucl-ex].

[176] Barnabás Pórfy. "Quantum statistical correlations in high energy physics." MA thesis. Eötvös U., 2022. URL: http://csanad.web.elte.hu/phys/diakok/porfybarnabas_msc.pdf.

[177] Robert Hanbury Brown. *Boffin: A personal story of the early days of radar, radio astronomy and quantum optics*. 1991.

[178] Richard Lednicky. "Finite-size effects on two-particle production in continuous and discrete spectrum." In: *Phys. Part. Nucl.* 40 (2009), pp. 307–352. DOI: 10.1134/S1063779609030034. arXiv: nucl-th/0501065.

[179] E. O. Alt, T. Csörgő, B. Lorstad, and J. Schmidt-Sorensen. "Coulomb corrections to the three-body correlation function in high-energy heavy ion reactions." In: *Phys. Lett. B* 458 (1999), pp. 407–414. DOI: 10.1016/S0370-2693(99)00588-2. arXiv: hep-ph/9812474.

[180] Pratt, S. and Csörgő, T. and Zimányi, J. "Detailed predictions for two pion correlations in ultrarelativistic heavy ion collisions." In: *Phys. Rev.* C42 (1990), pp. 2646–2652. DOI: 10.1103/PhysRevC.42.2646.

[181] H. A. Bethe, L. Maximon, and F. Low. "Bremsstrahlung at High Energies." In: *Phys. Rev.* 91 (2 1953), pp. 417–418. DOI: 10.1103/PhysRev.91.417.2. URL: https://link.aps.org/doi/10.1103/PhysRev.91.417.2.

[182] L. D. Landau and E. M. Lifshitz. *Quantum Mechanics: Non-Relativistic Theory, 3-rd Ed., Sect. 136*. Oxford: Pergamon Press, 1977.

[183] J. Bijnens, G. Colangelo, G. Ecker, J. Gasser, and M. E. Sainio. "Pion-pion scattering at low energy." In: *Nucl. Phys. B* 508 (1997). [Erratum: Nucl.Phys.B 517, 639–639 (1998)], pp. 263–310. DOI: 10.1016/S0550-3213(97)00621-4. arXiv: hep-ph/9707291.

[184] S. K. Adhikari. "Improved effective-range expansions for small and large values of scattering length." In: *Eur. J. Phys.* 39.5 (2018), p. 055403. DOI: 10.1088/1361-6404/aad620. arXiv: 1807.05208 [quant-ph].

[185] A. Schenk. "Absorption and dispersion of pions at finite temperature." In: *Nucl. Phys. B* 363 (1991), pp. 97–113. DOI: 10.1016/0550-3213(91)90236-Q.

[186] G. Colangelo, J. Gasser, and H. Leutwyler. "$\pi\pi$ scattering." In: *Nucl. Phys. B* 603 (2001), pp. 125–179. DOI: 10.1016/S0550-3213(01)00147-X. arXiv: hep-ph/0103088.

[187] R. Garcia-Martin, R. Kaminski, J. R. Pelaez, J. Ruiz de Elvira, and F. J. Yndurain. "The Pion-pion scattering amplitude. IV: Improved analysis with once subtracted Roy-like equations up to 1100 MeV." In: *Phys. Rev. D* 83 (2011), p. 074004. DOI: 10.1103/PhysRevD.83.074004. arXiv: 1102.2183 [hep-ph].

[188] https://github.com/csanadm/StrongCoulombLevyBEC.

[189] M. Sumbera. "Selected results on Strong and Coulomb-induced correlations from the STAR experiment." In: *Braz. J. Phys.* 37 (2007). Ed. by Sandra S. Padula and Scott Pratt, pp. 925–932. DOI: 10.1590/S0103-97332007000600009. arXiv: nucl-ex/0702015.

[190] S. V. Akkelin and Yu. M. Sinyukov. "The HBT-interferometry of expanding inhomogeneous sources." In: *Z. Phys. C* 72 (1996), pp. 501–507. DOI: 10.1007/s002880050271.

[191] P. Csizmadia, T. Csörgő, and B. Lukacs. "New analytic solutions of the nonrelativistic hydrodynamical equations." In: *Phys. Lett. B* 443 (1998), pp. 21–25. DOI: 10.1016/S0370-2693(98)01297-0. arXiv: nucl-th/9805006.

[192] Máté Csanád and Márton Vargyas. "Observables from a solution of 1+3 dimensional relativistic hydrodynamics." In: *Eur. Phys. J. A* 44 (2010), pp. 473–478. DOI: 10.1140/epja/i2010-10973-3. arXiv: 0909.4842 [nucl-th].

[193] T. Csörgő, S. Hegyi, and W. A. Zajc. "Bose-Einstein correlations for Levy stable source distributions." In: *Eur. Phys. J. C* 36 (2004), pp. 67–78. DOI: 10.1140/epjc/s2004-01870-9. arXiv: nucl-th/0310042.

[194] K. Werner, Iu. Karpenko, T. Pierog, M. Bleicher, and K. Mikhailov. "Event-by-Event Simulation of the Three-Dimensional Hydrodynamic Evolution from Flux Tube Initial Conditions in Ultrarelativistic Heavy Ion Collisions." In: *Phys. Rev. C* 82 (2010), p. 044904. DOI: 10.1103/PhysRevC.82.044904. arXiv: 1004.0805 [nucl-th].

[195] H. J. Drescher, M. Hladik, S. Ostapchenko, T. Pierog, and K. Werner. "Parton based Gribov-Regge theory." In: *Phys. Rept.* 350 (2001), pp. 93–289. DOI: 10.1016/S0370-1573(00)00122-8. arXiv: hep-ph/0007198.

[196] Maria Stefaniak. "Beam Energy Scan dependence of elliptic and triangular flow of identified hadrons in the STAR experiment and the EPOS model." PhD thesis. Warsaw U. of Tech., IMT Atlantique, 2021.

[197] Bo Andersson. "THE LUND STRING MODEL." In: *7th European Symposium on Antiproton Interactions: From LEAR to the Collider and Beyond*. 1986.

[198] Silvia Ferreres-Solé and Torbjörn Sjöstrand. "The space–time structure of hadronization in the Lund model." In: *Eur. Phys. J. C* 78.11 (2018), p. 983. DOI: 10.1140/epjc/s10052-018-6459-8. arXiv: 1808.04619 [hep-ph].

[199] K. Werner, B. Guiot, Iu. Karpenko, and T. Pierog. "Analysing radial flow features in p-Pb and p-p collisions at several TeV by studying identified particle production in EPOS3." In: *Phys. Rev. C* 89.6 (2014), p. 064903. DOI: 10.1103/PhysRevC.89.064903. arXiv: 1312.1233 [nucl-th].

[200] Klaus Werner. "Core-corona separation in ultra-relativistic heavy ion collisions." In: *Phys. Rev. Lett.* 98 (2007), p. 152301. DOI: 10.1103/PhysRevLett.98.152301. arXiv: 0704.1270 [nucl-th].

[201] Szabolcs Borsányi, Gergely Endrődi, Zoltán Fodor, Antal Jakovác, Sándor D. Katz, Stefan Krieg, Claudia Ratti, and Kálmán K. Szabó. "The QCD equation of state with dynamical quarks." In: *JHEP* 11 (2010), p. 077. DOI: 10.1007/JHEP11(2010)077. arXiv: 1007.2580 [hep-lat].

[202] Fred Cooper and Graham Frye. "Comment on the Single Particle Distribution in the Hydrodynamic and Statistical Thermodynamic Models of Multiparticle Production." In: *Phys. Rev. D* 10 (1974), p. 186. DOI: 10.1103/PhysRevD.10.186.

[203] M. Bleicher et al. "Relativistic hadron hadron collisions in the ultrarelativistic quantum molecular dynamics model." In: *J. Phys. G* 25 (1999), pp. 1859–1896. DOI: 10.1088/0954-3899/25/9/308. arXiv: hep-ph/9909407.

[204] S. A. Bass et al. "Microscopic models for ultrarelativistic heavy ion collisions." In: *Prog. Part. Nucl. Phys.* 41 (1998), pp. 255–369. DOI: 10.1016/S0146-6410(98)00058-1. arXiv: nucl-th/9803035.

[205] M. Stefaniak. "Examination of Heavy-ion Collisions Using EPOS Model in the Frame of BES Program." In: *Acta Phys. Polon. Supp.* 11 (2018), p. 695. DOI: 10.5506/APhysPolBSupp.11.695.

[206] Cornelius Lanczos. "A precision approximation of the gamma function." In: *SIAM J. Numer. Anal.* 1 (1964), pp. 86–96.

EXPERIMENTAL AND PHENOMENOLOGICAL INVESTIGATIONS OF FEMTOSCOPIC CORRELATION FUNCTIONS IN HEAVY-ION COLLISIONS

SUMMARY OF A DISSERTATION SUBMITTED FOR THE DEGREE OF DOCTOR OF PHILOSOPHY BY DÁNIEL KINCSES

During my research, I investigated femtoscopic correlations, which aim to unravel the space-time structure of the particle-emitting source (the quark-gluon-plasma) created in high-energy heavy-ion collisions.

I started my experimental work by measuring Bose-Einstein correlations of pion pairs on a set of Au+Au collision data recorded by the PHENIX experiment at the Relativistic Heavy Ion Collider (RHIC). My results showed that the two-particle source function of pions exhibits a power-law behavior, and the Lévy distribution can provide an adequate description of the source shape in all investigated centrality and center-of-mass collision energy classes from $\sqrt{s_{NN}}$ = 15 GeV up to 200 GeV. The limited amount of data available at lower energies raised the need for more precise measurements. To satisfy these needs, I joined the STAR experiment at RHIC, which provides a more significant amount of data due to its larger acceptance. My preliminary results for $\sqrt{s_{NN}}$ = 200 GeV Au+Au collisions at the STAR experiment indicated that to be able to describe experimental data with such high precision, one may need to go beyond the previously utilized theoretical framework. Hence my focus shifted to phenomenological investigations.

To calculate the shape of Bose-Einstein correlation functions, one needs a proper description of the final-state interactions. Previous methods for pions only included the Coulomb interaction and assumed a negligible contribution from the strong interaction. My calculations involving both final-state interactions showed that although the inclusion of the strong interaction may only result in a few-percent difference in the source parameters, the quality of the fits to the experimentally measured correlation functions may improve significantly.

I investigated furthermore the shape of the two-particle source function in $\sqrt{s_{NN}}$ = 200 GeV Au+Au collisions simulated by the EPOS model. My event-by-event analysis showed that Lévy source shapes arise in individual events when hadronic rescattering is turned on, and resonance decays also significantly contribute to the power-law behavior. Thus the reason for the appearance of such source shapes is not event-averaging. I also investigated the average-transverse mass dependence of the Lévy source parameters and found them comparable to experimental results, although for EPOS somewhat higher values of the Lévy exponent were observed. These results also indicate that the hydro-dynamical picture usually leading to Gaussian-like distributions might need some refinements as well.

FEMTOSZKÓPIAI KORRELÁCIÓK KÍSÉRLETI ÉS FENOMENOLÓGIAI VIZSGÁLATA NEHÉZION-ÜTKÖZÉSEKBEN

KINCSES DÁNIEL

DOKTORI ÉRTEKEZÉSÉNEK MAGYAR NYELVŰ ÖSSZEFOGLALÓJA

Kutatásaim során femtoszkópiai korrelációk vizsgálatával foglalkoztam, amelyek a nagyenergiás nehézion-ütközésekben keletkező részecskekeltő forrás, a kvark-gluon-plazma téridőbeli strukturájának feltárásában játszanak fontos szerepet.

Kísérleti munkám során elsőként pion párok Bose-Einstein korrelációinak mérését végeztem el a Relativisztikus Nehézion Ütköztetőnél (RHIC-nél) található PHENIX kísérlet által rögzített arany-arany ütközések adatait felhasználva. Eredményeim alapján a kétrészecske forrásfüggvény hatványfüggvény jellegű lecsengést mutat, és a Lévy-eloszlás a forrásalak megfelelő leírását biztosítja az összes vizsgált centralitás és tömegközépponti ütközési energia tartományon $\sqrt{s_{NN}}$=15 GeV-től 200 GeV-ig. Bár az előzetes eredmények alapján a hatványfüggvény jelleget leíró Lévy-exponens mért értéke nem mutatja kritikus viselkedés jeleit, az alacsony ütközési energiákon rendelkezésre álló kevés adatmennyiség miatt felmerült az igény pontosabb mérések elvégzésére. Ennek érdekében bekapcsolódtam a RHIC-nél található STAR kísérletbe is, amely nagyobb akceptanciája révén nagyobb adatmennyiséget biztosít. A 200 GeV-es arany-arany ütközések adatain itt elvégzett mérésem eredményei azt mutatják, hogy a kísérleti adatok ilyen nagy precizitású leírásához szükség lehet az elméleti leírás finomítására, ezért fenomenológiai kutatásokat is végeztem.

A kísérletekben mért Bose-Einsten korrelációs függvények leírásához szükség van a pionok végállapoti kölcsönhatásainak megfelelő kezelésére. A korábban alkalmazott módszerek csak a Coulomb-kölcsönhatást vették figyelembe, ezért számításokat végeztem az erős kölcsönhatás vizsgálatára. Eredményeim azt mutatják, hogy bár az erős kölcsönhatás figyelembe vétele a forrásparaméterekben legfeljebb néhány százalékos eltérést okozhat, kellően precíz kísérleti adatok esetén az illesztések konfidencia szintjében jelentős javulást jelenthet.

Megvizsgáltam továbbá pionpárok forrásfüggvényének alakját az EPOS szimulációs csomag által generált arany-arany ütközések esetén. Eredményeim azt mutatják, hogy az újraszórás és a rezonanciabomlások hatására különálló események esetén is megjelenik a Lévy-forrásalak, ennek oka nem az eseményátlagolásban keresendő. A vizsgált Lévy forrásparaméterek átlagos transzverz tömeg függése összevethető a kísérleti eredményekkel, bár a Lévy-exponens esetében a kísérleti mérésekhez képest valamelyest nagyobb értékek adódtak. Mindez arra is utal, hogy az általában Gauss-jellegű eloszlásokat létrehozó hidrodinamikai kép is finomításra szorulhat.